IMPROVING THE ENERGY AND TIME RESOLUTION OF THE DRAGON ARRAY

by

William W. Huang

B.Sc. Physics, University of British Columbia, 2016

A THESIS SUBMITTED IN PARTIAL FULFILLMENT OF
THE REQUIREMENTS FOR THE DEGREE OF
MASTER OF SCIENCE
IN
PHYSICS

UNIVERSITY OF NORTHERN BRITISH COLUMBIA

December 2022

Abstract

DRAGON seeks to replace its BGO detectors with $LaBr_3$:Ce detectors. The Geant4 simulation estimates gamma ray capture efficiency values of 3.384±0.011% and 1.113±0.007% for the BGO detector and the $LaBr_3$:Ce detector respectively for 0.6617 MeV gamma rays at 5 cm distance. The latter achieves an experimental efficiency of 1.102±0.042% and an experimental energy resolution of 3.282±0.021% for these gamma rays. The experimental and simulated $LaBr_3$:Ce detector efficiency results agree within error. However, the simulation may overestimate the detector efficiency at high gamma ray energies, as observed at 4.44 MeV and 6.131 MeV. Furthermore, the timing method is performed to utilize its high time resolution. The average resonance energy is 0.47428±0.00359 MeV/u which agrees with the true value of 0.475 MeV/u. Therefore, the energy and time resolution of the $LaBr_3$:Ce detector improve DRAGON's ability to study radiative capture reactions, with its lower efficiency being its only drawback.

Contents

List of Tables

List of Figures

Glossary

Compound Nucleus - A compound nucleus may be formed during a nuclear reaction when a projectile nucleus fuses with a target nucleus [1].

Cross-Section - When a beam of projectile nuclei is incident on target nuclei, there is a probability of an interaction between the projectiles and the target. The cross-section is defined as the ratio of the number of interactions to the product of the number of incident beam projectiles on the target per unit area and the number of target nuclei that the projectile beam comes into contact with. It thereby measures the probability of the occurrence of a nuclear reaction with the units of area. The cross-section may be formulated differently to measure the probability of an interaction such as the photoelectric effect, Compton scattering, and pair production [1].

Isotropic - An isotropic radioactive source emits particles in all directions equally. This means that a detector that is placed at any angle with respect to the source will receive the same amount of particles for the same source-to-detector distance.

Lorentzian Distribution - A Lorentzian distribution is also known as a Cauchy distribution. It represents the symmetric distribution about the mean value where the peak is narrow. This distribution is used to represent the numbers of nuclear reaction events at the resonance energies, since the event frequencies form sharp peaks at these energies.

Particle - In nuclear physics, alpha particles, gamma rays, neutrons, photons, and protons are referred to as particles. However, nuclei in general can also be referred to as particles.

Resonance Energy - The discrete energy levels of the compound nucleus correspond to resonance energies in which each individual excited state corresponds to a single resonance energy where the nuclear reactions are likely to occur [1].

Resonance Reaction - In a resonance reaction, the sum of the energy that is released or absorbed in forming the compound nucleus and the projectile energy must match a resonance energy in order for the compound nucleus to reach a resonant excited state. In order for this event to occur, the projectile nuclei have an incident energy that enables them to penetrate the target nuclei. As a result, the reaction cross-section reaches a peak. The compound nucleus relaxes by emitting a particle or by emitting the projectile nucleus, and this event represents the end of the compound nucleus lifetime [1].

Acknowledgements

I graciously thank the DRAGON group for facilitating the creation of this thesis in which I specifically thank the primary supervisor Dr. Ahmed Hussein for his incredible support, patience, and guidance throughout the turbulent process of completing this thesis. Without his help, I would have struggled to understand the required concepts in nuclear astrophysics.

I also thank Dario Gigliotti, who helped me set up the electronics for the detector efficiency calibration experiments, and he also provided the foundation for the Geant4 detector simulation programs.

In addition, Dr. Devin Connolly also helped me understand the C++ language when I was new to Geant4. I also thank Konstantin Olchanski, Pierre-André Amaudruz, and Thomas Lindgren for their assistance in setting up the detector efficiency calibration experiments. They also provided me with access to MIDAS (Maximum Integrated Data Acquisition System) to acquire data along with the work station. Without them and Dario Gigliotti, these experiments

may not have occurred.

Dr. Chris Ruiz and the DRAGON group performed the timing experiments with the $LaBr_3$:Ce detectors during the Covid-19 pandemic when I couldn't be there in person. I specifically thank Dr. Chris Ruiz for helping me understand the Geant4 simulation and providing feedback on the thesis; in particular, the timing method calculations. He and Dr. Matthew Williams prepared code in ROOT that allows the timing data to be quickly visualized.

Dr. Chris Ruiz is an external member of the thesis committee. The co-supervisors are Dr. Ian Hartley and Dr. Mark Shegelski. I thank the external examiner Dr. Barry Davids as well as the entire committee for their support on my thesis and for having the thesis defence.

I thank Dr. Dave Hutcheon for also helping me understand the timing method. Furthermore, Dr. Dave Hutcheon's advice has been instrumental in describing how DRAGON determines the resonance energies of radiative capture reactions. Overall, the DRAGON group has been crucial in completing the thesis work and shaping my learning experience. Many of the data tables could not be written without their AutoCAD files.

I thank Dr. Adam Garnsworthy and the GRIFFIN group for letting me borrow a single $LaBr_3$:Ce detector for the detector efficiency measurements in which Victoria Vedia clarified

the dimensions of this detector. In general, I thank TRIUMF for providing me with a tremendous scientific research experience.

I am truly blessed to be surrounded by amazing people with stellar aspirations. Of course, this thesis is dedicated to my family and friends who have supported me every step of the way. It has been a long journey that has been further prolonged by the global Covid-19 pandemic, which requires tremendous patience to complete.

I will always remember these learning moments in the TRIUMF laboratory; the resonance energy measurements and the efficiency calibration runs as well as the DRAGON meetings. I will cherish these memories for a lifetime.

Chapter 1

Introduction

The study of nuclear astrophysics involves nuclear reactions that occur within the stars. These reactions produce the elements which make up the universe to ultimately define its existence. This thesis covers the basic details of this field of study, and the role of the DRAGON (Detector of Recoils and Gammas of Nuclear Reactions) facility in furthering nuclear astrophysical research. As a contribution, this thesis offers an improvement to the DRAGON facility's ability to fulfill its role by recommending the replacement of its Bismuth Germanate (BGO) detector array with a Lanthanum Bromide doped with Cerium ($LaBr_3$:Ce) detector array. The corresponding experimental data and Geant4 simulation data have been summarized.

1.1 Big Bang Nucleosynthesis

The universe is theorized to have been created by a Big Bang in which it expanded from a zero-volume singularity to occupy the current volume over a period of 13.8 billion years. The hydrogen nuclei which are ^{1}H and ^{2}H, and most of the helium nuclei which are ^{3}He and ^{4}He as well as ^{7}Li were created as a result [1]. Nucleosynthesis began when the universal temperature was in between 10^{8} K and 10^{9} K, which occurred between 100 and 1,000 seconds after the Big Bang [2]. As the universe cools further, the nuclear reactions "freeze out" of an equilibrium state since they can no longer be reversed. The specific mechanisms by which nucleosynthesis occurs after the Big Bang are described by models in this paper [2].

1.2 Stellar Nucleosynthesis

1.2.1 The Proton-Proton Chain

The proton-proton chains that are described here represent the process of nucleosynthesis that occurs within stars such as the Sun. ^{4}He which is known as an alpha particle was mostly produced by the proton-proton (pp1) chain reactions that are shown in Equation 1.1,

$$^{1}H + {}^{1}H \Rightarrow {}^{2}H + e^{+} + \nu \quad Q = 1.442\ MeV \tag{1.1a}$$

$$^{2}H + {}^{1}H \Rightarrow {}^{3}He + \gamma \quad Q = 5.493\ MeV \tag{1.1b}$$

$$^{3}He + {}^{3}He \Rightarrow {}^{4}He + {}^{1}H + {}^{1}H \quad Q = 12.861\ MeV \tag{1.1c}$$

where Q represents the energy that is released during this reaction. Two hydrogen atoms combine to form deuterium in which a positron and a neutrino are released. Deuterium combines with hydrogen to form ^{3}He and a gamma ray is released. Two ^{3}He nuclei combine to form ^{4}He and two hydrogen nuclei. The total amount of energy produced by this series of reactions is 26.731 MeV because the reactions in Equation 1.1a and Equation 1.1b occur twice for every time the reaction in Equation 1.1c occurs. However, since some energy is carried away by the two neutrinos, the actual amount of energy available in thermal form is about Q = 26.19 MeV [1].

^{1}H and ^{4}He would be the building blocks for heavier nuclei to ultimately produce the elements that exist today. These heavier nuclei are primarily produced in stars by nuclear reactions along with the further production of ^{4}He. The stars are formed by the gravitational collapse of gaseous clouds which are known as nebulae. As the material of the clouds contracts, its gravitational potential energy is converted to thermal energy which raises the temperature of the cloud. At a critical point where the thermal energy enables the nuclei to get close enough to fuse together, nuclear reactions occur.

These reactions provide radiative pressure to prevent the material from collapsing further, so the volume of the cloud stabilizes and it becomes a star. This stabilization represents a state of equilibrium. After the hydrogen nuclei have been consumed in these reactions, a new series of nuclear reactions may occur if the amount of thermal energy available is sufficient to facilitate them [1].

An alternative nucleosynthesis pathway for the ^{3}He produced by the pp1-chain is the pp2-chain which is summarized by Equation 1.2 as follows.

$$^3He + {}^4He \Rightarrow {}^7Be + \gamma \tag{1.2a}$$

$$^7Be + e^- \Rightarrow {}^7Li + \nu \tag{1.2b}$$

$$^7Li + {}^1H \Rightarrow {}^4He + {}^4He \tag{1.2c}$$

^{3}He combines with ^{4}He to produce ^{7}Be and a gamma ray is released. ^{7}Be undergoes electron capture to become ^{7}Li and a neutrino is released. ^{7}Li combines with hydrogen to produce two alpha particles. When the neutrino energy loss is taken into account, Q = 25.65 MeV [1]. An alternative nucleosynthesis pathway for the ^{7}Be produced by the pp2-chain is the pp3-chain which is summarized by Equation 1.3 as follows.

$$^7Be + {}^1H \Rightarrow {}^8B + \gamma \tag{1.3a}$$

$$^8B \Rightarrow {}^8Be + e^+ + \nu \tag{1.3b}$$

$$^8Be \Rightarrow {}^4He + {}^4He \tag{1.3c}$$

^{7}Be combines with hydrogen to produce ^{8}B and a gamma ray is released. ^{8}B, which has a half-life of 770 milliseconds, undergoes positron emission to release a neutrino to become ^{8}Be. ^{8}Be breaks down into 2 alpha particles and after neutrino energy loss, Q = 19.75 MeV. The pp2 and pp3 chains become more likely to occur than the pp1 chain as the temperature rises above 18×10^6 K. Proton capture becomes more favourable at temperatures above 25 $\times$

10^6 K for ^{7}Be in which the pp3 chain becomes the most likely outcome [1]. Otherwise, the nuclear reactions terminate on the last step of the pp1 chain.

1.2.2 The CNO Cycle

Most stars contain carbon, nitrogen, and oxygen nuclei in addition to hydrogen and helium, since three alpha particles can combine together to form ^{12}C. Two alpha particles would form ^{8}Be and if the ^{8}Be formation rate equals or exceeds its decay rate, this nuclide could undergo the reaction ^{8}Be(α,γ)^{12}C. Figure 1.1 summarizes the major CNO cycles, which show how ^{12}C would be converted to ^{14}N through its first branch and ^{16}O through its second branch [1]. It is likely for ^{15}N to become ^{12}C through the (p,α) reaction. The CNO cycle may have a second branch if ^{15}N undergoes a (p,γ) reaction to become ^{16}O instead. The third branch stems from the ^{17}O(p,γ)^{18}F reaction, which is an alternative to the ^{17}O(p,α)^{14}N reaction. The fourth branch represents the ^{18}O(p,γ)^{19}F reaction, which is an alternative to the ^{18}O(p,α)^{15}N reaction. Figure 1.1 shows the pathways of the CNO cycle, while Table 1.1 lists the hot CNO cycle reactions [1]. As shown in Figure 1.1, carbon, nitrogen, oxygen, or fluorine act as catalysts for these reactions. The typical temperature range for the CNO cycles is on the order of 10^6 K to 10^8 K [1, 3–5].

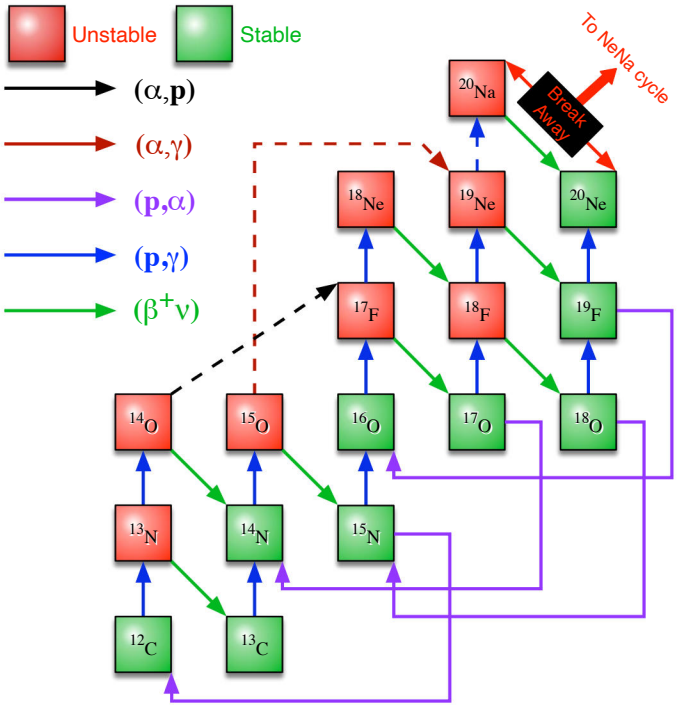

Figure 1.1: The CNO cycles are shown along with additional reaction pathways where broken lines show pathways that lead to the break out reactions.

A small fraction of ^{15}N nuclei that were produced by the hot CNO1 cycle will undergo the ^{15}N(p,γ)^{16}O reaction instead of the ^{15}N(p,α)^{12}C to enter the hot CNO2 cycle. At temperatures above 1.8 $\times$ 10^{8} K, the ^{17}F(p,γ)^{18}Ne reaction becomes more frequent over the ^{17}F($\beta^{+}\nu$)^{17}O decay which leads to the hot CNO3 cycle [1].

The CNO cycle normally does not produce nuclei with an atomic mass at 20 or above. The break out reaction occurs for temperatures above 10^{8} K because at this temperature range, reactions like ^{14}O(α,p)^{17}F, ^{15}O(α,γ)^{19}Ne, and ^{19}Ne(p,γ)^{20}Na can outpace β-decay [1,6]. Under these conditions, ^{20}Ne and ^{20}Na will have no pathways to enter the CNO mass range except for

Table 1.1: The hot CNO cycle reactions.

Hot CNO1	Hot CNO2	Hot CNO3
$^{12}C(p,\gamma)^{13}N$	$^{15}O(\beta^{+}\nu)^{15}N$	$^{15}O(\beta^{+}\nu)^{15}N$
$^{13}N(p,\gamma)^{14}O$	$^{15}N(p,\gamma)^{16}O$	$^{15}N(p,\gamma)^{16}O$
$^{14}O(\beta^{+}\nu)^{14}N$	$^{16}O(p,\gamma)^{17}F$	$^{16}O(p,\gamma)^{17}F$
$^{14}N(p,\gamma)^{15}O$	$^{17}F(\beta^{+}\nu)^{17}O$	$^{17}F(p,\gamma)^{18}Ne$
$^{15}O(\beta^{+}\nu)^{15}N$	$^{17}O(p,\gamma)^{18}F$	$^{18}Ne(\beta^{+}\nu)^{18}F$
$^{15}N(p,\alpha)^{12}C$	$^{18}F(p,\alpha)^{15}O$	$^{18}F(p,\alpha)^{15}O$

photodisintegration. Table 1.2 summarizes the break out reactions [1]. These reactions represent the main transitions to the rapid proton capture process, which is known as the rp-process. ^{20}Na would then undergo the rp-process to produce heavier elements [4].

Table 1.2: The break out reactions.

Sequence 1	Sequence 2	Sequence 3
$^{15}O(\alpha,\gamma)^{19}Ne$	$^{14}O(\alpha,p)^{17}F$	$^{14}O(\alpha,p)^{17}F$
$^{19}Ne(p,\gamma)^{20}Na$	$^{17}F(p,\gamma)^{18}Ne$	$^{17}F(\gamma,p)^{16}O$
	$^{18}Ne(\alpha,p)^{21}Na$	$^{16}O(\alpha,\gamma)^{20}Ne$

1.3 Stellar Evolution

The types of elements that a star produces depend on its mass. Figure 1.2 summarizes the evolution and element production of a star that is 25 times heavier than the Sun. This figure assumes that the star is spherically symmetric [2].

Hydrogen burning is represented by the pp-chains, and hydrogen can also be consumed through the rp-process once a break out from the hot CNO cycle has been achieved. The stages of nucleosynthesis that are shown on Figure 1.2 progressively require a higher temperature and density to produce heavier elements, and these stages become progressively faster until the star becomes a supernova. All stars above 8 times the mass of the Sun will likely undergo the burning stages that are shown in Figure 1.2 [2]. Stellar reactions can create nuclei as heavy as iron. However, charged-particle induced nucleosynthesis beyond iron is no longer copious since the Coulomb barrier hinders charged-particle induced reactions, and the Q-values of these reactions that produce nuclei heavier than iron are negative. Nucleosynthesis beyond iron mainly occurs through neutron capture in either the slow *s*-process or the rapid *r*-process. The *s*-process is where nuclei capture neutrons slower than they β-decay, and the *r*-process is where nuclei capture neutrons faster than they β-decay [1].

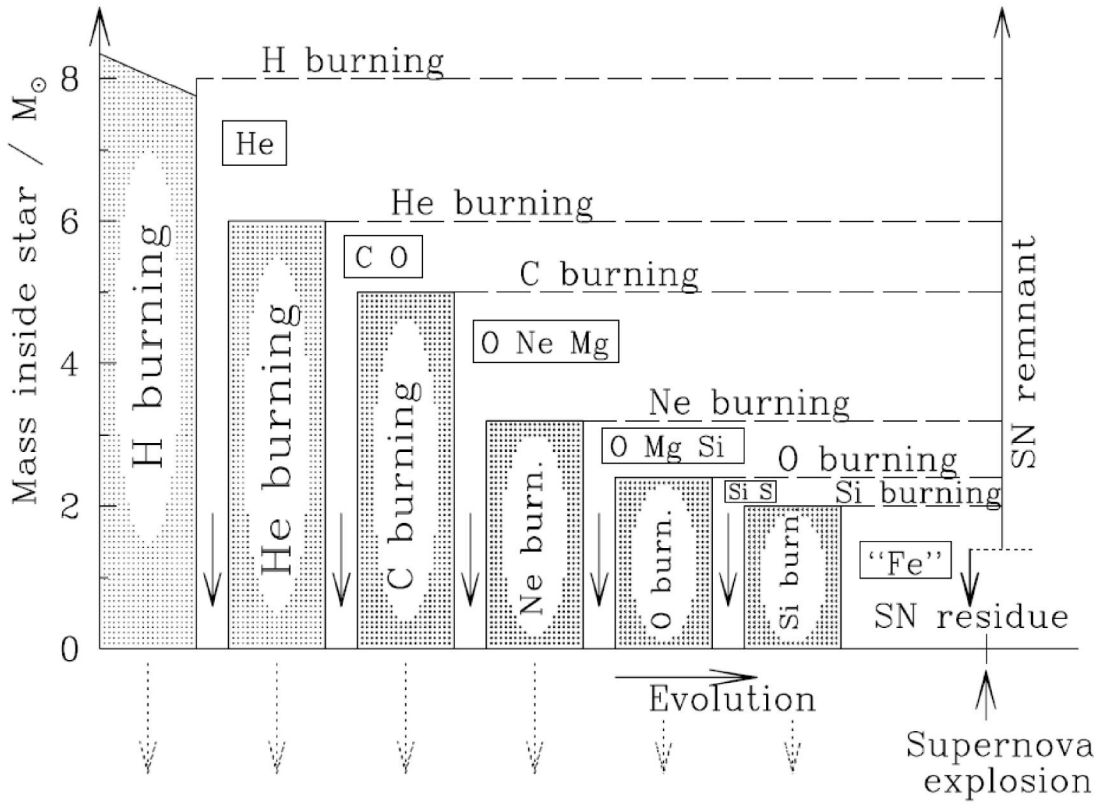

T_C (K)	6×10^7	2×10^8	9×10^8	1.7×10^9	2.3×10^9	4×10^9
ρ_C (g/cm^3)	5	700	2×10^5	4×10^6	10^7	3×10^7
Time–scale	7×10^6 years	5×10^5 years	600 years	0.5 years	6 days	1 day

Figure 1.2: The central star temperature T_c and central star density ρ_c are listed below each element burning stage. When the element has been consumed in the centre, the elements that have been produced form peripheral shells of the star. The downward arrows represent the gravitational contraction of the star between stages. The elements that are produced by each stage are shown beside them. When the star explodes as a supernova, the material that is released is the supernova (SN) remnant, and the supernova core leaves behind a residue.

1.4 Here Enters the DRAGON

The evolution of a star depends on many factors. The competition between the decay rates of various radioactive nuclides and the cross sections of the various nuclear reactions that involve those nuclides determine to a large extent the pathways the star takes during its lifetime as well as its final fate at the end of its life.

The **I**sotope **S**eparator and **AC**celerator (ISAC) facility at the TRI-University Meson Facility (TRIUMF) is designed and built to provide a plethora of beams of radioactive nuclei that are relevant to the stars' evolution so that the cross sections of nuclear reactions involving those nuclei can be measured with reasonable accuracy. Furthermore, the Detector of Recoils And Gammas Of Nuclear reactions (DRAGON) is designed and built to use the radioactive beams produced by ISAC to measure their radiative capture cross sections. Many of the following chapters are dedicated to the description of the ISAC - DRAGON combination.

Chapter 2

Detector Spectroscopy

Research work in nuclear astrophysics requires the use of particle and radiation detectors to study nuclear reactions. The detectors each have specialized material with which particles and radiation interact in a specific manner. These interactions are detected and recorded electronically for subsequent data analysis. The research project that is described in this thesis involves the interactions of gamma rays with BGO and $LaBr_3$:Ce detectors. The three main modes of these gamma ray interactions are the photoelectric effect, Compton scattering, and pair production [7].

2.1 The Photoelectric Effect

The photoelectric effect dominates for photon radiation with less than 100 keV of energy because the cross-section for this process is larger than the other processes in this energy range. The photoelectric effect occurs when a gamma ray deposits all of its energy onto an electron bound in an atom. The gamma ray disappears and the electron exits the atom as a photoelectron with a kinetic energy equal to the difference between the energy of the gamma ray and its binding energy. This process is shown in Equation 2.1,

$$E = h\nu - B \tag{2.1}$$

where E is the kinetic energy of the photoelectron, h is Planck's constant, ν is the gamma ray frequency, and B is the atomic shell binding energy. After the electron escapes, the electrons in the atomic shell rearrange themselves to fill the vacancy. This rearrangement may lead to the release of X-rays or Auger electrons [8]. Isolated free electrons cannot absorb photons, and more than 80% of the photoelectric absorption occurs in the tightly bound K-shell electrons for photons that have more energy than the K-shell binding energy [9]. If nothing escapes from the detector which becomes more likely for large detectors, the energy that it detects should equal the energy of the original gamma ray minus the atomic shell binding energy which is shown in Figure 2.1 [7]. The binding energy is relatively small compared to the gamma ray energy $h\nu$ so the full energy peak is represented as $h\nu$. In experimental spectra, the vertical axis measures the number of gamma ray counts.

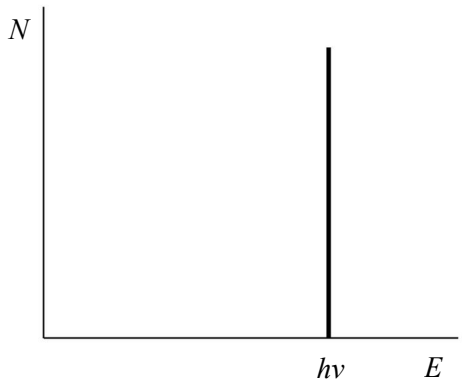

Figure 2.1: The energy spectrum for mono-energetic gamma rays is shown, assuming that all of them interact with the detector by the photoelectric effect, and this detector can detect the gamma ray energy perfectly. The number of counts N is being measured with respect to the incident gamma ray energy E.

2.2 Compton Scattering

Compton scattering occurs when a gamma ray hits a quasi-free electron, which is an electron that is bound but its binding energy has a negligible effect on this interaction. The gamma ray scatters with less energy (i.e. longer wavelength) than what it initially had and the electron recoils. Compton scattering is shown in Figure 2.2 [9]. Equation 2.2 shows the change in wavelength, while Equation 2.3 and 2.4 give the energies of the products of Compton scattering,

$$\lambda' - \lambda = \Delta\lambda = \frac{h}{m_\circ c}(1 - \cos\theta) \tag{2.2}$$

$$E'_e = \frac{E_\gamma^2(1 - \cos\theta)}{m_\circ c^2 + E_\gamma(1 - \cos\theta)} \tag{2.3}$$

$$E'_\gamma = \frac{E_\gamma}{1 + (\frac{E_\gamma}{m_\circ c^2})(1 - \cos\theta)} \tag{2.4}$$

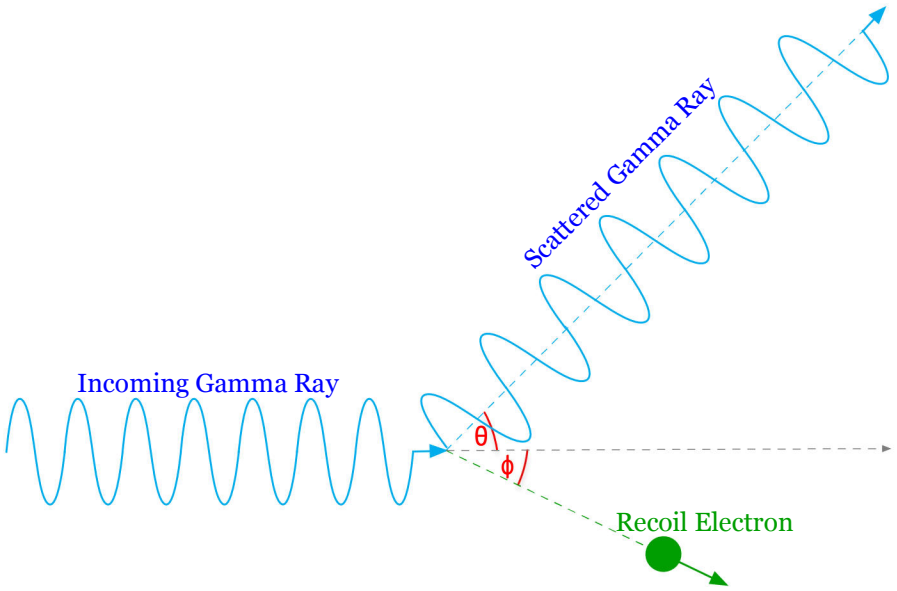

Figure 2.2: The schematic diagram for Compton scattering is shown. The gamma ray scatters at angle θ and the electron recoils at angle ϕ.

where λ and λ' are the wavelengths of the incoming and scattered gamma rays, respectively. E_γ is the initial energy of the gamma ray, $m_\circ c^2$ is the electron rest energy, θ is the scattering angle of the gamma ray, and ϕ is the electron emission angle. E'_e is the kinetic energy of the recoil electron, and E'_γ is the energy of the scattered gamma ray [9].

There are two extreme cases for θ. For $\theta \simeq 0°$, the scattered gamma ray has about the same amount of energy as the incident gamma ray, and the recoil electron has almost no kinetic energy. For $\theta \simeq 180°$, the gamma ray scatters backwards along its direction of incidence, and the electron recoils along this direction of incidence. In this case, the maximum amount of energy that could be transferred to the electron is given to it. If the incident gamma ray energy is much larger than the electron rest energy, the difference in energy between the incident

gamma ray and the recoil electron will approach a constant value of 0.256 MeV. Figure 2.3 shows the ideal energy spectrum for gamma rays that interact with the detector through the photoelectric effect and Compton scattering [7].

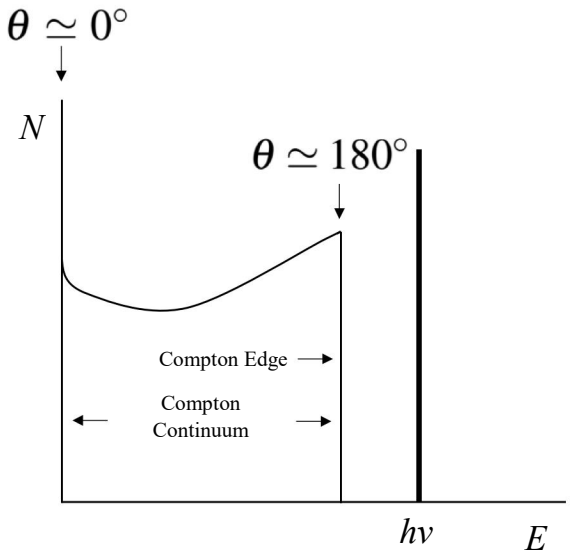

Figure 2.3: The energy spectrum for mono-energetic gamma rays is shown, assuming that all of them interact with the detector by the photoelectric effect and Compton scattering. The two extreme cases for θ are shown, where $\theta \simeq 0^\circ$ corresponds to no energy transfer to the recoil electron, and $\theta \simeq 180^\circ$ corresponds to the maximum energy transfer to the recoil electron. This detector is also assumed to detect the gamma ray energy perfectly.

2.3 Pair Production

Pair production is a process in which a gamma ray near a nucleus creates an electron-positron pair. Conservation of energy dictates that for the pair production to take place, the gamma ray must have an energy of at least 1.022 MeV; double the rest mass energy of an electron (a photon with an energy of 1.022 MeV is in the gamma ray region of the electromagnetic spectrum). Any extra energy will be given to the pair as kinetic energy. Usually, a second particle must be close to the gamma ray for the pair production process to conserve momentum.

The second particle can be an atomic nucleus and the minimum gamma ray energy E_G in MeV that is required for pair production depends on the mass M of the second particle as shown in Equation 2.5,

$$E_G = 1.022\left(1+\frac{m_\circ}{M}\right)\ [MeV] \tag{2.5}$$

where $m_\circ$ is the electron mass. Equation 2.5 confirms that gamma rays must have energies slightly above 1.022 MeV for pair production to occur near a nucleus, and they must have energies around 2.044 MeV for pair production to occur near an electron [9]. After the electron and positron are produced, the positron will rapidly lose most of its kinetic energy, and then it will likely annihilate or combine with an electron in the scintillator medium to produce two gamma rays, each with an energy of 0.511 MeV [7]. To conserve momentum, these two gamma rays would travel in opposite directions and form an 180° angle between their trajectories.

Depending on the material and volume of the detector, one or both of the gamma rays that are produced by positron annihilation could escape it. If both gamma rays are detected, the full energy of the original gamma ray that underwent pair production is detected, and it is registered as a count in the full energy peak on the energy spectrum. If one of the gamma rays escape, 0.511 MeV less than the full energy of the original gamma ray would be detected, and this event would be counted as part of the single escape peak. If both gamma rays escape, 1.022 MeV less than the full energy of the original gamma ray is detected, and this event would be counted as part of the double escape peak. Figure 2.4 shows the representative energy spectrum for a detector where both gamma rays have escaped. In this figure, $m_{\circ}c^2$ is equal to 0.511 MeV [7].

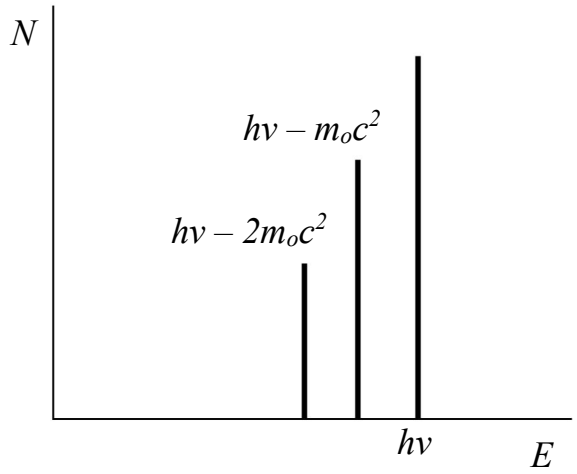

Figure 2.4: The energy spectrum for mono-energetic gamma rays is shown, assuming that all of them interact with the detector through pair production. This detector is also assumed to detect the gamma ray energy perfectly.

2.4 Gamma Ray Attenuation

A tight beam of gamma rays absorbed and scattered in a medium is described by the exponential attenuation law Equation 2.6,

$$I = I_0 e^{-n\sigma x} = I_0 e^{-\mu x} \tag{2.6}$$

where I_0 is the initial number of gamma rays or the initial beam intensity, I is the attenuated beam intensity, n is the number density of the medium in units of m^{-3}, σ is the total cross section of the medium in units of m^2, μ is the linear attenuation coefficient of the medium (or normally just the attenuation coefficient) and it has units of m^{-1}, and x is the length in m traversed by the beam into the medium [8].

It is sometimes easier to use the mass attenuation coefficient μ_m and the area density of the absorbing material z as shown in Equation 2.7,

$$I = I_\circ e^{-\mu_m z} \tag{2.7}$$

where μ_m is in units of (m^2/kg) and z is in units of (kg/m^2). The mass attenuation coefficient μ_m can be expressed as Equation 2.8,

$$\mu_m = \frac{\mu}{\rho} = \frac{n\sigma}{\rho} = \frac{N_A \sigma}{M_A} \tag{2.8}$$

where ρ is the material volume density, N_A is the Avogadro number, and M_A is the atomic mass of the material. The reciprocal of the linear attenuation coefficient is the mean free path, which is the average distance that a gamma ray travels before it interacts with the material.

This quantity is also known as the attenuation length. The mass attenuation coefficient is more commonly used because it can be used independently from the material density. Figure 2.5 shows how the probabilities of the photoelectric effect, Compton scattering, and pair production vary with the gamma ray energy and the atomic number of the medium [7]. These probabilities also depend on the atomic cross-sections of these three processes.

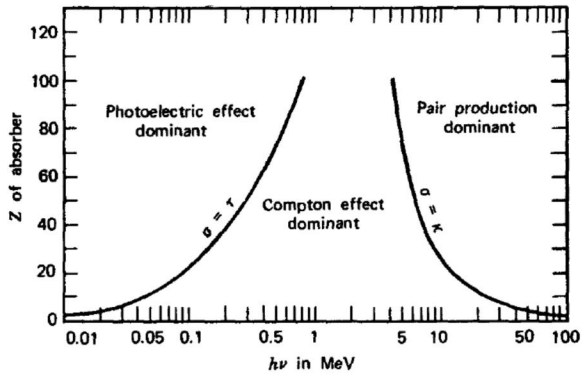

Figure 2.5: The regions where the photoelectric effect, Compton scattering, and pair production are most likely to occur are shown. On the curve where $\sigma = \tau$, the photoelectric effect and Compton scattering are equally likely to occur. Likewise, on the curve where $\sigma = \kappa$, Compton scattering and pair production are equally likely to occur.

Since there are multiple layers of materials in a detector, Equation 2.6 could be generalized as in Equation 2.9,

$$I = I_o e^{-X} \ , \ X = \sum_i \mu_i x_i \tag{2.9}$$

and using Equation 2.8, the mass attenuation coefficient is then given by

$$\mu_m = N_A \sum_i \frac{\beta_i \sigma_i}{M_{Ai}} \tag{2.10}$$

where the sum is carried over all of the materials, and β_i is the fraction of the i^{th} material.

Equation 2.10 would express the total attenuation of the gamma ray beam through the detector. The detector's crystal usually forms the thickest layer of material that the gamma rays will encounter, and the other layers of material are designed to be relatively thin. In fact, they are often designed to be reflective walls on the detector to prevent gamma rays from escaping the detector [7]. In this case, μ is the mass attenuation coefficient of the scintillator crystal.

If the crystal is a compound, which is the case for BGO and $LaBr_3$:Ce, μ is calculated as the weighted sum of the mass attenuation coefficients of its elements μ_i as in Equation 2.11,

$$\mu = \sum_i \beta_i \mu_i \tag{2.11}$$

where β_i is the mass fraction of each element in the compound [9]. Charged particles such as electrons would pass through the same number of electrons in similar materials that have the same mass thickness. The range of these particles and the stopping power of the material do not significantly vary for materials that have about the same atomic number [7].

2.5 The Detector Design

The detectors that are being investigated are the hexagonal prism BGO detector, which is part of the DRAGON detector array, and a single cylindrical $LaBr_3$:Ce detector, which was borrowed from the GRIFFIN (Gamma-Ray Infrastructure For Fundamental Investigations of Nuclei) facility. BGO and $LaBr_3$:Ce are inorganic scintillator crystals that absorb the energy

from the incident gamma rays and produce photons in the visible region [7,10]. The inorganic scintillator crystals have a conduction band and a valence band. Electrons in the conduction band are not tightly bound to their atoms and can easily move around. Electrons in the valence band are tightly bound. The two bands are separated by an energy region where electrons could not occupy; this region is called "Band Gap", "Energy Gap", or "Forbidden Gap". Electrons in the valence band can only jump to the conduction band if given energy that is equal to or larger than the energy width of the band gap. When such an event takes place, a vacancy or hole is left in the valence band. The atom that has the vacancy is actually positively charged. In an electric field, the hole seems to move along the direction of the electric field, i.e. in the opposite direction of an electron. However, in reality the hole does not move, but what happens is that an electron moves from an atom and fills in the vacancy, thereby creating a hole or a vacancy somewhere else. When a gamma ray is absorbed in a pure scintillator crystal, electrons in the valence band can be elevated to the conduction band, leaving a vacancy behind in the valence band. Normally, an electron falls into the valence band emitting a photon. This process, however, is inadequate for the efficient detection of gamma rays. Due to the energy gap size, few photons are emitted and the photons are not in the visible wavelength. These problems can be alleviated by doping the pure scintillator crystal with a certain material that can introduce energy levels within the energy gap of the crystal. For example, NaI is doped or activated by a small amount of thallium (Tl) and $LaBr_3$ is activated by cerium (Ce). Figure 2.6 shows the energy structure of a pure inorganic scintillator crystal and the activated one.

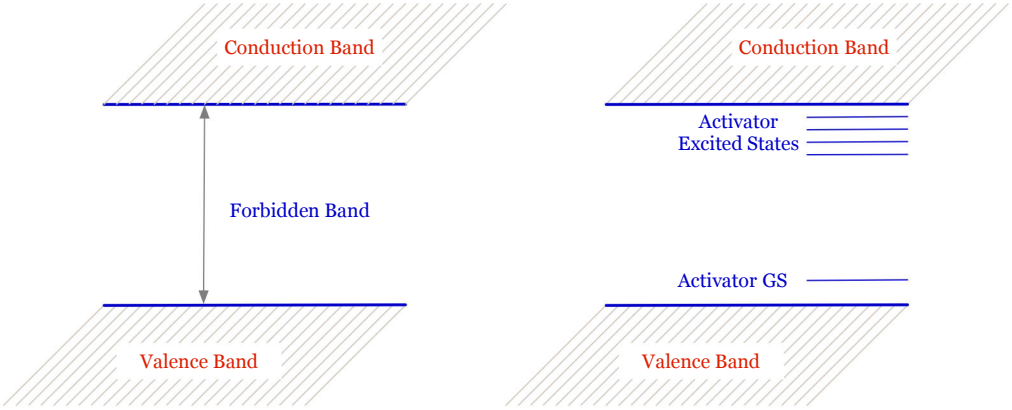

Figure 2.6: The energy structure of an inorganic scintillator crystal with and without activators is shown. GS stands for ground state.

The activator's energy levels introduced in the forbidden gap allows for the production of photons with smaller energies [10]. In other words, they shift the photon spectrum toward the visible region (i.e. longer wavelength). Furthermore, the number of photons per gamma ray is now much larger than those produced in the pure scintillator crystal. These last two properties help improve the energy resolution and efficiency of inorganic scintillator detectors.

Each scintillator crystal produces photons with a characteristic spectrum. This spectrum is identified by the wavelength that has the maximum intensity (λ_{max}). For example, λ_{max} = 480 nm for BGO, 415 nm for NaI, and 380 nm for $LaBr_3$:Ce [11]. The process is similar for organic scintillators where gamma rays excite molecules from their ground state to their excited states. When these electrons return to their ground state through fluorescence, photons are emitted [7].

In regards to the $LaBr_3$:Ce detector, the natural Lanthanum element has two isotopes; ^{138}La with an abundance of 0.088% and ^{139}La with an abundance of 99.912% and is stable. ^{138}La is radioactive with a half-life of 1.03×10^{11} years. Figure 2.7 shows the decay scheme of ^{138}La [12]. The decay of ^{138}La produces 2 gamma rays with energies 788.7 keV and 1435.8 keV. Bromine, on the other hand, has two stable isotopes.

The rate of the gamma rays produced by ^{138}La in the $LaBr_3$:Ce detector is about 153 counts/second for the $LaBr_3$:Ce detector. This internal radiation can be useful as a consistent way of energy calibration. However, the internal radiation can be a problem for low count rate experiments. The latter problem can be alleviated by background subtraction.

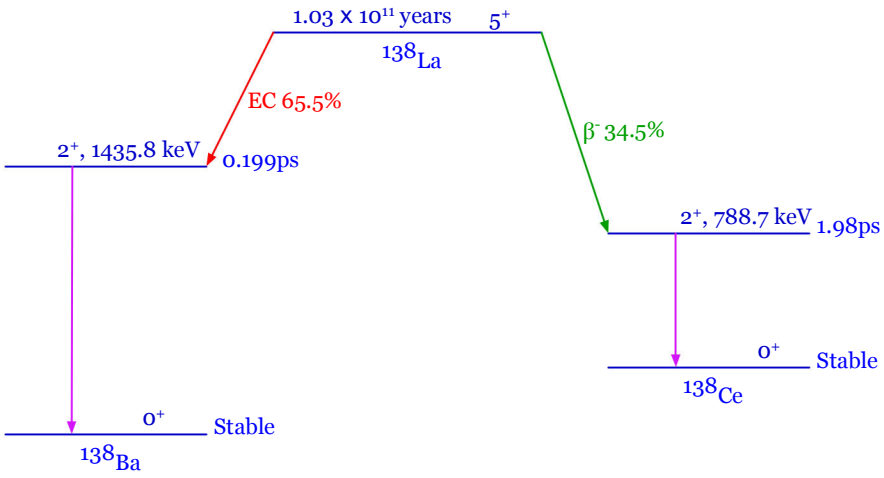

Figure 2.7: The decay scheme of ^{138}La is shown, where it has a 65.5% probability of undergoing electron capture to an excited state of ^{138}Ba which relaxes by releasing a 1435.8 keV gamma ray. Alternatively, ^{138}La has a 34.5% probability of undergoing β-minus decay to ^{138}Ce which relaxes by releasing a 788.7 keV gamma ray. The total angular momentum of each state is given as well as the half-life and the parity.

The scintillator crystal must be connected to a photomultiplier tube to count the produced scintillations for data. The photomultiplier tube is a vacuum that includes a transparent window to the photon spectrum produced by the scintillator crystal, photocathode, a series of dynodes, and an anode as shown schematically in Figure 2.8 [13–15].

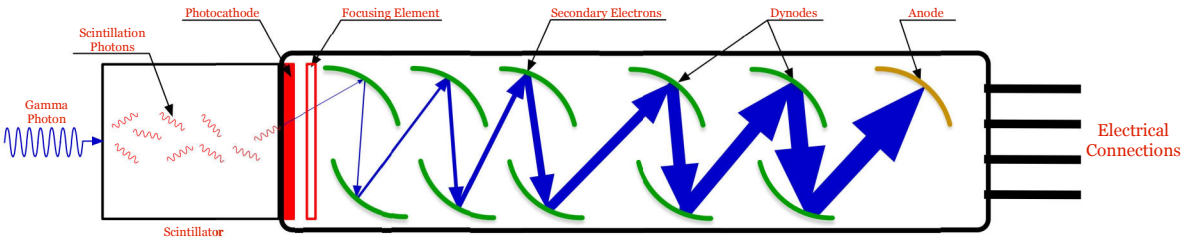

Figure 2.8: A schematic diagram of a detector is shown.

The phototube is set up such that the photocathode is at a high negative electric potential of about 1,000 V. The first dynodes are set up with a less negative potential relative to the photocathode. The potential of each successive dynode will have less negative potential than the one before it. The anode potential is very close to ground.

When scintillation photons leave the crystal and enter the phototube, they hit the photocathode to release a group of primary electrons. This process is repeated as primary electrons are then focused and accelerated toward the first dynode to release a larger group of secondary electrons. Those secondary electrons are in turn accelerated toward the second dynode to release more secondary electrons. This process continues until the secondary electrons reach the anode. The number of electrons arriving at the anode will be much larger than the original

number of the primary electrons released at the photocathode, and as a result a sharp current pulse is produced by the anode. If n is the number of the secondary electrons released by each dynode per incident electron and assuming that the phototube has k dynodes, then the overall gain of the tube is n^k [13]. A 12-dynode tube that yields 4 secondary electrons per dynode per incident electron has an overall gain of $\approx 10^7$. The entire process is very fast since it occurs within nanoseconds. The amplitude of the current pulse produced by the anode is directly proportional to the number of secondary electrons that arrive at the anode. The number of secondary electrons at the anode is directly proportional to the number of primary electrons released by the photocathode. Furthermore, the number of primary electrons is directly proportional to the number of scintillation photons that reach the photocathode, and the number of scintillation photons is directly proportional to the amount of energy lost by the incident gamma ray inside the scintillator crystal. If the gamma rays seen by the detector lose *all* of their energies inside the crystal, then the amplitude of the current pulse is directly proportional to the gamma ray energy. In actual experiments, one has to find out the proportionality constant by using a source that produces a well defined gamma ray energy. In short, a good detector response must be linear i.e. as explained above, the amplitude of the anode signal must be directly proportional to the energy lost by the incoming gamma ray in the crystal. Real detectors are not linear but they are very close to being linear.

Some of the BGO crystals are coupled to the Hamamatsu R1828-01 and the rest are coupled to Electron Tubes Ltd. (ETL) 9214 photomultiplier tubes in which both photomultiplier

tube models are in operation during the experiments [3]. Table 2.1 summarizes the specifications of the Hamamatsu R1828-01 model [16]. Table 2.2 summarizes the specifications of the ETL 9214B model [17]. The quantum efficiency is the percentage of the photons that undergo the photoelectric effect at the photocathode.

Table 2.1: The properties of the Hamamatsu R1828-01 model at 25°C.

Photocathode Material	Bialkali
Photocathode Diameter (mm)	46
Window Material	Borosilicate Glass
Gain	2.0×10^7

Table 2.2: The properties of the ETL 9214B model around room temperature.

Photocathode Material	Bialkali
Photocathode Diameter (mm)	46
Window Material	Borosilicate Glass
Best Quantum Efficiency (%)	30
Best Gain	30×10^6

The photomultiplier tube window is generally made of ultraviolet-transparent glass, which could be composed of borosilicate or lime [13, 16, 17]. The photomultiplier tube is sealed in a vacuum by these materials because only visible light photons are allowed to enter it. Detectors usually have about 9-10 stages of dynodes, although the Hamamatsu R1828-01 and ETL 9214B models have 12 stages [13, 16–18].

The BGO scintillator crystal that is used by DRAGON is encased by a layer of aluminium and a reflective layer made of magnesium oxide [3]. The reflective layer is designed to prevent gamma rays from escaping the detector after they enter it [7]. Figure 2.9 shows the schematic

diagram of a BGO detector that is being used by DRAGON [19]. There are two types of BGO detectors that are being used; one of them was manufactured by Bicron and the other one was manufactured by Scionix.

The hexagonal aluminium casing for the Bicron detectors is 0.535 mm thick and it covers the whole detector. The hexagonal aluminium casing for the Scionix detectors is 0.5 mm thick and it only covers the scintillator crystal. A cylindrical aluminium casing covers the photomultiplier tube. Figure 2.9 shows the Scionix design [19]. Both Bicron and Scionix have designed the BGO crystal to be a hexagonal prism with a length of 7.62 cm and an incircle radius of 2.79 cm [3].

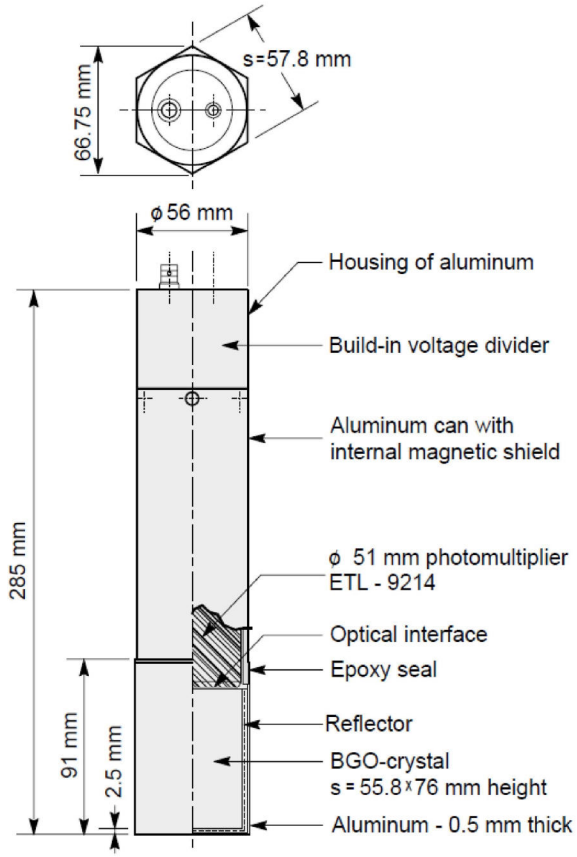

Figure 2.9: The DRAGON BGO detector is shown. This diagram has not been drawn to scale.

Figure 2.10 shows the schematic diagram of a $LaBr_3$:Ce detector that was borrowed from GRIFFIN. This detector was manufactured by Saint-Gobain and it is called BrilLanCe^{TM}380 [11].

This detector is attached to the Hamamatsu R2083 photomultiplier tube which has 8 dynode stages. Its specifications are given in Table 2.3 [20]. The Hamamatsu R1828-01, ETL 9214B, and the R2083 models are designed to convert incident photons with wavelengths between 300 nm and 650 nm into electrons to generate signals [16, 17, 20].

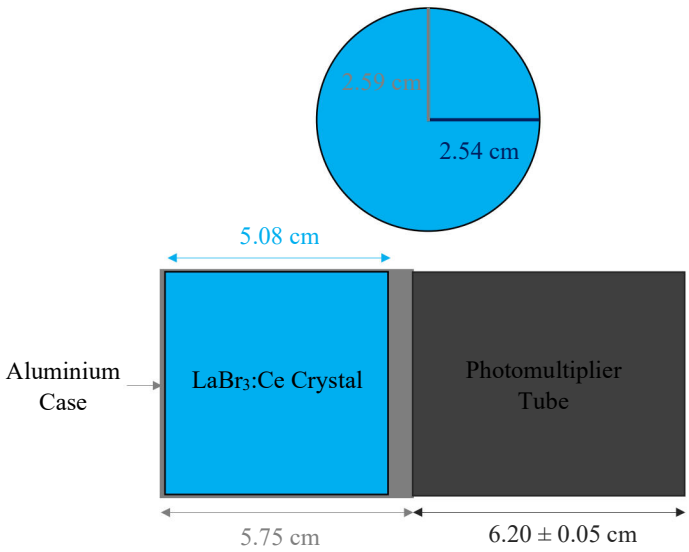

Figure 2.10: The $LaBr_3$:Ce detector is shown with the scintillator radius and the aluminium case radius, where the aluminium case covers the scintillator. This diagram has been approximately drawn to scale.

Table 2.3: The properties of the Hamamatsu R2083 model at 25°C.

Photocathode Material	Bialkali
Photocathode Diameter (mm)	46
Window Material	Borosilicate Glass
Gain	2.5×10^6

2.6 Energy Resolution

If all of the gamma rays with the same energy going through a detector produce exactly the same number of secondary electrons at the anode of the phototube, then there would be no spread in the energies measured by the detector and the energy spectrum will appear as Figure 2.4, i.e. the energy resolution of the detector is infinitesimally small. However, all processes

from the production of scintillation photons to the production of primary electrons and secondary electrons are dependent on the incident energy, direction, and the medium. As a result, the size of the signal produced by the phototube anode varies from one gamma ray to another, even though they all have the same energy. The variation varies from detector to detector, from very small in solid state detectors to relatively large in some scintillators like NaI(Tl). Other factors contributing to this variation are, for example, the existence of slow and fast processes in the detector and the intrinsic afterglow in some scintillator crystals. A review of the detector energy resolution is given in a paper by Moszyński, *et al.* [21].

The electron relaxation and the subsequent photon emission processes that occur in the scintillator generate statistically varying numbers of photons. When these photons are converted to electrons, the number of electrons vary. As a result, after the dynodes multiply the electron population, the subsequent electrical signals vary in amplitude. Through this process, different energy values for a single gamma ray energy are obtained. The quantum mechanical nature of the crystal, photocathode, and photomultiplier tube materials provide these statistical variances. The quantum mechanical nature of the crystal in particular provides its intrinsic energy resolution. These different energy values deviate from the mean, which is the true gamma ray energy. Crystal impurities could worsen or improve the energy resolution by an unknown amount, which is a source of random error. When these variations are taken into account, the overall energy resolution is obtained. Therefore, the number of electrons that are released within the photomultiplier tube to generate an electrical signal may not exactly

be proportional to the original gamma ray energy [22]. Equation 2.12 expresses the intrinsic energy resolution as the energy variation ΔE divided by the energy E,

$$\left(\frac{\Delta E}{E}\right)^2 = (\delta_c)^2 + (\delta_p)^2 + (\delta_t)^2 \tag{2.12}$$

where δ_c is the intrinsic energy resolution of the crystal, δ_p is the variation in the number of photoelectrons that the photocathode releases, and δ_t is the variation in the number of photoelectrons that are collected by the photomultiplier tube [22]. Figure 2.11 illustrates the concept of energy resolution [23]. The value of ΔE is provided by the Full Width Half Maximum (FWHM), which is the full width of the peak at half of the peak height. For large numbers of gamma ray events, the energy peaks that are centred at E are expected to resemble Gaussian distributions. The energy resolution improves as the statistical variances decrease, and the energy peaks become sharper.

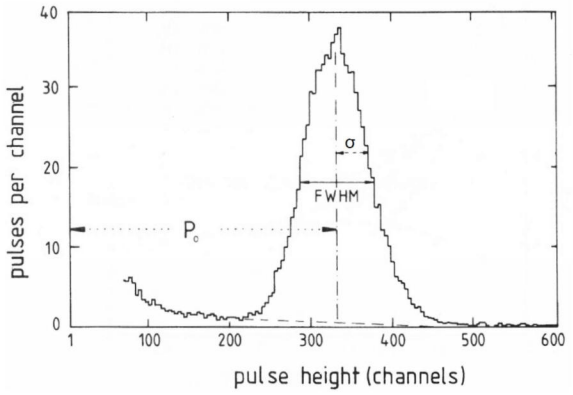

Figure 2.11: A plot of gamma ray energies versus counts shows the concept of energy resolution. $P_\circ$ is the position of the pulse peak. The peak position corresponds to the energy value of the peak channel. The standard deviation $\sigma = \frac{FWHM}{2\sqrt{2ln(2)}}$. The energy resolution $E_r = \frac{\Delta E}{E} = 100(FWHM/P_\circ)$.

Small detectors have dimensions of around 2 cm or less, and large detectors have dimensions with values over 10 cm. The BGO and $LaBr_3$:Ce detectors are thereby considered to be detectors of intermediate size. Figure 2.12 shows what the energy spectra are expected to look like for detectors of intermediate size when the photoelectric effect, Compton scattering, and pair production occur in which energy resolution effects are included. Only the full energy peak and Compton scattering are visible for gamma ray energies that are below twice the electron rest energy, which is represented by the expression $2m_{\circ}c^2$. The single escape peak and double escape peak appear for gamma rays that have significantly more energy than 1.022 MeV [7].

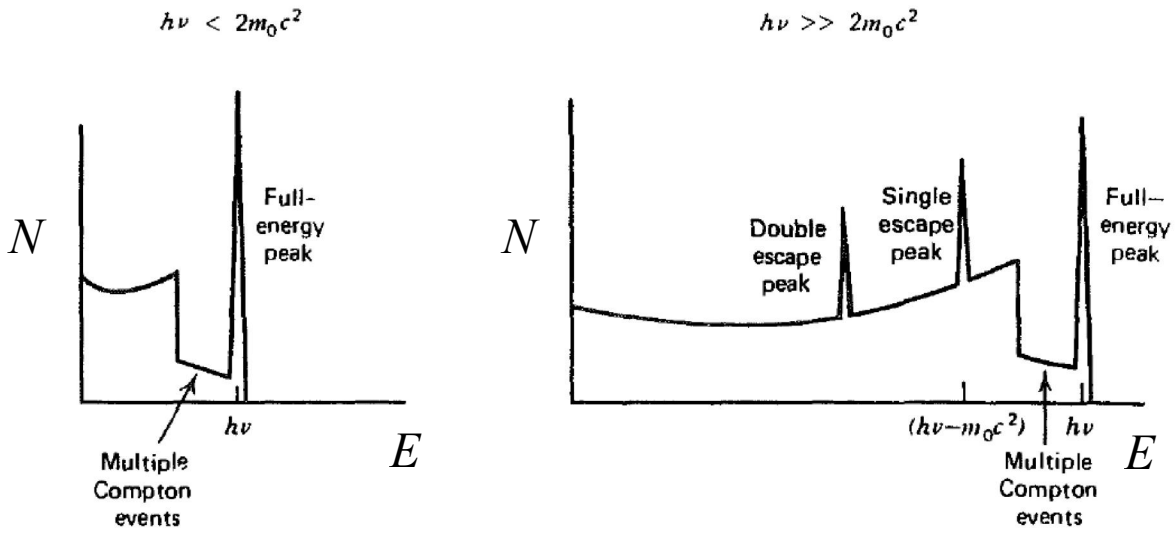

Figure 2.12: The energy spectrum for monoenergetic gamma rays which includes the main types of gamma ray interactions is shown. The number of counts N is being measured with respect to the incident gamma ray energy E.

2.7 Detector Timing Considerations

The time resolution also depends on the nature of the scintillator crystals [24]. Gamma rays excite the electrons in the scintillator molecules in which photons are emitted upon electron relaxation. This time period is represented as the scintillator rise time R. The differences in the rise times for different gamma ray detection events lead to a spread in the time of these events about a mean time, and the FWHM of this spread is the time resolution. The time spectrum would be similar to what is observed on Figure 2.11, with the number of entries being plotted with respect to time instead of energy. The photons provide a light pulse for the scintillator, and the time required for this light pulse to decrease to $\frac{1}{e}$ of its maximum value is the decay time D [7]. Equation 2.13 summarizes the scintillator response as follows,

$$I = I_{\circ}(e^{-t/D} - e^{-t/R}) \tag{2.13}$$

where I is the light yield at a given time, $I_{\circ}$ is the initial light yield which corresponds to the peak of the light pulse, and t is the elapsed time. Although this equation is used for organic scintillators, similar equations can be used for inorganic scintillators [25]. After gamma ray detection, the detector cannot detect another one until the current gamma ray signal has been mostly processed during the dead time. The intrinsic time resolution of the detector and the accompanying data acquisition system contribute to the dead time [7]. Figure 2.13 shows an example of a timing spectrum taken for a $LaBr_3$:Ce detector by using a ^{137}Cs source, which provides 0.662 MeV gamma rays [25]. The decay time may not be Gaussian since the detector

has a slow decay component in addition to the relatively fast decay time. However, Equation 2.13 is expected to be a good approximation in most cases since a single decay time dominates although Figure 2.13 shows how this equation can be modified to better model the data.

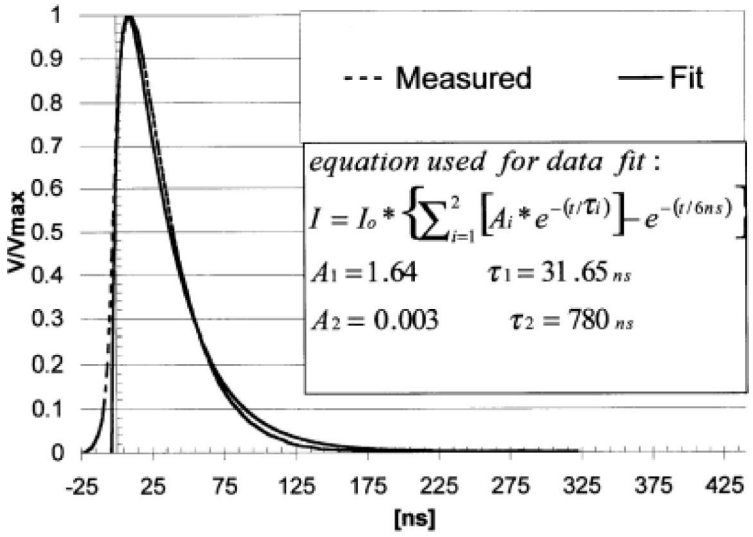

Figure 2.13: The 0.662 MeV timing spectrum for the $LaBr_3$:Ce detector is shown, where the fit function takes into account both the fast and slow decay components. The signal has been normalized so 1 corresponds to the peak value, and the pulse intensity is plotted with respect to the time elapsed in nanoseconds.

2.8 BGO and $LaBr_3$:Ce Detector Comparison

Table 2.4 summarizes some of the physical properties of the BGO and $LaBr_3$:Ce crystals [11, 15, 25–38]. The energy resolution values were taken for 0.662 MeV gamma rays, which is the characteristic radiation of ^{137}Cs [12]. The BGO detector could have an energy resolution of 11% to 13% at room temperature which worsens as the gamma ray energy decreases [31].

The energy resolution value given at 6.5±0.2% was taken at the temperature of liquid nitrogen [29]. On the contrary, the $LaBr_3$:Ce energy resolution of around 3% was taken at room temperature [34].

Table 2.4: The physical properties of the BGO and $LaBr_3$:Ce crystals.

Material	$LaBr_3$:Ce	BGO
Density ($\frac{g}{cm^3}$)	5.08	7.13
Effective Atomic Number	48.3	74.2
Decay Time (ns)	∼16	300
Time Resolution (ps)	260	1300
Light Output (photons/keV)	∼60	≥6
Band Gap (eV)	3.24	4.2
Peak Emission Wavelength (nm)	380	480
Overall Energy Resolution (%)	∼3	≥ 6.5±0.2
Linear Attenuation (μ)(cm^{-1})	0.47	0.95
Hygroscopic?	Yes	No

In addition to measuring the rise time, the time resolution can be measured by using the two back-to-back annihilation gamma rays produced by a positron emitting source like ^{22}Na in time coincidence. The energy resolution can be measured by using well known gamma rays produced by sources like ^{60}Co and ^{137}Cs. These sources produce gamma rays with well defined energies of 1.17 MeV, 1.33 MeV, and 0.662 MeV. The time resolution of the $LaBr_3$:Ce detector doped by 5% Ce was measured in coincidence with a BaF_2 detector by using 0.511 MeV gamma rays that were provided by ^{22}Na where 260 ps is the FWHM value [34]. The time resolution for a BGO crystal was taken in coincidence with a CsF scintillator for the gamma rays emitted by ^{60}Co, which have energies of 1.17 MeV and 1.33 MeV [12]. In this case, the FWHM value is 1300 ps [37]. All of the $LaBr_3$:Ce detector properties apply onto detectors that have been doped with a mole fraction of 5% Cerium, except for the 3.24 eV band gap for detectors that have been doped with a mole fraction of 0.5% Cerium [38]. The linear attenuation coefficients are taken in response to 0.511 MeV gamma rays [32].

The scintillator crystal should be coupled to the photomultiplier tube through a transparent material that has the same index of refraction as the crystal. This is done to minimize the internal reflection so most of the photons would travel to the photocathode [7]. The $LaBr_3$:Ce crystal is hygroscopic, which means it tends to absorb moisture from the air [10].

BGO was chosen as the scintillator material for the DRAGON detector array because it was an affordable material with a low decay time and a high density. Its decay time provides a good time resolution, and its high density provides a high interaction probability between

the BGO molecules and the gamma rays [3]. The latter property is known as the gamma ray capture efficiency. It will be replaced by $LaBr_3$:Ce to improve the energy and time resolution at the expense of the gamma ray capture efficiency due to its lower density.

Chapter 3

DRAGON

Although individual detectors can be used to detect charged particles and gamma rays, they usually can only detect one type of particle at a time. A series of detectors is normally required to fully investigate a nuclear reaction. DRAGON is a facility designed to fully investigate reactions of astrophysical importance by taking into account the gamma rays that are produced as well as the residual nuclei which are also known as recoils. The "head of" the DRAGON facility is composed of a gas target box and a BGO detector array. The "body of" DRAGON is a mass separator composed of two pairs of electric and magnetic dipoles, quadrupoles, and adjustable vertical and horizontal slits. At the "tail of" DRAGON, there is a detector for the heavy recoils such as a double sided silicon strip detector (DSSSD) or an ionization chamber (IC) [19]. DRAGON alone is not capable of studying astrophysical nuclear reactions. It needs beams of heavy radioactive ions that are accelerated to energies that correspond to

temperatures in the stars. The ISAC (**I**sotope **S**eparator and **AC**celerator) facility provides such beams to the DRAGON experiments. Even though ISAC is an integral part of DRAGON, it also serves other experimental facilities. This chapter provides a brief description of the various components of DRAGON.

3.1 ISAC-I

The ISAC facility at TRIUMF is composed of two accelerator systems known as ISAC-I and ISAC-II along with beam lines for various types of experiments. This facility is designed to deliver intense radioactive and stable beams with masses and energies suitable for nuclear astrophysics research. ISAC-I delivers radioactive beams of nuclei with atomic masses up to A = 30 and energies in the range of 0.15 - 1.5 MeV/nucleon. ISAC-II provide beams whose masses range up to A = 150 with energies of at least 6.5 MeV/nucleon [39–41]. Figure 3.1 shows a part of the ISAC-I accelerators with all of the optical elements used to transport

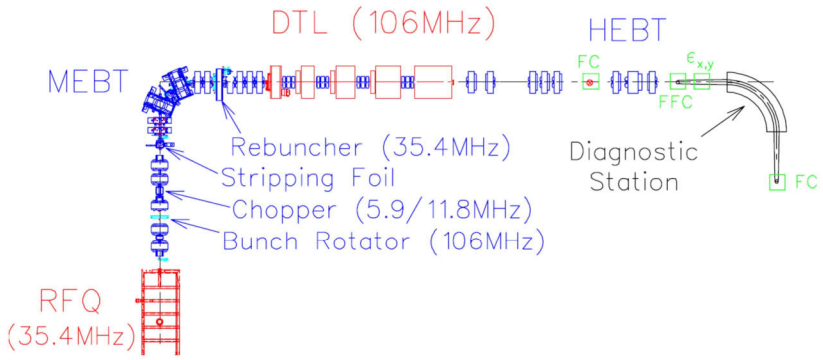

Figure 3.1: A section of the ISAC-I accelerators is shown.

and focus the heavy ion bunches [39]. The ISAC system produces and isolates short lived heavy ion bunches by bombarding specific targets with the protons produced by TRIUMF's main cyclotron. The target choice depends on which particular ion species is required for a particular experiment. The ions are then accelerated to a low energy of about 2 keV/nucleon and directed toward the accelerator components of ISAC. ISAC-I has two accelerators; the first is an 8 m long Radio Frequency Quadrupole (RFQ) that uses an electric field created by the quadrupoles and a 35.4 MHz radio frequency electric field to compress the heavy ion bunches. The RFQ accelerates the heavy ion bunch to an energy of 150 keV/nucleon. The ion bunches are then directed to the second stage accelerator called the Drift Tube Linac (DTL). The DTL is composed of 5 drift tube cavities and is capable of accelerating the 150 keV/nucleon ions from the RFQ up to 1.53 MeV/nucleon. The RFQ mass-to-charge acceptance is limited to $A/q \leqslant 30$, while the DTL is limited to $3 \leqslant A/q \leqslant 6$. For ions with A/q larger than 6, a carbon foil is placed between the two accelerators to strip electrons from the ions thus increasing q and reducing A/q to a value within the acceptance of the DTL. As shown in Figure 3.1, the entire ISAC line contains many beam optical elements to direct, focus, and shape the ion beams to suit the various requirements of DRAGON experiments. When the magnetic dipole at the diagnostic station is turned off, the beam proceeds to DRAGON or it can be switched to ISAC-II for further acceleration. In addition, there is an Off Line Ion Source (OLIS) that produces stable beams for experiments that need them [39–41].

3.2 The Gas Target

The most common way of studying properties of nuclei and their nuclear interactions is by bombarding a collection of those nuclei (target) with accelerated light particles (projectiles) like p, n, α, etc. This process is called forward kinematics.

Many astrophysically important nuclear reactions are of the type (p,γ) and (α,γ) on radioactive nuclei, since they are involved in the pathways of nucleosynthesis. It is not possible to study such nuclear reactions in forward kinematics because the radioactive nuclei under investigation decay rapidly. For instance, the half-life of a ^{21}Na target is 22.49 seconds so it cannot be made into a target [12].

Furthermore, radioactive targets would cause radiation damage to the target containment structure so it would have to be replaced often. To circumvent these issues, such nuclear reactions are performed in reverse kinematics, whereby the radioactive nuclei are used as projectiles rather than a target and the light particles are used as targets. Figure 3.2 illustrates this process [3].

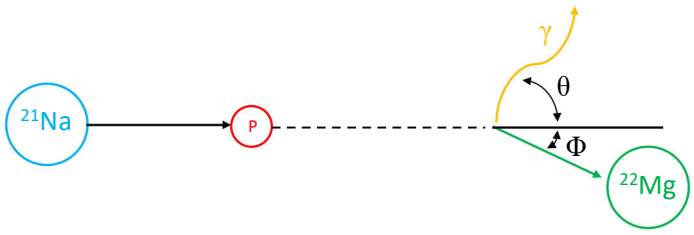

Figure 3.2: This figure shows how to study the radiative capture of a proton by ^{21}Na in reverse kinematics in which an accelerated radioactive ^{21}Na beam bombards a proton gas target. A gamma ray and a ^{22}Mg recoil are produced.

DRAGON is designed to study radiative capture reactions on radioactive nuclei. DRAGON's target nuclei are either hydrogen or helium in which the hydrogen atom has its electron removed. This explains why the target is made up of protons in Figure 3.2. Generally, the chemical and physical conditions of the target in any nuclear reaction experiment are determined by a compromise among many conflicting factors. Its chemical and physical conditions are normally chosen to achieve the best possible experimental results. The most common targets used are solid targets. However, gas and liquid targets have been used in many experiments. In the case of DRAGON, the most important factors are high energy resolution and high reaction rate. The first factor requires minimum energy loss by the beam while traversing the target.

This means that the incoming beam must encounter the least amount of material and that includes the target material itself. High reaction rates require high target density to reduce data collection time and achieve low statistical errors. Further complications arise from the fact that DRAGON's incoming beams are composed of heavy ions. Heavy ions lose energy very rapidly while travelling in a medium compared to beams of light particles like protons, alpha particles, and neutrons for example. It is then obvious that liquid, solid, very thin self-supporting foils, and sealed gas targets are unquestionably unsuitable for DRAGON experiments.

A windowless gas target is a target in which the gas is contained in a region with a relatively high pressure in the middle of the beam tube that is under very low pressure. In the DRAGON

gas target, the pressure at the center is ≈ 5 Torr while the pressure upstream and downstream of the target region is $< 10^{-6}$ Torr. Figure 3.3 shows the gas target design which includes its trapezoidal component where the nuclear reactions occur [19]. Figure 3.4 shows the path of the beam through the gas target [42]. Table A5 in Appendix A provides its dimensions. The gas of the target is contained in a trapezoidal region within the box. The beam enters the trapezoidal region through a 6 mm diameter aperture and exits through an 8 mm diameter aperture. The two apertures are 11 cm apart[1] [43].

A series of five large Root Blowers and seven turbomolecular pumps along with a trap containing a X-13 (Zeolite) molecular sieve at liquid nitrogen temperature form a system to differentially pump, recirculate, and clean the gas. This system helps maintain the gas pressure inside the trapezoidal region at 0.2-10 Torr and less than 3×10^{-6} Torr within the gas target box and in the upstream and downstream beam pipes [19]. Two silicon detectors (called elastic monitors) are included in the gas target box to detect the hydrogen or helium nuclei that are recoiling from the elastic scattering of beam ions off target particles. One of the silicon detectors observes this at 30° and the other at 57°. The elastic scattering rate is a direct measure of the beam current if the gas pressure is known.

In general, the angle of the recoil ϕ_R is given by Equation 3.1 [43].

$$\phi_R = \arctan\left[\frac{\sin\theta_\gamma}{\frac{c\sqrt{2mE}}{E_\gamma} - \cos\theta_\gamma}\right], \tag{3.1}$$

[1] For a detailed description of the entire windowless gas target system see [19,43].

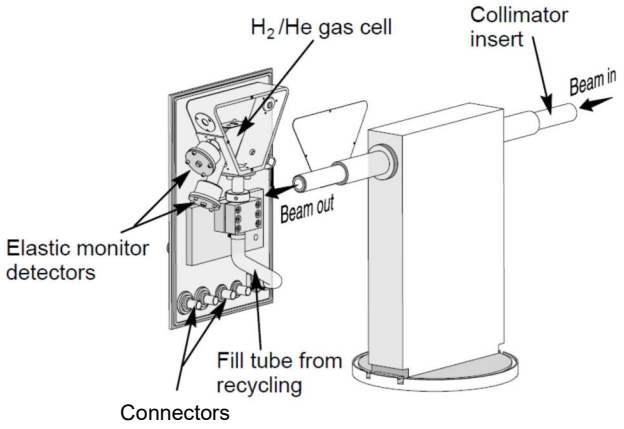

Figure 3.3: The major components of the gas target box and the beam direction are shown.

The scattering angle of the gamma ray θ_γ is given by Equation 3.2 where E_γ represents the gamma ray energy.

$$\theta_\gamma = \arccos\left[\frac{E_\gamma}{c\sqrt{2mE}}\right] \tag{3.2}$$

The angle of the recoil ϕ_R reaches its maximum when the gamma ray scatters at 90° relative to the beam [43]. In Equation 3.3, for the specific cases where $\theta_\gamma = 0°$ or 180° and $\phi_R = 0°$, the recoil momentum p_R is expressed in terms of the beam ion momentum:

$$p_R = p\left(1 \pm \frac{E_\gamma}{c\sqrt{2mE}}\right) \tag{3.3}$$

In Equation 3.1, 3.2, and 3.3, m is the mass of the radioactive beam ions, $p = \sqrt{2mE}$ is the momentum of the beam, E is the kinetic energy of the radioactive beam ions, and c is the speed of light. These equations apply in the lab frame [43]. Therefore, the exit aperture must be slightly larger than the entrance aperture to take into account the difference in momenta between the recoils and the radioactive beam as they leave the gas target box.

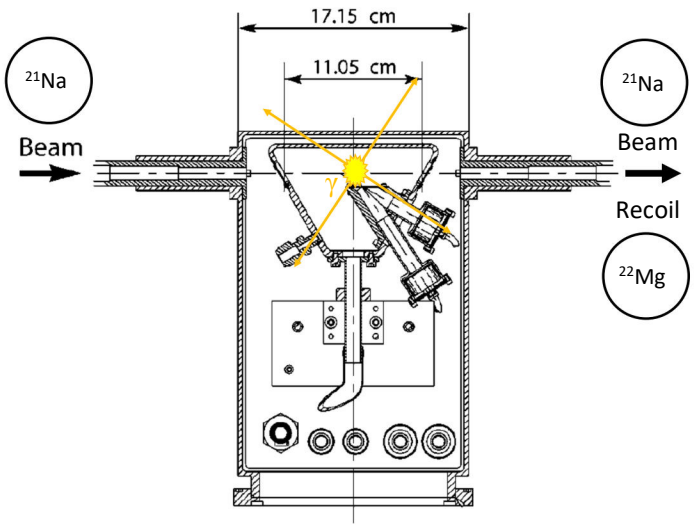

Figure 3.4: The radioactive beam enters the gas target box and interacts with the gas within the trapezoidal cell. The residual beam and the recoils exit the gas target box. The gamma rays (γ) are detected by the BGO detector array.

3.3 The Gamma Detector Array

The hexagonal shape of the BGO detectors makes it possible to arrange them in an array without overlaps or gaps. To optimize gamma ray capture, it is important to design the array in such a way to cover the largest possible solid angle around the gas target box. The BGO array covers 89-92% of the solid angle [3]. The scintillator crystals of the array all face the gas target box. Figure 3.5 provides an illustration of the array and the gas target box [43, 44].

Each detector has an incircle diameter of 5.58 cm and a length of 28.5 cm [3, 43]. Each detector in the array is assigned a number from 1 to 30, to indicate their individual positions. Seven of these detectors are made by Bicron, and the other twenty-three as well as a spare detector are made by Scionix [3]. Figure 3.6 shows the detectors in the DRAGON array with

their representative numbers. The detectors may be switched around which explains why six Bicron detectors are shown. Table A7 and A8 in Appendix A provide the details on the detector positions. In an experiment, these detectors may be rearranged. To cut down the intensity of the 0.511 MeV gamma rays, lead shielding is placed at the entrance of the gas target box which makes it necessary to move back two detectors. Consequently, about 3% of the array coverage is lost. These background gamma rays are created by the β-plus decay of the radioactive beam ions. The positrons that emerge from this decay annihilate electrons in aluminium to produce these gamma rays [3].

Gamma rays interact with the BGO detectors through either the photoelectric effect, Compton scattering, or pair production [7]. In most cases, the gamma rays can undergo Compton scattering and pair production multiple times to produce multiple electrons before they disappear. The gamma ray interaction events are separated from the background by using the coincidence timing method with their corresponding recoils. The details of the electronics that are used by DRAGON to obtain the data are described by Christian *et al.* (2014) [45].

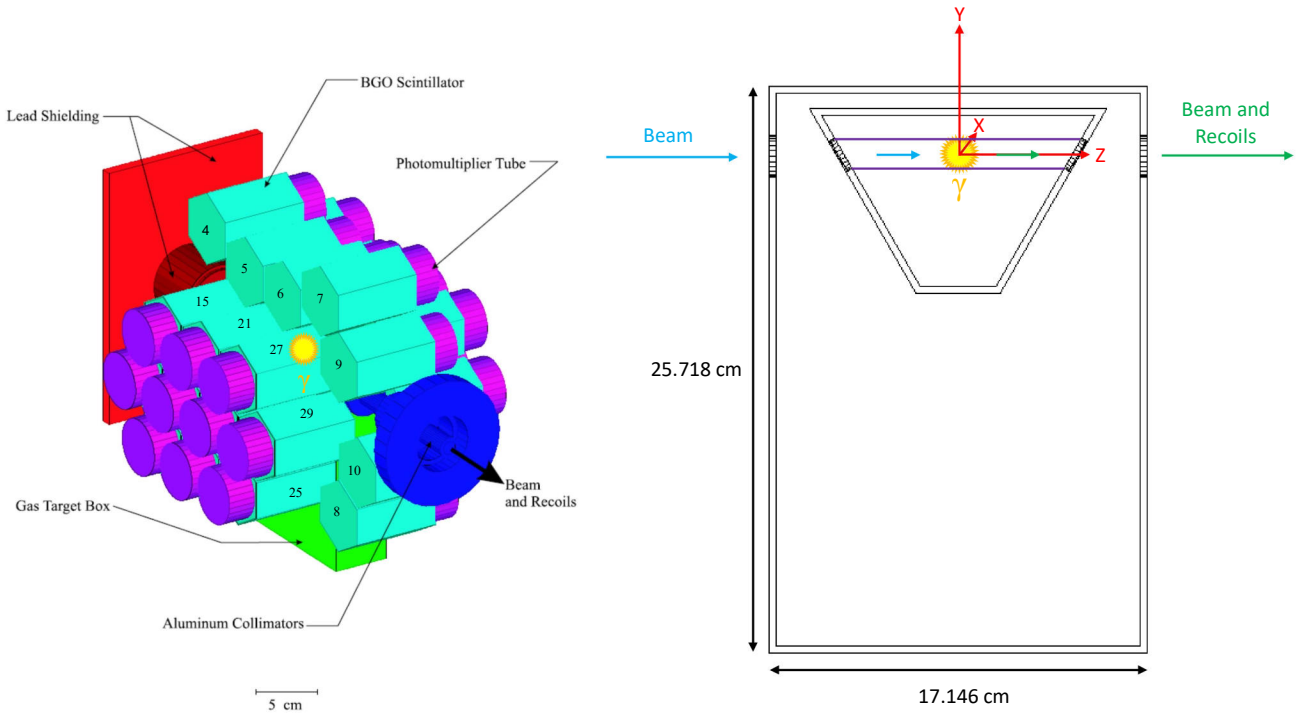

Figure 3.5: The left side shows the BGO array surrounding the gas target box. The lead shielding surrounds the side of the gas target box where the beam enters it. The detectors are numbered based on their positions. The right side shows a simulation of the gas target box and its components. The beam is propagated along the region that is marked by the purple lines. Gamma rays (γ) and recoils are emitted upon nuclear reactions between the beam and the gas.

(a) (b)

Figure 3.6: (a) The left-hand side of the DRAGON array is shown along with the crown detectors and the straddling detectors. (b) The right-hand side of the DRAGON array is shown.

3.4 The Electromagnetic Separator

The nuclear reactions of interest at DRAGON have very small cross sections; as a result, the intensity of the product ions are of the order of 10^{10} - 10^{16} times lower than that of the incoming beam. In addition, due to the use of reverse kinematics (see Table 3.1), the angular separation between the incoming beam ions and the recoiling ions is extremely small; it can be less than a degree [19]. The electromagnetic separator (EMS) is designed to reduce the beam contamination by at least 10^{10}, and further suppression is provided by the time coincidence between the gamma ray events that are detected by the BGO detectors and the recoil events that are detected by the end detectors placed at the final focus of the mass separator (see section 3.5). Electric and magnetic dipoles are used to separate the recoils from the radioactive beam.

Table 3.1: The forward and reverse kinematics of $^{14}\mathrm{N}(p,\gamma)^{15}\mathrm{O}$ and $^{27}\mathrm{Al}(p,\gamma)^{28}\mathrm{Si}$.

Forward Kinematics		Reverse Kinematics	
$^{14}\mathrm{N}(p,\gamma)^{15}\mathrm{O}$	$^{27}\mathrm{Al}(p,\gamma)^{28}\mathrm{Si}$	$p(^{14}\mathrm{N},\gamma)^{15}\mathrm{O}$	$p(^{27}\mathrm{Al},\gamma)^{28}\mathrm{Si}$
$E_p = 2.0\ MeV$	$E_p = 2.0\ MeV$	$E_{\mathrm{N}} = 2.0\ MeV$	$E_{\mathrm{Al}} = 2.0\ MeV$
$\theta_{max}(\gamma) = 180^\circ$	$\theta_{max}(\gamma) = 180^\circ$	$\theta_{max}(\gamma) = 180^\circ$	$\theta_{max}(\gamma) = 180^\circ$
$\phi_{max}(\mathrm{O}) = 8.59^\circ$	$\phi_{max}(\mathrm{Si}) = 12.7^\circ$	$\phi_{max}(\mathrm{O}) = 1.86^\circ$	$\phi_{max}(\mathrm{Si}) = 2.1^\circ$

The mass separator is composed of two identical stages. Each stage has a magnetic and an electric dipole with quadrupoles in between the dipoles and the two stages. The magnetic dipole of the first stage (MD1) begins the separation with the magnetic force [3]. When a charged particle with charge q, mass m, and velocity v enters a magnetic field B that is

perpendicular to the velocity, a force of magnitude Bqv acts on the particle. The direction of the force is perpendicular to the plane that contains v and B. This force tends to change the direction of the velocity without changing its magnitude. As a result, the particle will move in a circle with radius R_M and the magnetic force acts as the required centripetal force mv^2/R_M in Equation 3.4,

$$R_M = \frac{p}{qB} \tag{3.4}$$

where p is the momentum [3]. Since the central momenta of the radioactive beam and the recoils are very close, the difference in their charges would cause them to have different radii of curvature. As a result, the recoils and the radioactive beam ions will have different trajectories. Mechanical narrow slits can then intercept and block most of the beam particles while allowing most of the recoils to pass. Quadrupoles (Quads) then focus the trajectories of the particles towards the electrostatic dipole of the first stage (ED1). The electric dipoles work in a similar way to the magnetic dipoles. If a charged particle moves in an electric field E in a direction perpendicular to the field direction, an electric force qE acts on the particle in a direction that is perpendicular to the plane formed by the E and v, i.e. the electric force in which qE becomes the centripetal force required to move the particle in a circle with radius R_E. This is shown in Equation 3.5,

$$R_E = \frac{mv^2}{qE} \tag{3.5}$$

where a difference of twice the kinetic energy to charge ratios between the beam and the recoils provide slightly different radii of curvature. Once again, mechanical slits are used to

reject the beam ions while allowing the recoils through. The actions of the first stage are shown schematically in Figure 3.7. Table 3.2 and Table 3.3 summarize their properties [43].

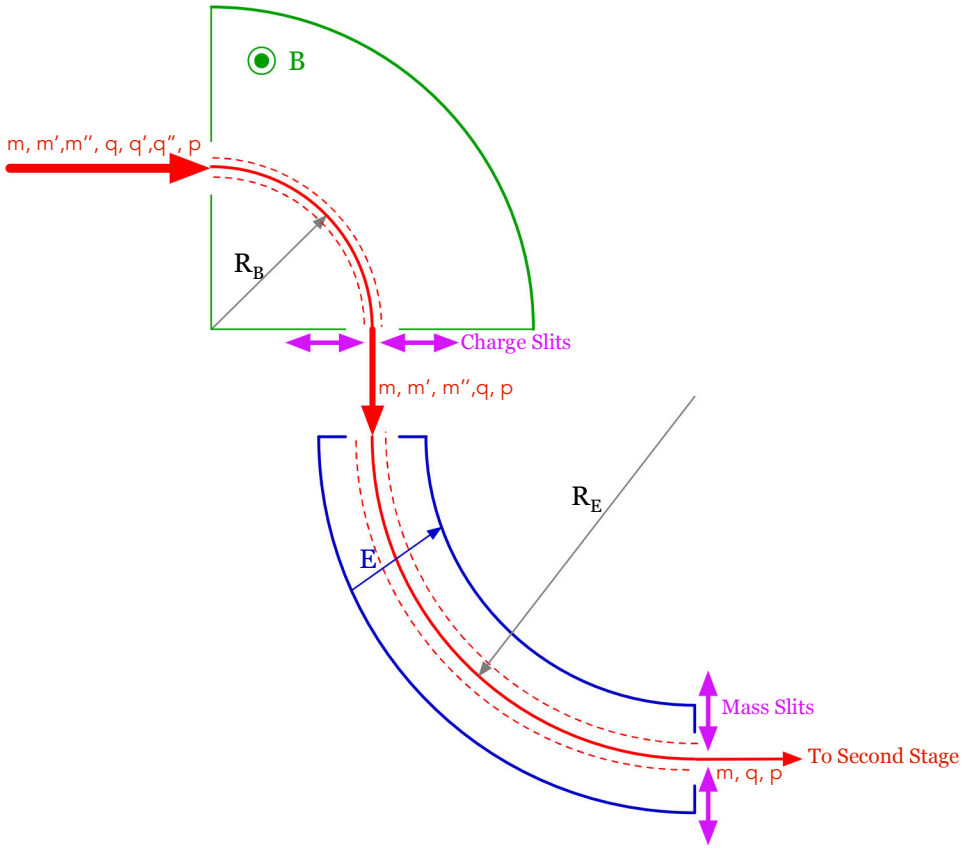

Figure 3.7: The actions of the first stage dipoles without the quadrupoles are shown. *B* is coming out of the page.

Beam suppression factors of about 10^{-9} to 10^{-11} have been achieved, depending on the beam ion energy. This means that the number of radioactive beam ions has been reduced by 10^{9} to 10^{11}.

Table 3.2: The properties of the magnetic dipoles.

Component	MD1	MD2
Bending Radius	1.00 m	0.813 m
Bending Angle	50°	75°
Maximum Field	5.9 kG	8.2 kG

Table 3.3: The properties of the electrostatic dipoles.

Component	ED1	ED2
Bending Radius	2.00 m	2.50 m
Bending Angle	20°	35°
Maximum Voltage	±200 kV	±160 kV

The quadrupoles assist in depositing the recoils onto either the DSSSD or the IC, or a hybrid detector which functions as both the DSSSD and the IC. The distance from the gas target box to a recoil detector is 21 m [19].

3.5 Double Sided Silicon Strip Detector (DSSSD)

Beam suppression by the mass separator may not be enough for certain reactions. Further suppression can be achieved by demanding a time coincidence between gamma detectors and a detector for the recoils and the remaining beam ions. Such a detector is placed at the final DRAGON focus. DRAGON uses several end detectors to help in further suppressing the leaked beam that may overwhelm the recoils. Experiments require one or more detectors depending on the overall purpose and the experimental conditions. The DSSSD is described here. The separator's bending elements (MDs and EDs) are designed to bend the particle

trajectories horizontally, which makes the DSSSD detector suitable for many experiments. The DSSSD is basically made of strips of reverse biased semiconductor p-n junctions [46].

3.5.1 The Band Theory of Solids

Values of electrical conductivity of various solids vary over a very wide range, from very small to extremely high. The former are the insulators and the latter are the conductors. Somewhere in the middle, there are solids that are neither good conductors nor good insulators, and they are called semiconductors. This category of materials is characterized by tetravalent atoms. A tetravalent atom has four electrons in its valence shell. Trying to understand the electrical property and other properties of solids using the atomic structure alone does not work. The band theory of solids is successful in explaining these properties. It is a quantum mechanical theoretical frame work that considers the interactions of electrons within their own atoms as well as with electrons in the surrounding atoms. The details of the theory are beyond the scope of this thesis so only a very short summary of its results is provided here.

Due to the complex interactions in a solid lattice, the energy levels that are available to be occupied by electrons in a solid become bands of very closely spaced energy levels that are separated by a region devoid of any energy levels. Figure 3.8 shows the basic structure of a solid (a), a solid at 0 K where all electrons are occupying the valence band (b), and the solid in (b) at a higher temperature (c), where some electrons acquired thermal energy and were able to jump to the conduction band across the gap.

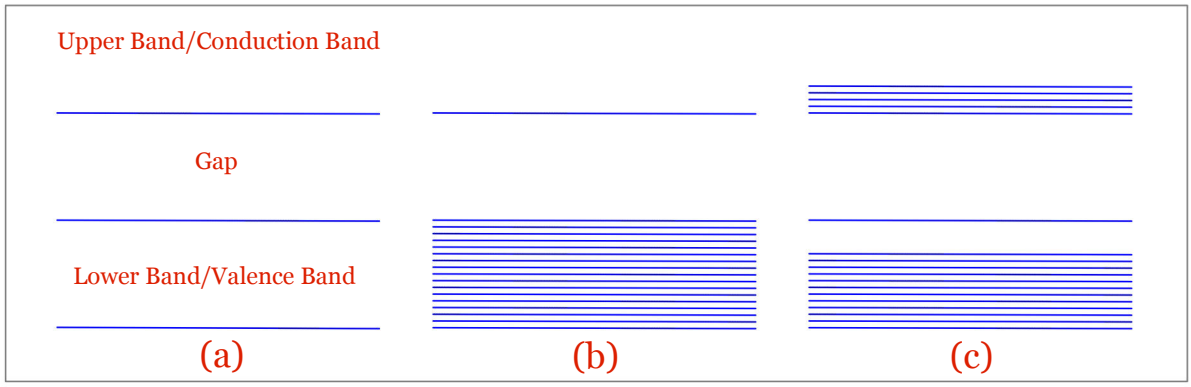

Figure 3.8: (a) The general energy structure of a solid. (b) A solid at 0 K. (c) The same solid in (b) at a higher temperature.

In general, the width of the gap determines whether the solid is an insulator, conductor, or semiconductor. Figure 3.9 illustrates a semiconductor. This distinction is shown in Figure 3.10 where (a) is a conductor where the gap width is zero, (b) is also a conductor where the conduction and valence bands overlap since some electrons are free, and (c) is an insulator where the gap width is so large the valence bound electrons cannot jump to the conduction band. Depending on the width of the gap, a solid can insulate at low temperatures but become a conductor at higher temperatures. For example, (d) is a semiconductor where the gap is small[2]. Pure semiconductors are not very useful as electronic devices. However, doping a semiconductor can be a means to have control of its conductivity.

[2]For comparison, the gap width for diamond, silicon, and germanium are 5.47 eV, 1.1 eV, and 0.66 eV, respectively [30]. Diamond is a good insulator but it will start conducting at temperatures higher than 63,000 K.

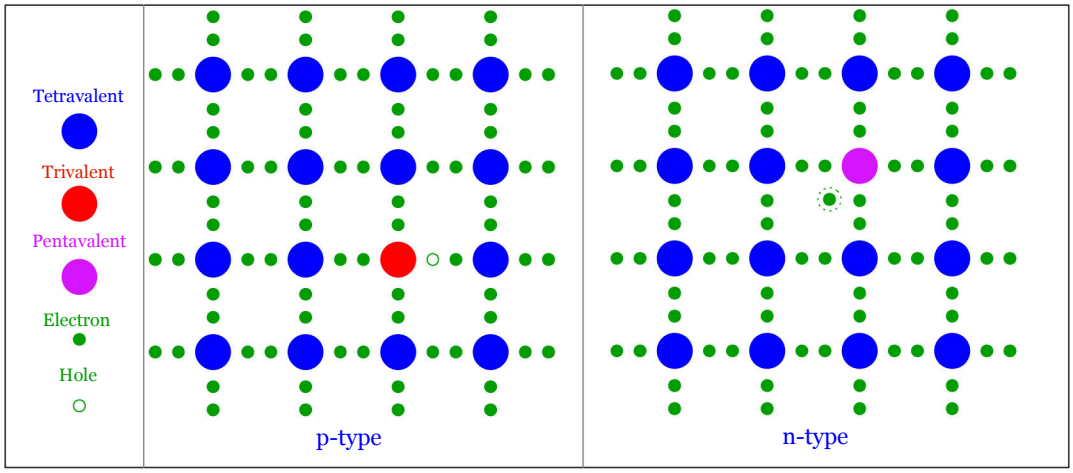

Figure 3.9: The atomic structure of a doped semiconductor is shown.

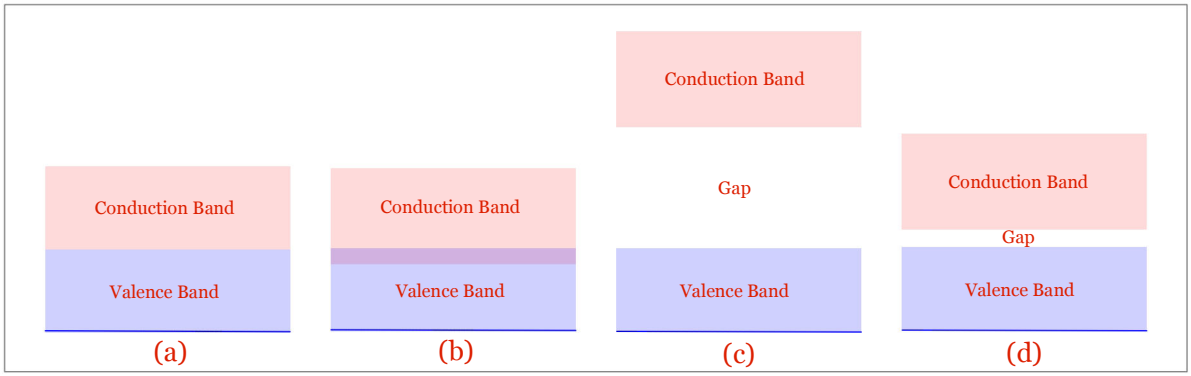

Figure 3.10: (a) and (b) Conductor, (c) Insulator, (d) Semiconductor.

As mentioned before, semiconductor solids are made of tetravalent atoms. Doping a pure semiconductor like silicon with a very small amount of a pentavalent material like phosphorus or with a trivalent material like boron will alter the band structure of silicon. Every phosphorus atom in the semiconductor lattice will contribute a loosely bound electron to the silicon crystal. The extra electrons will occupy an energy level that lies very closely below the conduction band. Those electrons can easily move to the conduction band and conduct electricity under

the influence of an electric field. This kind of doped semiconductor is called an n-type semiconductor because electric conduction is carried by the movement of the negatively charged electrons. The extra energy level below the conduction band is normally called the "donor level".

On the other hand, if a pure semiconductor is doped with trivalent atoms like boron, the doped sites will have vacancies that can be occupied by electrons. Those vacancies are formed in a discrete energy level just above the valence band. Electrons from the valence band can be easily transported through the material under the influence of an electric field, which creates new vacancies. Under the influence of a uniform electric field, electrons move in one direction while the vacancies move in the opposite direction. The vacancies are called "holes" and they can be treated as electrons but with opposite charge and a slightly different mobility. Such a material is called a p-type semiconductor because it contributes to the conductivity through the filling of holes by electrons, with positively charged holes as the majority charge carriers. In the p-type semiconductor, the extra energy level above the valence band is normally called the "acceptor level". Figure 3.11 shows the band structure of n-type and p-type semiconductors.

The number of free electrons or holes in a doped semiconductor is determined by the amount of doping material. Under an electric field, those electrons or holes carry the majority of the electric current so they are called majority carriers. Due to the possibility of thermal excitations, there is always a small number of electrons and holes that roam the crystal and contribute a flowing electric current. Therefore, they are called minority carriers.

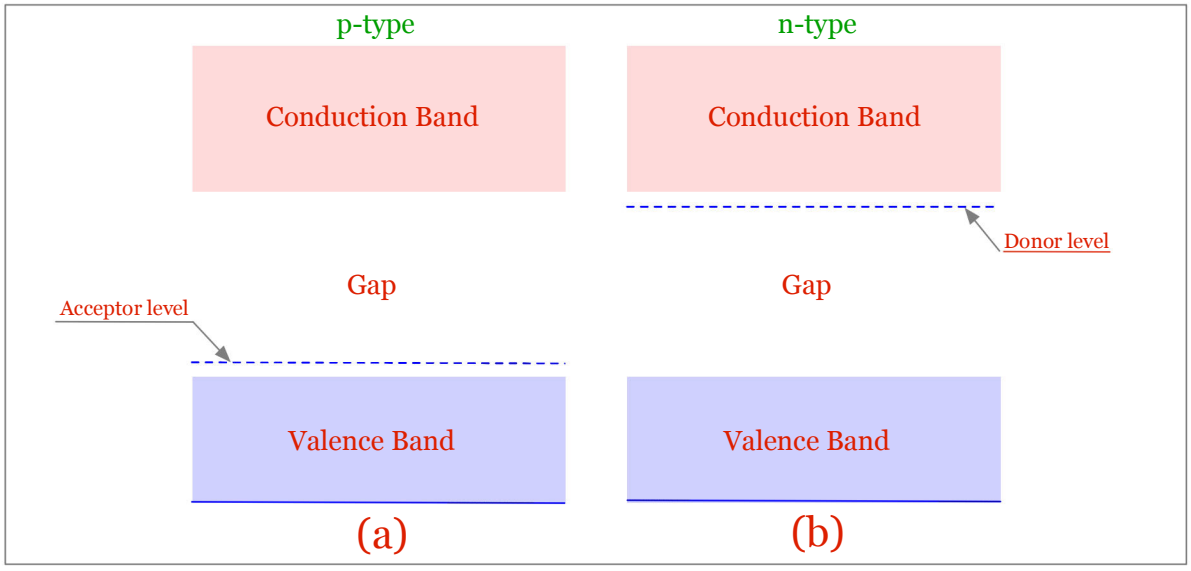

Figure 3.11: The band structure for (a) a p-type semiconductor, and (b) a n-type semiconductor is shown.

3.5.2 The Pn-Junction

A useful device can be made by combining a p-type and an n-type semiconductor[3]. Such a device is called a pn-junction and it can be used as a switch. It can also be used as a basic component for several electronic devices like transistors.

The two parts of the pn-junction are initially electrically neutral. However, some of the electrons from the n-type diffuse into the p-type across the barrier. This results in an accumulation of negative charge on the p-side and a positive charge on the n-side. This will establish an internal electric field pointing from the n-side toward the p-side within a region where electrons combine with holes. This region is called the depletion region since it contains no free

[3]The combination is not done by simply slabbing the two pieces together. It is normally done by injecting a single semiconductor crystal by a donor material into one side and the acceptor material into the opposite side.

electrons or free holes. The internal field will keep growing in strength and eventually stop the diffusion of electrons.

Now, if a battery is connected to the pn-junction with the positive terminal connected to the p-side and the negative terminal to the n-side, this will establish an electric field that is in the opposite direction of the internal field diminishing it. The battery voltage is large enough such that the holes in the p-side will be attracted to the negative terminal of the battery and the electrons in the n-side will be attracted to the positive terminal of the battery. The electrons and holes meet at the junction, where the electrons cross over and fill the holes. In the meantime, the battery takes electrons from the p-side to inject them into the n-side, which creates new holes in the p-side. A large current is established and the pn-junction is said to be *forward biased*. On the other hand, if the battery is connected to the pn-junction with the positive terminal connected to the n-side and the negative terminal to the p-side, the holes in the p-side will be attracted to the negative terminal of the battery and the electrons in the n-side will be attracted to the positive terminal of the battery. This establishes an electric field in the same direction as the internal field and ideally no current flows through the circuit. This is the case when the pn-junction is *reverse biased* [46]. Figure 3.12 shows the forward and reverse biased pn-junction case.

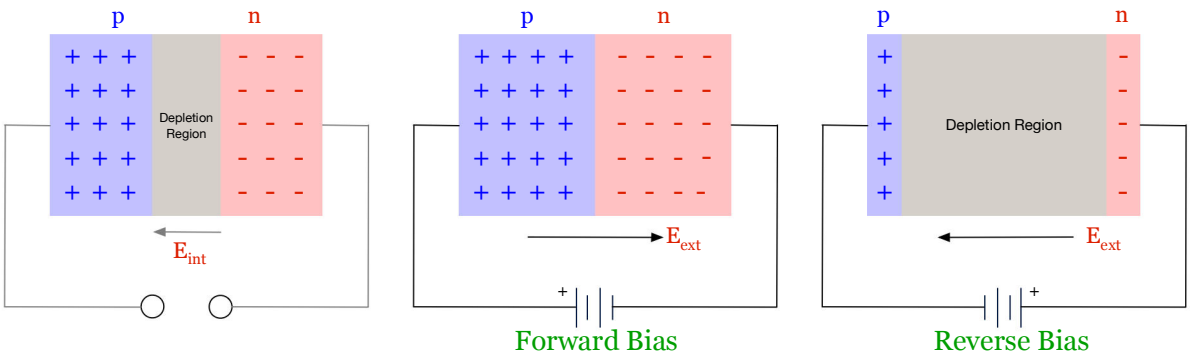

Figure 3.12: The pn-junction is shown with no bias at the left, forward biased in the middle, and reverse biased at the right.

3.5.3 The Pn-Junction as a Radiation Detector

A reverse biased pn-junction can be used as a charged particle detector. If an energetic charged particle enters the junction, it loses energy rapidly by freeing electrons to the conduction band, which creates holes in the valence band. Those charges are swept by the external field which creates a voltage drop in the form of a pulse that can be detected and counted. The collection time is quite short so the detector is fast. If the incoming particle loses all of its energy in the depleted region, then the number of ion pairs (or the amplitude of the pulse) is proportional to its energy. The energy required to create an ion pair in a silicon pn-junction detector is 3.6 eV, compared to 20 eV - 40 eV in gas-filled detectors [46]. As a result, the number of ion pairs per unit energy is quite large, the statistical variations are quite low, and the energy resolution is high.

A reverse biased pn-junction can then be a fast and high energy resolution charged particle detector. In addition, it also offers a high efficiency for a wide range of charged particles. This

detector can be a position sensitive device as well. It is possible to segment one side of the pn-junction into vertical strips and the other side into horizontal strips. That is exactly the description of the DSSSD detector which is used as an end detector in the DRAGON facility.

The DSSSD is a 5 cm $\times$ 5 cm silicon based detector that has 16 front strips and 16 back strips. The two sets of strips are oriented orthogonally to each other. The strips are 3 mm wide, approximately 5 cm long, and 250 μm thick. The space between the strips is about 100 μm wide. When a charged particle enters the detector, it creates a number of electron-hole pairs and they will be swept away by the detector bias to create two coincident signals, which come from the front and from the back. This way, the detector behaves like an array of 256 detectors with an area of 3 mm^2 each. The signals from the front and the back are picked up by the detector electronics, and the corresponding strips identify the x-coordinates and the y-coordinates of the particle [46, 47].

The energy resolution of the detector was determined to be around 1% and the position resolution is 3 mm [46]. Given these properties, the detector can usually separate the recoils from any remaining beam. However, this may not be the case for certain energies and masses of the beam and recoils. In such cases, a further reduction can be achieved by taking data in coincidence mode between the gamma array and the end detector. Coincidence mode requires the gamma ray events to be associated with recoil events at the end detector to be acceptable events.

Figure 3.13 illustrates the DSSSD geometry with its aluminium electrodes [43]. The n-side is the n-type semiconductor and the p-side is the p-type semiconductor. The symbol n^+ indicates high density donor doping and likewise, p^+ indicates high density acceptor doping. A thin layer of SiO_2 is placed on both sides of the DSSSD to protect it from contamination [46].

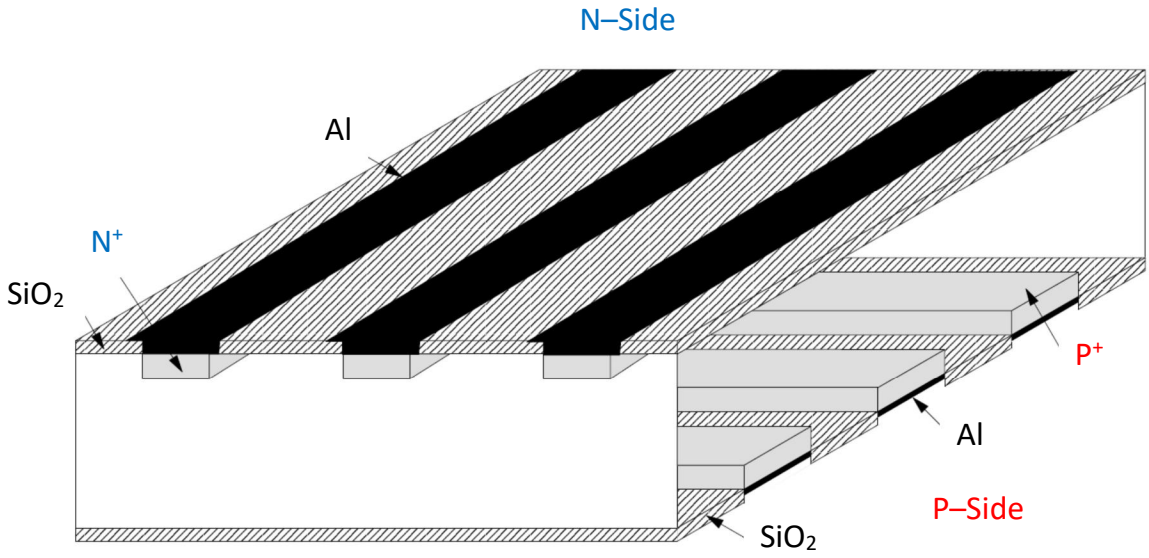

Figure 3.13: The Double Sided Silicon Strip Detector is shown with its n-side and p-side.

3.6 Summary

To summarize, Figure 3.14 shows a three-dimensional view of DRAGON [43].

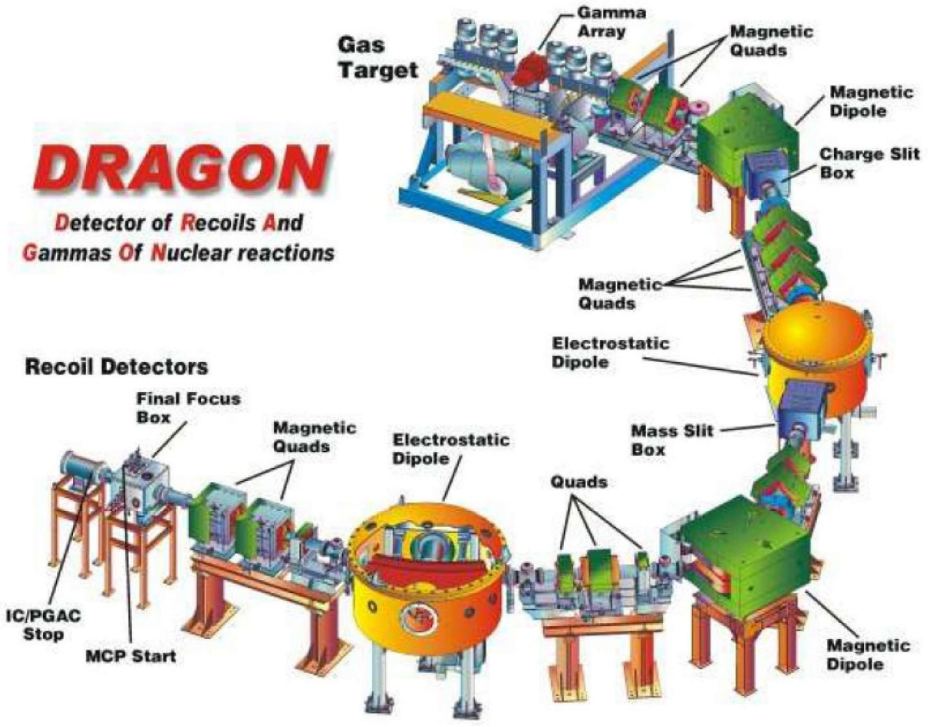

Figure 3.14: The three-dimensional illustration for DRAGON is shown. This diagram has not been drawn to scale.

Chapter 4

Detector Measurements

This thesis focuses on simulations and experiments that have been performed on an individual $LaBr_3$:Ce detector which has been doped by a 5% mole fraction of Ce. The purpose is to illustrate its energy resolution advantage over the BGO detector while showing its gamma ray capture efficiency disadvantage.

To accomplish this, the simulations are performed by Geant4 (Geometry and Tracking 4), which has been written in the programming language of C++ [44]. This program provides the foundation for the detector simulations in which the gamma ray capture efficiency of a single BGO and $LaBr_3$:Ce detector can be estimated.

Ideally, the simulation results should agree with the experimental results for a given detector configuration to show the accuracy of the simulation. For instance, the gamma ray capture

efficiency of the $LaBr_3$:Ce detector simulation should agree with the results of its experimental counterpart, within error. The simulation methodology is discussed in terms of how the detectors are modelled and set up to detect gamma rays. The single detector simulation results are summarized, along with the main causes of the simulation errors.

The efficiency measurements were experimentally performed for a single $LaBr_3$:Ce detector that was borrowed from the Gamma-Ray Infrastructure For Fundamental Investigations of Nuclei (GRIFFIN), and their results are compared to the simulations. In addition, the experimental $LaBr_3$:Ce detector energy resolution is measured.

4.1 Simulation Methodology

For this simulation, the detector is the mother volume that is used to house its daughter volume components. These daughter volumes are not considered to be overlapping with the mother volume, since they are parts of the mother volume. The simulation is confined to the world volume, which is a cube with a side length of 1 m. Further details on how Geant4 handles objects and the physics of particle interactions are found in this comprehensive paper by Agostinelli *et al.* and the Physics Reference Manual [44, 48]. Appendix C shows how to access the Geant4 code where the detectors and materials are defined as well as how the gamma ray interaction data are placed into histograms.

4.1.1 Single Detector Configuration

Every volume is composed of a material, and the parameters of each material have been defined to represent realistic experimental conditions [44]. Specifically, all simulations are performed at a pressure of 1 atmosphere and a temperature of 298.15 K. Table 4.1 lists the characteristic gamma ray energies for each radioactive source that was used for data collection [3, 12, 49, 50]. For the simulations, all gamma ray sources were point sources that emit gamma rays isotropically, and their activities have no uncertainties [44]. The data tables which summarize the $LaBr_3$:Ce detector dimensions, geometry, and materials are on Table A1 and Table A2 in Appendix A. Likewise, the details of the BGO detector are given on Table A3 and Table A4 in Appendix A.

Table 4.1: The external radioactive sources and their gamma ray energies.

Source	Energy
^{137}Cs	0.6617 MeV
^{60}Co	1.17 MeV, 1.33 MeV
^{22}Na	1.27 MeV, 2×0.511 MeV
$^{241}Am^{9}Be$	4.44 MeV
$^{244}Cm^{13}C$	6.131 MeV

For the internal radiation source ^{138}La of the single $LaBr_3$:Ce detector with a half-life of 1.03×10^{11} years, the gamma ray emission rate is calculated to be about 53 per second for 0.789 MeV, and about 100 per second for 1.436 MeV at the present day. The branching ratios for the 0.789 MeV and 1.436 MeV gamma rays are 0.345 and 0.655, respectively [12]. All external sources were set at an intensity of 1.0 for the simulations. The laboratory experiments and simulations were performed with the external source placed along the central z-axis of a single cylindrical $LaBr_3$:Ce detector at distances of 5, 10, and 20 cm away from it. These positions are called 1, 2, and 3, respectively. Figure 4.1 illustrates this arrangement for position 1 [44]. The energy axis is divided into 1,000 channels between 0 MeV and 10 MeV. For positions 1, 2, and 3, the sources isotropically emitted 300,000 gamma rays. The source intensity is assumed to be proportional to the total number of gamma rays emitted. In this case, an intensity of 1.0 corresponds to 300,000 gamma rays being emitted per simulation. Since ^{22}Na and ^{60}Co were treated as two sources in the simulations, it is assumed that 150,000 gamma rays are emitted from each source on average. This is a reasonable assumption since the sources have equal intensities in the simulations. In regards to ^{60}Co, the 1.17 MeV and 1.33 MeV gamma rays have equal branching ratios so they are treated as having equal intensities [49]. 5 trials were performed for each source and position by using the Geant4 random number seeds. The simulations excluded the internal radiation of the $LaBr_3$:Ce detector, since they are being compared to the experimental spectra after their internal radiation entries have been removed. The photopeak efficiency ε_{sim} is calculated by taking the number of gamma rays

captured by the detector N with an energy value in the photopeak as a percentage of the total number of gamma rays emitted by the source T, as shown in Equation 4.1.

$$\varepsilon_{sim} = \frac{N}{T} \times 100\% \tag{4.1}$$

The data set has 5 points to represent 5 trials since the simulations involve random processes, in which the mean is taken for each source and position. The sample standard deviation is taken to calculate the mean standard error.

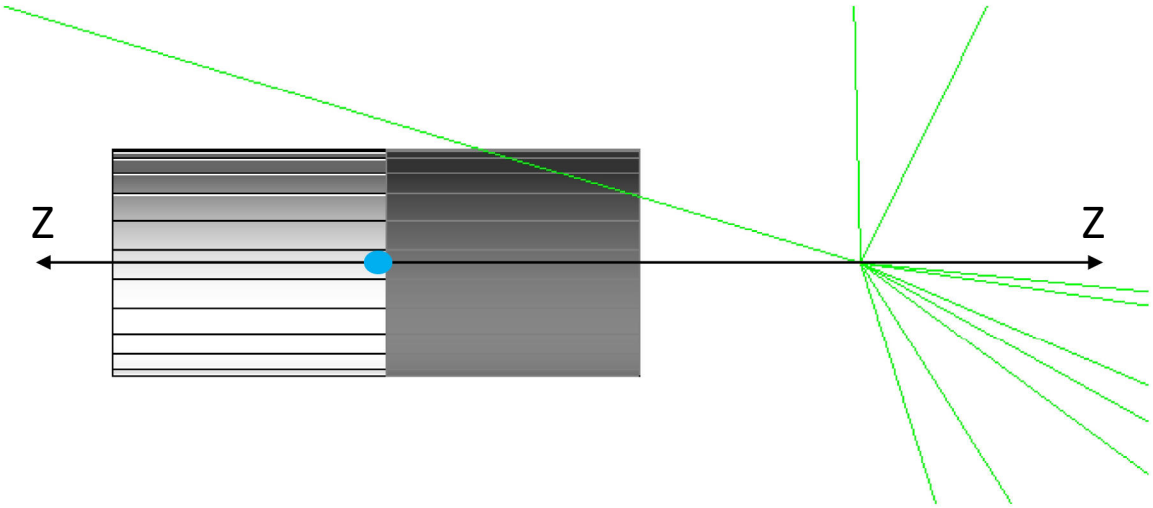

Figure 4.1: The simulation arrangement is shown where the source emits 10 gamma rays at a distance 5 cm away from the detector face. The blue oval represents the origin where $z = 0$. This diagram has been approximately drawn to scale.

4.2 Single $LaBr_3$:Ce Detector Simulation Results

The simulation results for ^{22}Na, ^{60}Co, and ^{137}Cs have been obtained, and their respective position 1 sample spectra are shown in Figure 4.2, 4.3, and 4.4. These 3 sources form the main focus of this thesis. Data on ^{241}Am^{9}Be and ^{244}Cm^{13}C are included for the purpose of comparison to previously obtained detector efficiency results to inspire confidence in the results of this thesis. The spectra have the "Entries" plotted on the vertical axis with respect to "Energy (MeV)" on the horizontal axis. The total number of entries in each spectrum is included.

4.2.1 ^{22}Na

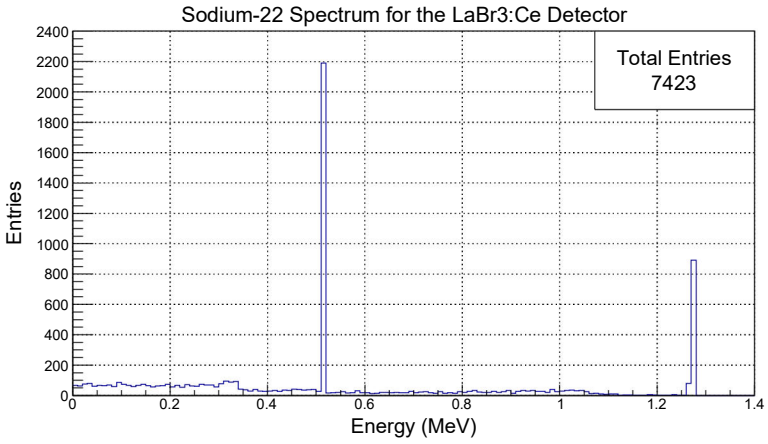

Figure 4.2: The simulated Sodium-22 spectrum is shown.

4.2.2 ^{60}Co

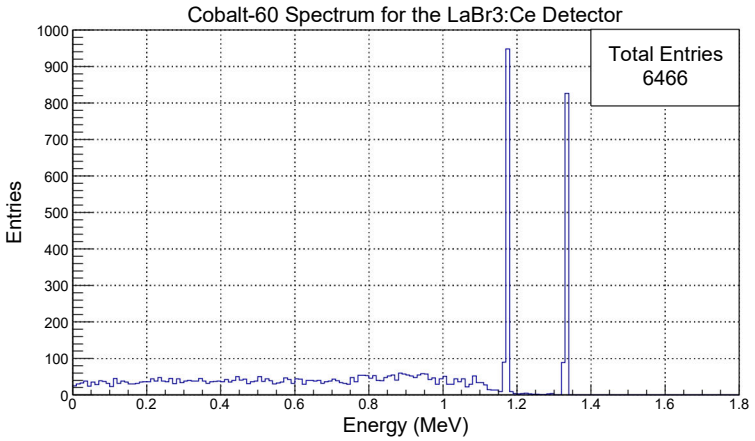

Figure 4.3: The simulated Cobalt-60 spectrum is shown.

4.2.3 ^{137}Cs

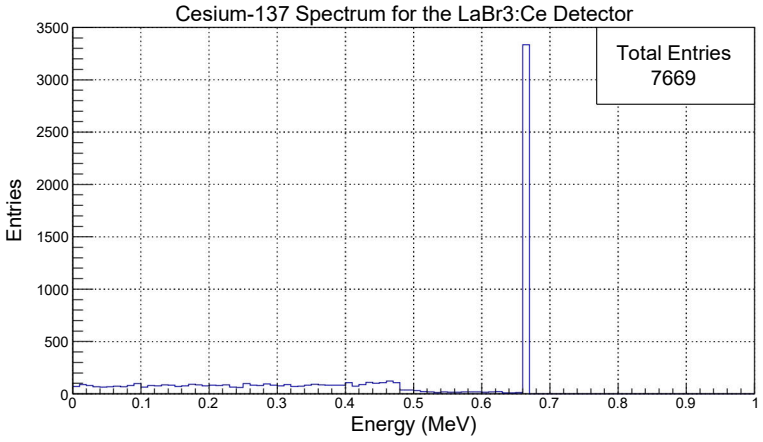

Figure 4.4: The simulated Cesium-137 spectrum is shown.

4.2.4 $^{241}Am^{9}Be$

Figure 4.5 shows a simulated spectrum obtained for the $^{241}Am^{9}Be$ source at position 1.

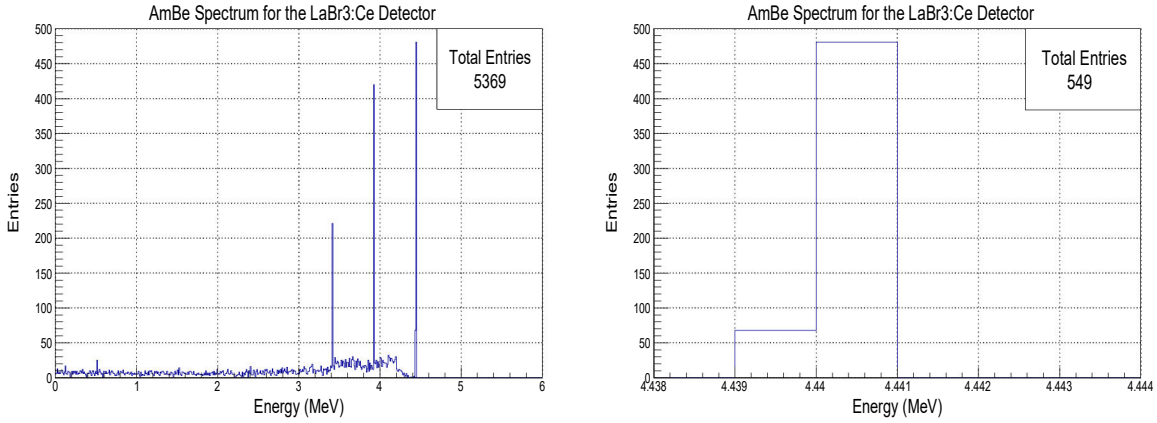

(a) (b)

Figure 4.5: (a) The simulated Americium-Beryllium (AmBe) spectrum is shown, where a single escape peak and a double escape peak are evident. (b) A close-up view of the full energy peak split into two channels is shown, where the histogram has been divided into 10,000 channels. The sum of the two peak counts is used to determine the photopeak efficiency in which 549 entries are shown here.

4.2.5 $^{244}Cm^{13}C$

Figure 4.6 shows a simulated spectrum obtained for the $^{244}Cm^{13}C$ source at position 1.

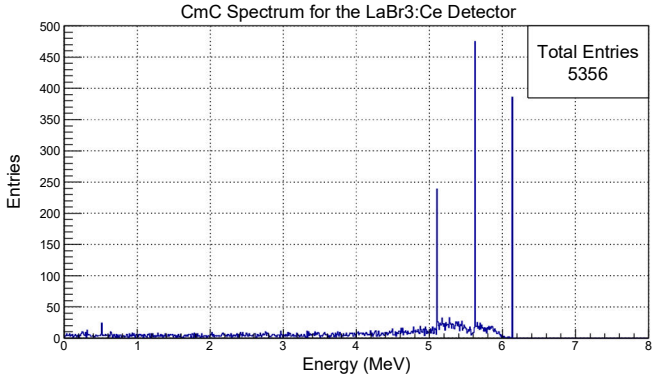

Figure 4.6: The simulated Curium-Carbon (CmC) spectrum is shown, where a single escape peak and a double escape peak form.

4.2.6 Simulated BGO and $LaBr_3$:Ce Efficiency Comparison

The main difference between $^{241}Am^{9}Be$ and $^{244}Cm^{13}C$ and the lower energy sources is that single escape events and double escape events occur. This explains why there are two peaks; one about 0.511 MeV below and one about 1.022 MeV below the full energy peak in their spectra.

Table 4.2 summarizes the BGO detector and the $LaBr_3$:Ce detector efficiency values which have been rounded to 3 decimal places. Figure 4.7, Figure 4.8, and Figure 4.9 plot the given values in Table 4.2 to illustrate the loss in gamma ray capture efficiency when the BGO detector is exchanged for the $LaBr_3$:Ce detector. The distance at which the data points were taken

is specified. The plots that are displayed in this thesis are generated by Gnuplot [51].

Regarding the error bars, precision increases with the amount of statistics in which the sizes of the error bars relative to the data points decreases. The BGO data have higher precision than the $LaBr_3$:Ce data because the photopeaks have more entries. As the number of entries decreases for higher gamma ray energies due to the reduced likelihood of complete energy loss within the detector, the precision worsens as expected.

Table 4.2: The simulated efficiency values for the BGO detector and the $LaBr_3$:Ce detector.

Energy (MeV)	Position	BGO Efficiency (%)	$LaBr_3$:Ce Efficiency (%)
0.511	1	3.783±0.012	1.415±0.015
0.511	2	1.300±0.018	0.496±0.010
0.511	3	0.363±0.009	0.152±0.006
0.6617	1	3.384±0.011	1.113±0.007
0.6617	2	1.187±0.009	0.403±0.007
0.6617	3	0.356±0.001	0.117±0.002
1.17	1	2.495±0.018	0.642±0.011
1.17	2	0.895±0.009	0.224±0.005
1.17	3	0.273±0.009	0.064±0.002
1.27	1	2.329±0.021	0.582±0.007
1.27	2	0.852±0.008	0.209±0.010
1.27	3	0.270±0.003	0.064±0.004
1.33	1	2.245±0.031	0.544±0.007
1.33	2	0.840±0.009	0.200±0.003
1.33	3	0.253±0.004	0.062±0.002
4.44	1	1.225±0.013	0.184±0.002
4.44	2	0.455±0.003	0.067±0.002
4.44	3	0.149±0.004	0.024±0.001
6.131	1	1.059±0.010	0.125±0.002
6.131	2	0.403±0.005	0.049±0.001
6.131	3	0.128±0.002	0.015±0.002

The error bars are relatively small on the order of 10^{-2} and 10^{-3}, which is why they are not clearly visible. In addition to the source-to-detector distance, the detector efficiency also depends on the size and shape of the scintillator crystal so the scintillators that have similar dimensions are the ones being compared to each other.

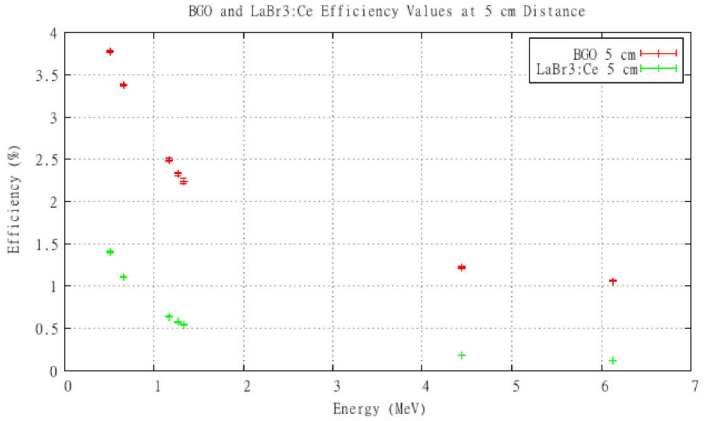

Figure 4.7: The simulated BGO and $LaBr_3$:Ce detector efficiency values are compared at a source-to-detector distance of 5 cm.

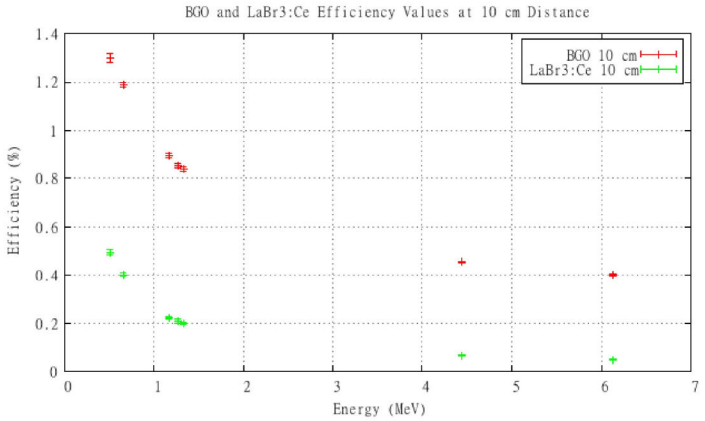

Figure 4.8: The simulated BGO and $LaBr_3$:Ce detector efficiency values are compared at a source-to-detector distance of 10 cm.

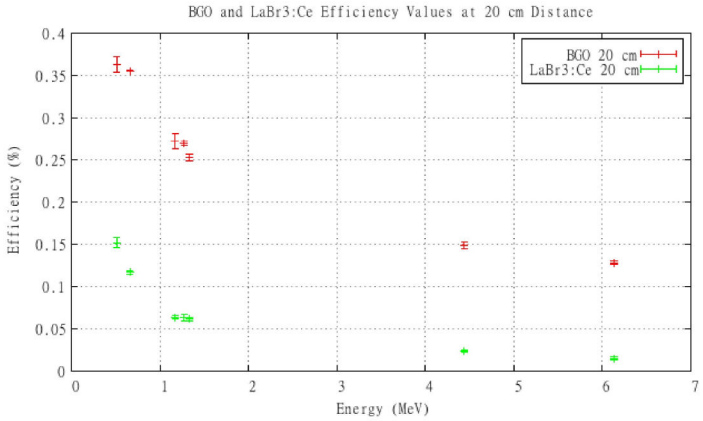

Figure 4.9: The simulated BGO and $LaBr_3$:Ce detector efficiency values are compared at a source-to-detector distance of 20 cm.

4.3 Other Simulation Errors

There are other sources of error aside from the mean standard error that have not been quantified. In regards to systematic error, the photomultiplier tube window and photomultiplier tube may not actually be made of pyrex glass, but the error is considered to be negligible since the main focus of the simulations is the scintillator crystal response to gamma rays. The main difference between the simulations and experiments is that the simulations register gamma rays that have deposited their energies into the scintillator crystal as histogram entries. The experiments register gamma ray events that have been represented by electrons that reach the end of the photomultiplier tube. Not all gamma ray events that have been captured within the scintillator would receive a complete representation, since not all of their photons would reach the photocathode and release photoelectrons. In terms of random error, the detectors may differ slightly from the ideal cylindrical or hexagonal shape in reality. Furthermore, ^{60}Co

does not act as an isotropic source since it decays in 2 steps, even though the simulation treats it as two isotropic point sources for 1.17 MeV and 1.33 MeV [52]. The only input parameter that is varied in the simulations is the distance away from the point source, with all of the other parameters such as the properties of the detector being held constant. Geant4 simulates real world physics to the best of its ability, but errors still occur to provide the values of $\bar{\sigma}$.

4.4 Experimental $LaBr_3$:Ce Detector Configuration

Figure 4.10 outlines the electronic circuit that is used to acquire data from a $LaBr_3$:Ce detector. The electronics are powered by the LeCroy Model 1403 and the detectors are powered by the LeCroy Model HV4032A at 1,260 V, where HV stands for high voltage. The pre-amplifier output is a charge signal that is split into two parts. One part goes directly to a 16 channel charge integrating VME (Versa Module Europa bus) ADC, and the other part is used to generate a gate. The CAEN (Costruzioni Apparecchiature Elettroniche Nucleari) Model V785N is used as the ADC (Analogue-to-Digital Converter), and its specifications are given here [53]. Each detector signal is sent to one of the ADC channels. The Phillips Scientific Model 794 is used as the GDG (Gate and Delay Generator) and the LeCroy Model 821Z is used as the discriminator, which is used to reject as much noise as possible while allowing the signals to go through. Their specifications are given here, respectively [54, 55]. The Joerger Visual Scaler Model VS 11214 is used as the gamma ray event and gate counter. The gate is delayed by

56 ns using a BOO7 Delay Line so that they coincide with their respective signal. The VME mini crate used in the system has three modules; the peak sensing ADC, the charge integrating ADC, and the TDC (Time to Digital Converter). This gate is then used to operate the ADC. The data are acquired from the detector and processed by MIDAS (Maximum Integrated Data Acquisition System), which takes full control of the VME mini crate to acquire and store the data from the VME modules. MIDAS then histograms the data and displays the histograms on the computer screen.

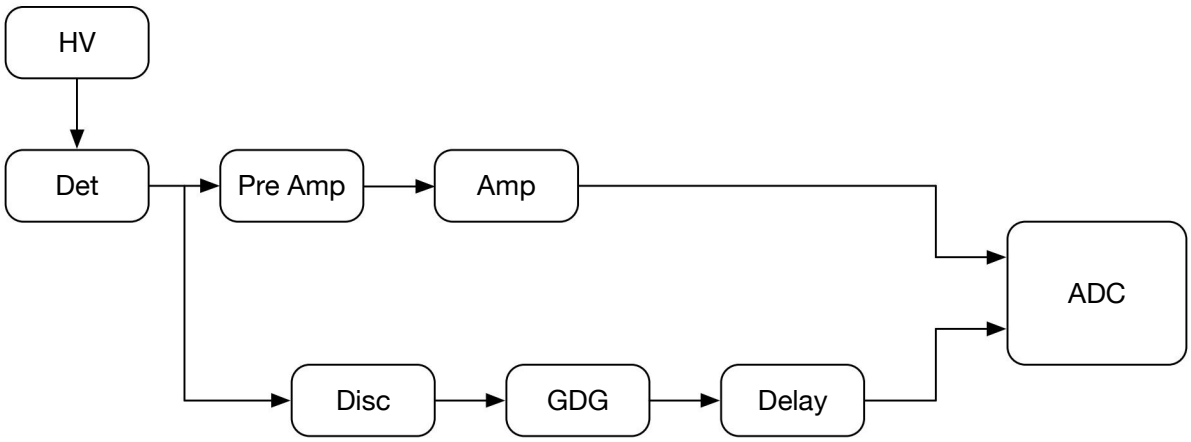

Figure 4.10: The circuit diagram for the $LaBr_3$:Ce detector is shown. The signals from the detector are paired with gates so they can be accepted by the ADC.

4.4.1 Experimental $LaBr_3$:Ce Efficiency Analysis

The efficiency of the $LaBr_3$:Ce detector is measured by using a Gaussian fitting function, which is able to model the photopeaks as Gaussian distributions. The Gaussian distribution is used because the peaks contain a large number of counts so they resemble normal distributions

that are symmetric around the mean [7]. Before the analysis is performed, all of the spectra had the internal radiation of $LaBr_3$:Ce subtracted from them. This was done by comparing the run time of an experimental run that solely measures the internal radiation to the run time of a given spectrum. For example, position 1 of ^{22}Na has a run time of 1,590 seconds and the internal radiation run has a run time of 146,778 seconds. The run time of ^{22}Na at position 1 is divided by the internal radiation run time to yield about 0.011. The counts in each channel of position 1 ^{22}Na spectrum is added to -0.011 times of the counts of each corresponding channel in the internal radiation run to perform the subtraction. During the Gaussian fit process, the background which applies to any spectrum is fitted with a cubic function to approximate its shape. This function is used to subtract the background below the photopeak. The analysis is performed by reporting the central position of the data and the Gaussian fit, as well as their width, height, and area. The fitted background is reported as well as χ^2 as a measure of its goodness of fit. A χ^2 value near 1 indicates an excellent fit, while smaller values indicate inaccurate fits.

The value of the Gaussian peak area is denoted P, which is the number of decays that correspond to captured full gamma ray energy events. P estimates the efficiency ε_{exp} in Equation 4.2,

$$\varepsilon_{exp} = \frac{P}{Atb} \times 100\% \tag{4.2}$$

where A is the source activity in Bq, t is the experimental run time in seconds, and b is the branching ratio of the radioactive decay source in question [56]. As seen in Equation 4.2,

ε_{exp} is dimensionless like ε_{sim}. The branching ratios and the half-lives of the decay sources are given in Table 4.3, and the details of A and t are given on Table A9 and Table A10 in Appendix A. A brief guide on how to use this program is given in Appendix B. The half-lives were taken into account to calculate the source activities on April 1, 2018, which is the estimated date of the $LaBr_3$:Ce detector efficiency measurements. These values of A were used to calculate the values of ε_{exp} [12, 49, 57]. There are three main sources of error; the uncertainties of the

Table 4.3: The half-lives and branching ratios of the radioactive sources.

Source	Half-Life (years)	Branching Ratio(s)
^{22}Na	2.6018	1.8 (0.511 MeV), 1.0 (1.27 MeV)
^{60}Co	5.2712	1.0 (1.17 MeV, 1.33 MeV)
^{137}Cs	30.08	0.851
^{241}Am^{9}Be	432.6	1.0
^{244}Cm^{13}C	18.11	1.0

source activities ΔA which are provided as percentages of the source activity A to be taken as $\frac{\Delta A}{A}$, the statistical variation in the area under the full energy peak ΔP which is taken as $\frac{\Delta P}{P}$, and the uncertainty of the distance measurements Δd which is ± 0.05 cm to be taken as $\frac{\Delta d}{d}$. Since background subtraction is being performed, the peak area P includes the background counts B to determine its uncertainty so $\frac{\Delta P}{P}$ is given by $\frac{1}{\sqrt{P+B}}$ [1]. The uncertainties are taken as relative errors, and they are added in quadrature to obtain $\Delta\varepsilon_{exp}$ in Equation 4.3 [3].

$$\frac{\Delta\varepsilon_{exp}}{\varepsilon_{exp}} = \sqrt{\left(\frac{\Delta A}{A}\right)^2 + \left(\frac{\Delta P}{P}\right)^2 + \left(\frac{\Delta d}{d}\right)^2} \tag{4.3}$$

Sample spectra around each individual photopeak on position 1 for the sources ^{22}Na, ^{60}Co, and ^{137}Cs are shown along with their respective Gaussian fit analyses in Figure 4.11, 4.12,

4.13, 4.14, and 4.15. The parameters that are shown in the Data column represent the data themselves where the program did the calculations on the spectra formed by the data points, while the parameters that are shown in the Gauss column represent the parameters of the fitted Gaussian function. The area in the Gauss column is taken as the Gaussian peak area. The "Counts/Channel" label on the *y*-axis refers to the number of counts in each of the individual channels.

4.4.2 ^{22}Na

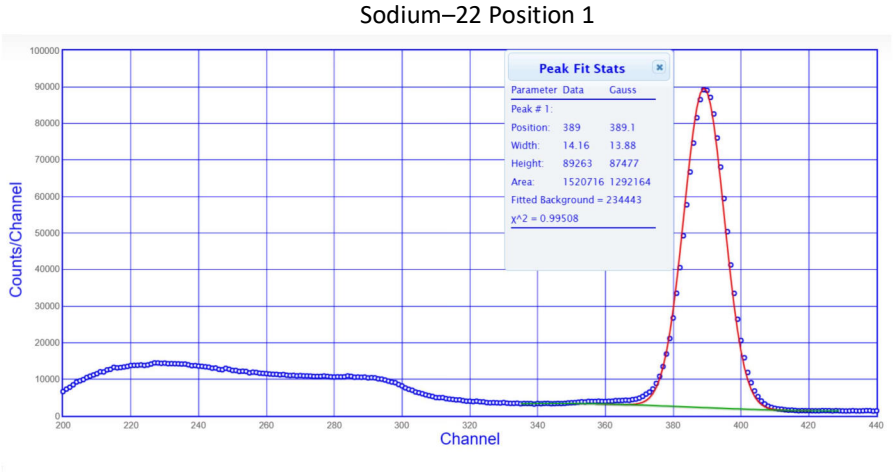

Figure 4.11: The experimental 0.511 MeV spectrum is shown. The Compton scattering counts form a small plateau over the background to the left of this photopeak.

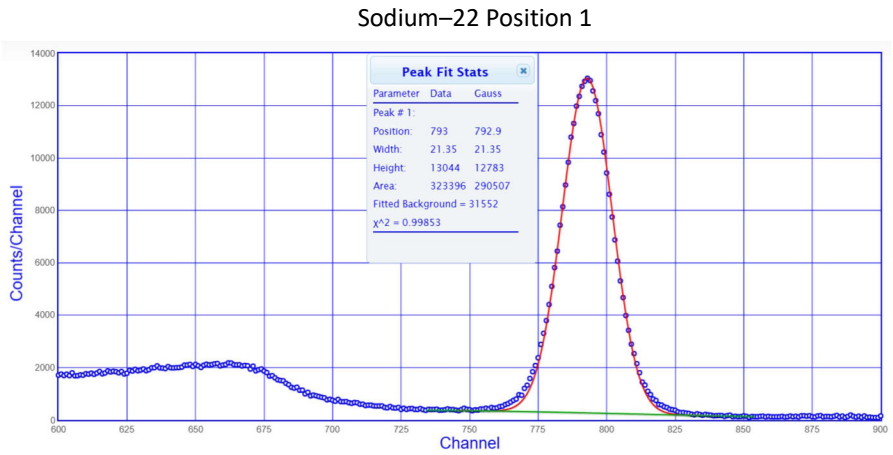

Figure 4.12: The experimental 1.27 MeV spectrum is shown. The Compton scattering counts form a small plateau over the background to the left of this photopeak.

4.4.3 ^{60}Co

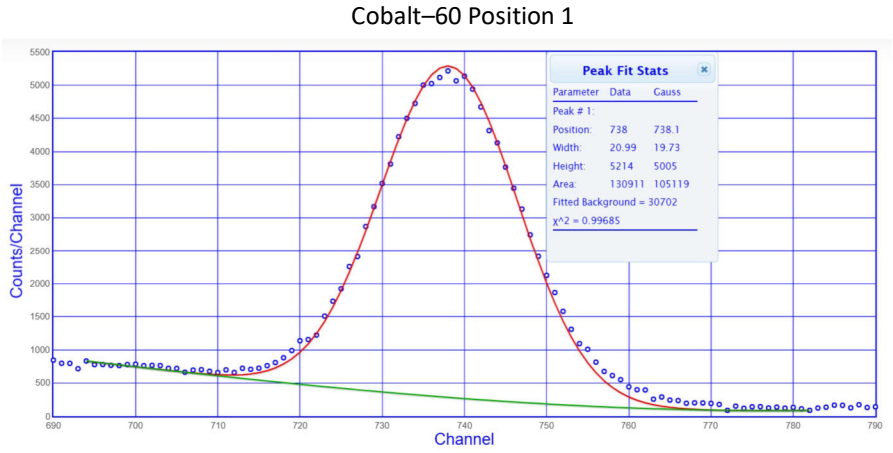

Figure 4.13: The experimental 1.17 MeV spectrum is shown.

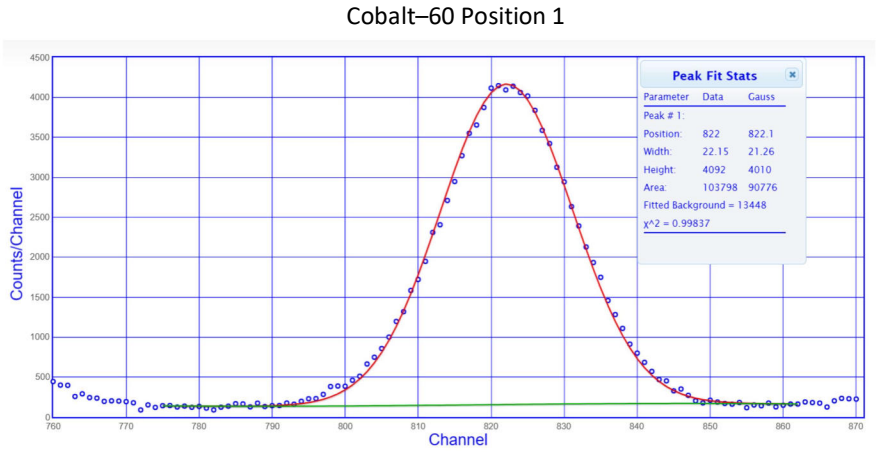

Figure 4.14: The experimental 1.33 MeV spectrum is shown.

4.4.4 ^{137}Cs

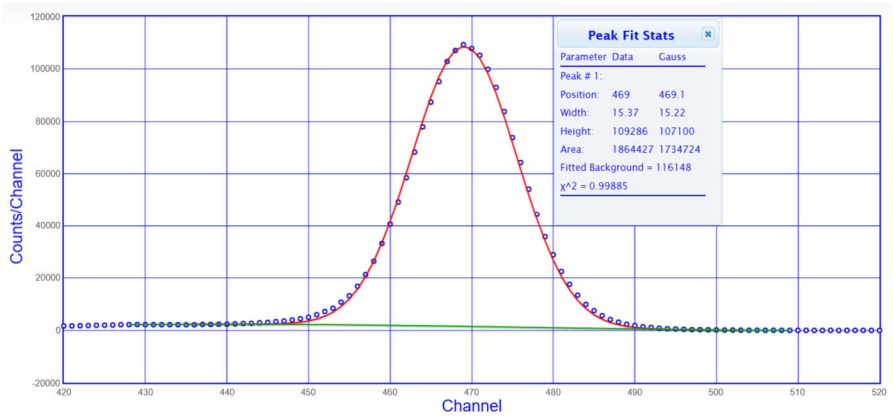

Figure 4.15: The experimental 0.6617 MeV spectrum is shown.

4.4.5 Experimental $LaBr_3$:Ce Efficiency Data Summary

Table 4.4 summarizes the experimental efficiency data which have been rounded to 3 decimal places. The uncertainties are mainly dominated by the source activity uncertainties, so there is no correlation between the precision and the incident gamma ray energy.

Table 4.4: The measured efficiency values for the $LaBr_3$:Ce detector.

Energy (MeV)	Position	$LaBr_3$:Ce Efficiency (%)
0.511	1	1.396±0.044
0.511	2	0.490±0.015
0.511	3	0.148±0.004
0.6617	1	1.102±0.042
0.6617	2	0.396±0.015
0.6617	3	0.119±0.004
1.17	1	0.632±0.014
1.17	2	0.222±0.004
1.17	3	0.064±0.001
1.27	1	0.565±0.018
1.27	2	0.208±0.006
1.27	3	0.063±0.002
1.33	1	0.546±0.012
1.33	2	0.204±0.004
1.33	3	0.061±0.001

4.5 Experimental $LaBr_3$:Ce Energy Resolution

The purpose of comparing the experimental energy resolution values to the literature is to confirm the validity of the results. To estimate the energy resolution of the experimental spectra, the Gaussian fit is performed on the given photopeak for the 3 different positions to estimate how the Gaussian fit width varies in which the mean width is taken. The Gaussian fit may underestimate the width of the data, which is clearly shown on Figure 4.13 and 4.14. The error is calculated in the same way as for the simulated efficiency data, which is by taking the sample standard deviation and then the mean standard error. The dimensionless energy resolution R is estimated as a percent of the photopeak energy E by using Equation 4.4,

$$R = \frac{FWHM}{E} \times 100\% \tag{4.4}$$

where $FWHM$ represents the Full Width Half Maximum [56]. The $FWHM$ is given by the Gaussian fitting program as a channel width when the Gaussian fit is performed, and the channel of the peak corresponds to E. Table 4.5 summarizes the experimental energy resolution data which have been rounded to 3 decimal places. In comparison to the literature, the energy resolution of the $LaBr_3$:Ce detector is measured to be about 2.6% at room temperature in response to 0.6617 MeV gamma rays. This study estimates the energy resolution values to decrease to about 2% as the incident gamma ray energy reaches 1.33 MeV [58]. In terms of a physical explanation for this improvement in energy resolution, the number of photons yielded by a scintillator in response to a gamma ray may fluctuate, and these fluctuations represent a

smaller percentage of larger gamma ray energies since their corresponding photon populations are higher.

It is important to note here that the energy resolution of a detector depends on how it has been manufactured. Therefore, there is no universal value for the energy resolution of a given compound or element but there is a realistic range of values. For instance, another study found the energy resolution of the $LaBr_3$:Ce detector to be around 3.2% for 0.662 MeV gamma rays, which is close to the estimated value in Table 4.5 [34]. Overall, the general trend of the data agrees with the literature; the energy resolution improves as the incident gamma ray energy increases [31, 58].

Table 4.5: The measured energy resolution values for the $LaBr_3$:Ce detector.

Energy (MeV)	$LaBr_3$:Ce Energy Resolution (%)
0.511	3.535±0.019
0.6617	3.282±0.021
1.17	2.647±0.021
1.27	2.721±0.018
1.33	2.661±0.039

4.6 Experimental and Simulated Data Comparison

Figure 4.16, Figure 4.17, and Figure 4.19 illustrate the comparisons between the experimental and the simulated efficiency results for the $LaBr_3$:Ce detector. Figure 4.18 compares the simulated efficiency data for the BGO detector to the experimental efficiency data acquired

by Gigliotti [3]. All data points agree within error, which further confirms the validity of the results. However, the differences between the simulation and experimental data are between 1% to 3% of the experimental values in most cases. In these cases, the simulations seem to systematically overestimate the efficiency. Some of the error bars are very small on the order of 10^{-2} and 10^{-3}, which is why they are not clearly visible. However, these error bars are about on the same order of magnitude as the differences between the data. Therefore, it is not clear if the differences between the simulation and experimental data are actually obscured by the error bars, so more precise measurements may be needed to confirm data agreement.

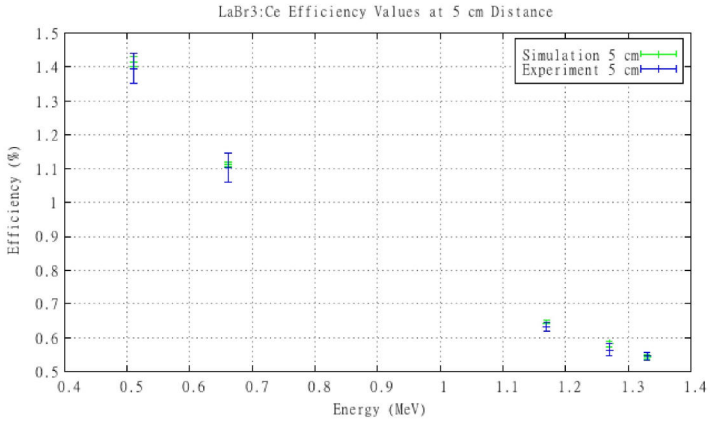

Figure 4.16: The experimental and simulated efficiency values for the $LaBr_3$:Ce detector are compared at a source-to-detector distance of 5 cm.

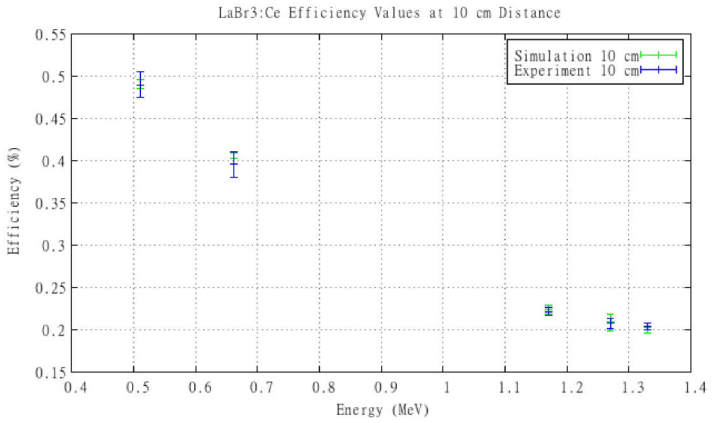

Figure 4.17: The experimental and simulated efficiency values for the $LaBr_3$:Ce detector are compared at a source-to-detector distance of 10 cm.

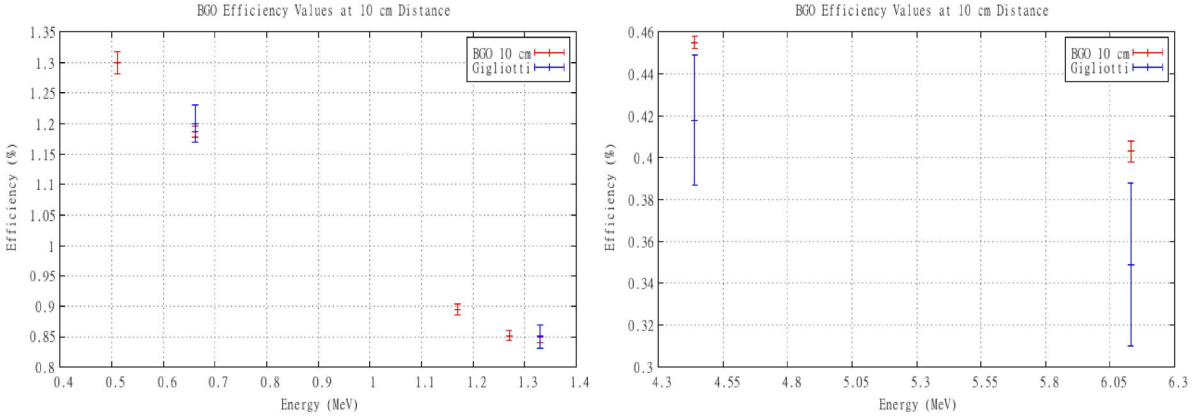

(a) (b)

Figure 4.18: (a) The simulated BGO detector efficiency values are compared to previously obtained experimental values at a source-to-detector distance of 10 cm for the ^{60}Co and ^{137}Cs sources. (b) The simulated BGO detector efficiency values are compared to previously obtained experimental values at a source-to-detector distance of 10 cm for the ^{241}Am^{9}Be and ^{244}Cm^{13}C sources.

It is notable that for Figure 4.18, 0.662 MeV is used instead of 0.6617 MeV, and 6.13 MeV is used instead of 6.131 MeV since these energies were rounded. The Geant4 simulation values agree with the BGO experimental values for the 0.6617 MeV ^{137}Cs source and the 1.33 MeV ^{60}Co source, but they disagree for the 4.44 MeV ^{241}Am^{9}Be source and the 6.131 MeV ^{244}Cm^{13}C source. This suggests that the simulation can accurately measure the detector efficiency at low energies, and it would overestimate the detector efficiency at higher energies.

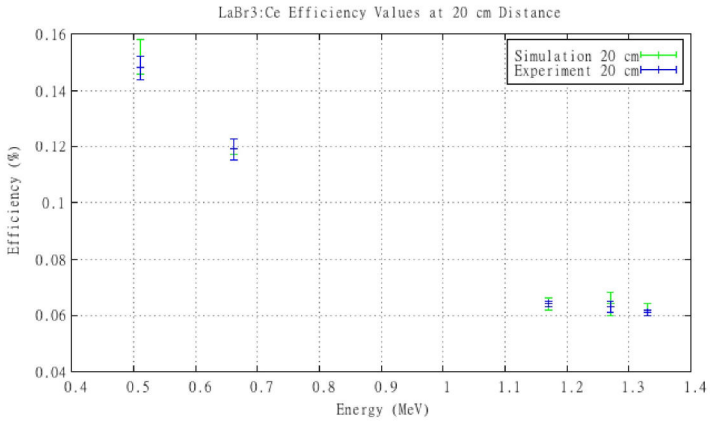

Figure 4.19: The experimental and simulated efficiency values for the $LaBr_3$:Ce detector are compared at a source-to-detector distance of 20 cm.

4.7 Other Experimental Errors

Not all of the experimental errors were quantified, since they are considered to be negligibly small compared to the main sources of error. The scintillator crystal may contain a small proportion of unknown impurities, which may affect the observed detector efficiency values and the observed energy resolution values. As previously mentioned, ^{60}Co decays in 2 steps but it is treated as an isotropic source for the experimental efficiency calculations [52]. Furthermore, the dead time of the MIDAS acquisition system was not taken into account so the system was assumed to be collecting data for the entire run time. Random errors mainly come from the background radiation which was simplistically modelled. Since the data agree within error, these other sources of experimental error appear to be negligible even though the simulations and experiments record the incident gamma rays differently.

Chapter 5

The Timing Method

In addition to the $LaBr_3$:Ce detector measurements, this thesis also focuses on how the $LaBr_3$:Ce detectors are used to more accurately determine the resonance energies of radiative capture reactions. This method is known as the timing method, and it is an application of the high time resolution that the $LaBr_3$:Ce detector provides. The further details on how DRAGON is able to measure these resonance energies are described by Hutcheon *et al.* [59].

5.1 Introduction

The main idea is that a linear accelerator system provides the beam to DRAGON but it does not do that continuously; it provides the beam in discrete beam packets at 84.9 ns intervals, and it sends a signal that corresponds to each beam packet. However, the signal is not received

at the same time as a beam packet due to the delay in the electronics. In addition, the beam velocity has a small spread, and this spread becomes significant for large beam energies over 0.5 MeV per atomic mass unit, or 0.5 MeV/u. As a result, the time taken for the beam packets to reach the gas target has a significantly large uncertainty. Consequently, their positions are not clearly known when the signals are received. The two sources of error which are the time difference between the signal and the beam as well as the beam energy spread contribute to the uncertainty of the time that the signal is received. However, these signals can be used as a time reference to which the arrival time of captured gamma rays can be referenced against. Since the arrival time of a beam bunch is related to the time at which beam ions enter the gas target, and the time of a gamma ray event denotes the time at which the capture reaction took place, the difference between them is related to how far into the gas target the beam ions got before they were captured, and thus, at what energy they were captured, i.e. the "resonance energy". This method employs a single plastic rectangular Saint-Gobain BC-404 detector as shown in Figure 5.1. It is placed at a known distance of 88 cm downstream along the path of DRAGON from the gas target centre where $z = 0$. This detector has dimensions of 1 cm x 1 cm x 0.3 cm, and it sits upright on a light guide that is attached to a Hamamatsu 6427 photomultiplier tube whose specifications are given here [60]. The purpose of this detector is to intercept the beam itself to record detection events as a time reference before the actual reaction runs. The detector is expected to capture most of the beam and a few accompanying recoils with a negligibly small amount of beam ions and recoils passing through it. The time

stamp where these events most frequently occur gives the time travelled by the beam across a 88 cm distance. This quantity is required for the timing method calculations as described by Equation 5.2.

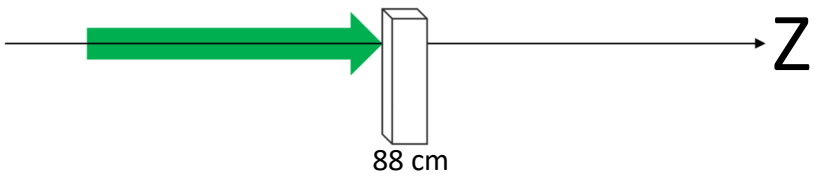

Figure 5.1: The experimental set up for the plastic detector is shown, where the detector is placed perpendicular to the z-axis. The green arrow represents the beam and recoils. This diagram has not been drawn to scale.

Figure 5.2 conceptually compares the uncertainty of the resonance energy ΔE_R and the position uncertainty ΔZ that are provided by the BGO and $LaBr_3$:Ce detectors. They are shown on an energy graph along the z-axis to show that $LaBr_3$:Ce detectors can more accurately pinpoint the resonance energy values due to their better time resolution [32]. A smaller uncertainty in time leads to a smaller uncertainty in position. The factor that ΔE_R decreases by depends on the beam energy and how the beam is tuned. In this case, beam tuning refers to the quantity of particles in a beam packet and how these beam packets travel through DRAGON during an experiment. Therefore, this improvement in the resonance energy detection process is the primary reason why the BGO detector array may be replaced by a $LaBr_3$:Ce detector array.

For a beam that is composed of a single type of radioactive particle, the nuclear capture reaction events are in many cases expected to form a Lorentzian peak around a certain resonance

energy value when the reaction frequency is graphed with respect to the reaction energy. The resonance energy value would correspond to the centroid of the Lorentzian peak, even though the beam energy distribution may be approximately Gaussian.

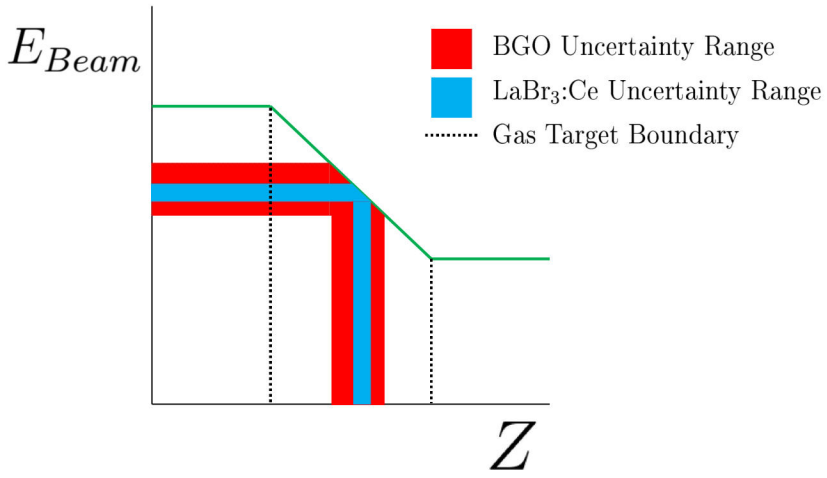

Figure 5.2: The relationship between the beam energy E_{Beam} and Z is shown along with their uncertainties as shaded regions. The uncertainties have not been drawn to scale.

5.2 Timing Methodology and Results

In addition to the plastic detector, the timing experiments were performed with 5 $LaBr_3$:Ce detectors that were borrowed from the GRIFFIN facility. These detectors have the same dimensions and components as the single $LaBr_3$:Ce detector that was used for the gamma ray capture efficiency measurement experiments. The DRAGON detector array was pulled apart to place these 5 detectors 6 cm apart in their z positions. The ends of the detectors are placed at a distance of 4.32 cm away from the beam z-axis along the x-axis. Therefore, the detector

centres are placed 10.295 cm away from the beam z-axis. These detectors are labelled 0, 1, 2, 3, and 4 and their coordinates in centimetres are (10.295, 0, -12), (10.295, 0, -6), (10.295, 0, 0), (10.295, 0, 6), and (10.295, 0, 12), respectively. Figure 5.3 illustrates this arrangement where the scintillator crystals face the gas target box [44]. The gamma rays originated from the ^{23}Na recoil when the ^{22}Ne beam underwent the ^{22}Ne(p,γ)^{23}Na reaction in the gas target. The details on the resonance energies for this reaction are described by Williams [61].

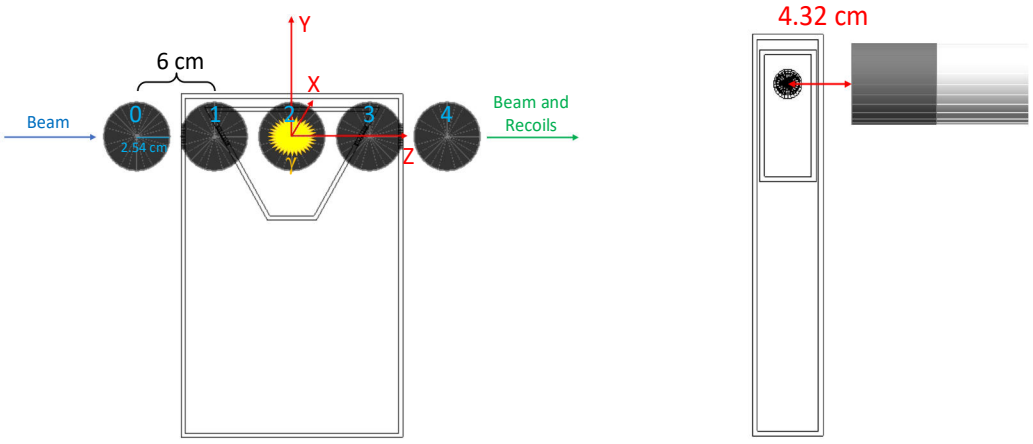

Figure 5.3: (a) The detector arrangement for the timing experiments is shown, where the detectors are behind the outline of the gas target box. The gamma rays (γ) are being released by the radiative capture reactions between the beam and the gas contained within the trapezoidal cell. (b) The side view for this arrangement is shown. These diagrams have not been drawn to scale.

Equation 5.1 calculates the gas target stopping power S for the plastic detector where L is the effective length of the gas target in centimetres and P is the gas pressure in Torr. ΔE measures the difference between the initial and the final beam energy in MeV/u after it passes through the gas target. Strictly speaking, the kinetic energy per atomic mass unit is being

presented as MeV/u. The units of S are thereby (MeV/u) / (cm Torr).

$$S = \frac{\Delta E}{LP} \tag{5.1}$$

The following calculations are performed for the plastic scintillator as shown in Equation 5.2.

$$M = MOD\left(\frac{TDC}{84.9}\right)\ [ns] \tag{5.2a}$$

$$v_{out} = 29.9\sqrt{\frac{2E_{out}}{931.494}}\ \left[\frac{cm}{ns}\right] \tag{5.2b}$$

$$t = \frac{88\ cm}{v_{out}} - M\ [ns] \tag{5.2c}$$

$$T = t + D\ [ns] \tag{5.2d}$$

The modulus M of TDC divided by 84.9 ns is taken to determine at what time was the event peak received at z = 88 cm in between the radio frequency pulses. For an example with a TDC value of -177.43 ns, the remainder between -177.43 ns and the third multiple of 84.9 ns would be 77.27 ns. This number comes from taking the third multiple of 84.9 ns which is 254.7 ns and adding -177.43 ns to 254.7 ns. This means that the beam packet which generated the event peak came 77.27 ns after the radio frequency pulse which came at a time stamp of -254.7 ns. The beam time of flight $\frac{88\ cm}{v_{out}}$, which is calculated to be about 92.759 ns, is reduced by M to determine the time at which the beam packet crossed the gas target centre at z = 0 relative to the radio frequency pulse. In this example for M being 77.27 ns, this value is subtracted from 92.759 ns to give the time stamp t of about 15.49 ns. For these experiments, v_{out} is approximately 3% of the speed of light since it depends on the final beam energy E_{out}

as shown in Equation 5.2b. The atomic mass unit is taken as 931.494 $\frac{MeV}{c^2}$, where the mass number of the beam on the numerator and the denominator have been cancelled out. The coefficient of 29.9 is set so v_{out} is given in the units of $\frac{cm}{ns}$. This t value is added by the delay time given by the electronics D to accurately estimate T. Likewise, the modulus of TDC_{LA} and 84.9 ns is taken as M_{LA}. The subscript LA denotes the values that are obtained from the $LaBr_3$:Ce detectors in which the TDC is triggered by gamma ray detection. This is done to indirectly infer the time T_{resm} and thereby the location Z_{resm} of nuclear reactions along the z-axis as shown in Equation 5.3, where the value of T is obtained from Equation 5.2d. To summarize, the difference in time between the gamma ray event and the radio frequency pulse is subtracted by the difference in time between the radio frequency pulse and when the beam packet crosses the gas target centre to determine the nuclear reaction time.

The average beam velocity over the length of the gas target is taken for v_{avg} since the beam slows down as it loses energy through the gas target. This average is calculated by using the initial and final beam energies to be used in Equation 5.3b.

$$T_{resm} = M_{LA} - T \ [ns] \tag{5.3a}$$

$$Z_{resm} = v_{avg} T_{resm} \ [cm] \tag{5.3b}$$

The calculated resonance reaction position Z_{resc} along the z-axis is given by Equation 5.4,

$$Z_{resc} = \frac{E_{in} - 0.475}{SP_r} - \frac{L}{2} \ [cm] \tag{5.4}$$

where E_{in} represents the initial beam energy, 0.475 MeV/u is the actual resonance energy value

in the lab frame, and P_r represents the pressure of a given experimental run for a $LaBr_3$:Ce detector. The literature reports this resonance as an energy value of 0.458 MeV in the centre-of-mass frame [61]. The values of Z_{resm} and L are used to determine the dimensionless value of F which is the fraction of gas that the beam crossed to reach the position Z_{resm} in Equation 5.5 and thereby E_{resm} by using Equation 5.6. E_{resm} is the measured resonance energy based on these calculations. E_{in} represents the initial beam energy, and E_{out} represents the final beam energy after it leaves the gas target.

$$F = 0.5 + \frac{Z_{resm}}{L} \tag{5.5}$$

$$E_{resm} = (1-F)E_{in} + FE_{out} \left[\frac{MeV}{u}\right] \tag{5.6}$$

4 runs were done at 4 different beam pressures; 2.3 Torr, 3.3 Torr, 4.8 Torr, and 6.2 Torr in which the centroid data were taken for each run to calculate E_{resm} for the 5 $LaBr_3$:Ce detectors. The purpose of these calculations is to compare the values of E_{resm} to each other to see if they are consistent, and also to see if they are close to a given value of E_{resc} which is the calculated resonance energy. This value is calculated by using Z_{resc} in Equation 5.5 and then by using F in Equation 5.6. The one unknown quantity is D which is being chosen such that the differences between the 4 E_{resm} values are minimized. Once D is found, the timing method can be used to estimate the unknown resonance energies in future experiments. Timing data were also taken for some BGO detectors although the centroid data cannot be taken from some of them since the peaks are not clear. This is attributed to the fact that the BGO detectors have a poor time

resolution unlike the $LaBr_3$:Ce detectors. Table 5.1 summarizes the experimental parameters for the calibration run of the timing data analysis which uses the plastic detector. Amu stands for atomic mass units, and the value of P refers to the experimental run that is done for the plastic scintillator. The units for energy are MeV/u. The universal delay constant that is taken when the differences between the E_{resc} values are minimized across the 5 $LaBr_3$:Ce detectors has been rounded to 5 decimal places. The other values in this table are exact. Figure 5.4 shows the timing data centroid for Detector 0 and an outlier taken for the centroid that is shown by Detector 4. This centroid is an outlier because it corresponds to a value of Z_{resm} that is significantly different from the other Z_{resm} values taken at 2.3 Torr. The initial beam energy E_{in}, mass of an individual beam nucleus which is called the beam mass, L, and the radio frequency pulse period are common to all experimental runs while the final beam energy E_{out} varies with pressure for these runs due to energy loss. Table 5.2 lists the different values of E_{out} for the experimental runs involving the $LaBr_3$:Ce detectors. Figure 5.5 shows the centroid for BGO detector #6 which is at its usual location in the DRAGON array as given in Table A7.

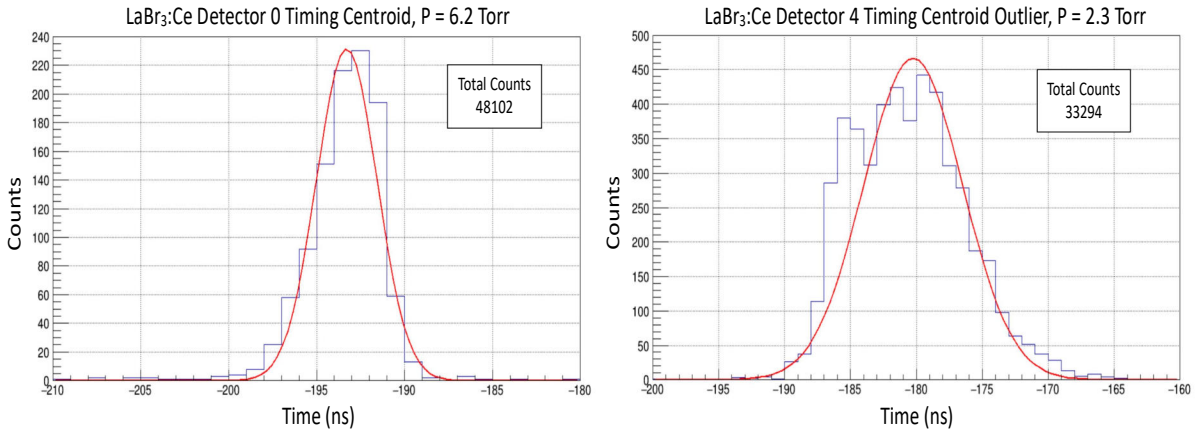

(a) (b)

Figure 5.4: (a) The timing centroid data can be clearly modelled by a Gaussian function in red. (b) The timing centroid data can be modelled by a Gaussian function in red for the outlier. However, the fit is poor.

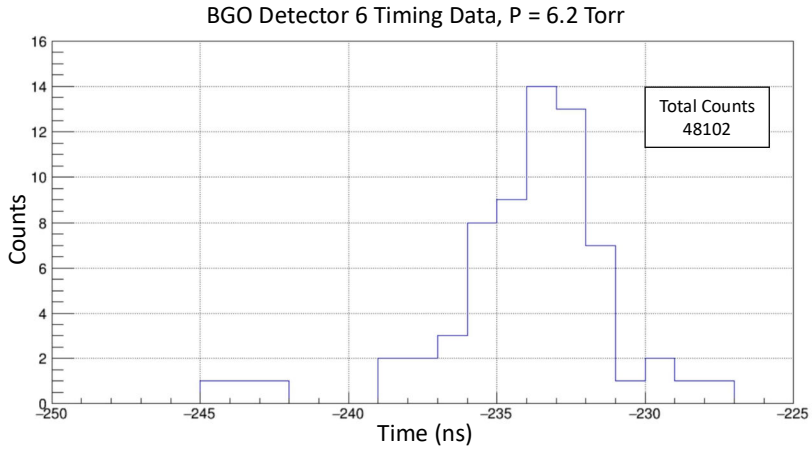

Figure 5.5: These timing data could be modelled by a Gaussian function but it would not be accurate due to the low count statistics.

Table 5.1: The values that are used for the calibration run are listed here.

Parameter	Value
Actual Resonance Energy (MeV/u)	0.475
Beam Mass (amu)	22
Universal Delay (ns)	46.10079
E_{in} (MeV/u)	0.48347
E_{out} (MeV/u)	0.46888
L (cm)	12.3
P (Torr)	4.4
Radio Frequency Pulse Period (ns)	84.9
TDC (ns)	-177.43
δTDC (ns)	1.54593

Table 5.2: The E_{out} values for the different pressure values are listed here.

Pressure (Torr)	E_{out} (MeV/u)
2.3	0.47600
3.3	0.47190
4.8	0.46810
6.2	0.46215

Figure 5.6 shows the comparison between the values of Z_{resc} and Z_{resm} for Detector 0 and Detector 1 in regards to P. Figure 5.7 continues the comparison for Detector 2 and Detector 3. Figure 5.8 concludes the comparison on Detector 4 where the peak distortion that is shown on Figure 5.4b has caused the Z_{resc} and Z_{resm} values to significantly disagree. In regards to these figures, as the pressure increases, more energy is lost by the beam per unit length and the resonance is reached at a smaller distance from the target entrance. Therefore, the resonance position follows an inversely proportional relationship to the pressure. The "Zresc Curve" is plotted according to Equation 5.4 by using the values in Table 5.1 and the pressure values in

Table 5.2. The data analysis was performed by using the standard ROOT commands where a Gaussian fit is applied onto the event peaks [62]. For the purpose of error propagation, the relative uncertainty in energy is $\pm 0.15\%$, the uncertainty in pressure is ± 0.01 Torr, and the uncertainty in measuring the effective length is ± 0.1 cm. The relative uncertainty for M and M_{LA} is taken from TDC and TDC_{LA}, respectively, which is given by the Gaussian fit. The variables that are involved are considered to have no correlation between each other. In Appendix A, Table A11 lists the error bar values for TDC_{LA} as well as their corresponding TDC_{LA} values. Different values of D are calculated for each individual detector to more accurately characterize them since the delay in the electronics depends on their individual positions as shown in Table A12. Table A13 summarizes the data for E_{resc} and Z_{resc}. Table A14-A18 summarize the data for E_{resm} and Z_{resm}. The energy values have been rounded to 5 decimal places, and the position values have been rounded to 4 decimal places to clearly show the small differences between them.

Aside from the outliers that are shown on Figure 5.7b and 5.8, the timing method can reliably be used to estimate the resonance energy even though the measured positions may differ from the calculated positions. The outliers for Figure 5.8 occur because the peak has been distorted, so the Gaussian fit needs to be shifted slightly to the left to more accurately model this peak. Figure 5.6 and Figure 5.7 show that the best resonance position results are obtained for Detector 0, 1, and 2. The average resonance energy measured by the 5 $LaBr_3$:Ce detectors is 0.47428 ± 0.00359 MeV/u which agrees with the actual resonance energy value of

0.475 MeV/u within error. Figure 5.9, 5.10, and 5.11 compare the E_{resm} values to the E_{resc} values as well as 0.475 MeV/u to illustrate data agreement. The uncertainties for ΔE_{resc} are calculated by using Equation 5.7 to avoid double counting errors. The relative uncertainty of $\frac{\Delta E}{E}$ is 0.0015 to represent $\pm 0.15\%$ and it is counted 3 times to take into account the E_{in} uncertainty, the E_{out} uncertainty of the experimental run for the plastic detector, and the E_{out} uncertainty of an experimental run for a $LaBr_3$:Ce detector. The same equation is used to determine the uncertainties for Z_{resc} where $\frac{\Delta E}{E}$ is counted twice since the experimental runs for a $LaBr_3$:Ce detector are not involved in determining Z_{resc}. The relative uncertainty of $\frac{\Delta P}{P}$ is about 0.0023 to represent $\frac{\pm 0.01\ Torr}{4.4\ Torr}$ for the plastic detector and this uncertainty is taken again for a $LaBr_3$:Ce detector where the pressure is 2.3 Torr, 3.3 Torr, 4.8 Torr, or 6.2 Torr. The pressure value corresponds to an experimental run as indicated by P_r. The relative uncertainty of $\frac{\Delta L}{L}$ is about 0.0081 to represent $\frac{\pm 0.1\ cm}{12.3\ cm}$, which takes into account the uncertainty of the effective length.

$$\frac{\Delta Z_{resc}}{Z_{resc}} = \sqrt{2\left(\frac{\Delta E}{E}\right)^2 + \left(\frac{\Delta P}{P}\right)^2 + \left(\frac{\Delta P}{P_r}\right)^2 + \left(\frac{\Delta L}{L}\right)^2} \tag{5.7a}$$

$$\frac{\Delta E_{resc}}{E_{resc}} = \sqrt{3\left(\frac{\Delta E}{E}\right)^2 + \left(\frac{\Delta P}{P}\right)^2 + \left(\frac{\Delta P}{P_r}\right)^2 + \left(\frac{\Delta L}{L}\right)^2} \tag{5.7b}$$

The uncertainties for Z_{resm} and E_{resm} are calculated by using Equation 5.8 to avoid double counting errors. $\frac{\Delta TDC}{TDC}$ represents the relative uncertainty provided by the FWHM of the Gaussian peak which is fitted to the plastic detector timing data. Likewise, $\frac{\Delta TDC_{LA}}{TDC_{LA}}$ represents the relative uncertainty provided by the FWHM of the Gaussian fit to the timing data of a

$LaBr_3$:Ce detector. δTDC and δTDC_{LA} are given as σ values which are converted to FWHM values and divided by their respective TDC and TDC_{LA} values to represent the time resolution of the plastic detector and a $LaBr_3$:Ce detector, respectively. $\frac{\Delta v_{avg}}{v_{avg}}$ determines the average beam velocity uncertainty which comes from the uncertainty in E_{in} and E_{out} for a $LaBr_3$:Ce detector. The relative uncertainty of $\frac{\Delta v_{out}}{v_{out}}$ is half of the relative uncertainty of $\frac{\Delta E_{out}}{E_{out}}$ for the experimental run of the plastic detector. These relative uncertainties are halved since the square root of E_{in} and E_{out} is taken to calculate v_{in} and v_{out} respectively in Equation 5.2b. The relative uncertainty of $\frac{\Delta L}{L}$ is taken into account to propagate the error of Z_{resm} to E_{resm}.

$$FWHM = 2\sqrt{2ln(2)}\sigma\ [ns] \tag{5.8a}$$

$$\Delta v_{avg} = \frac{1}{2}\sqrt{(0.0015v_{in})^2 + (0.0015v_{out})^2}\ \left[\frac{cm}{ns}\right] \tag{5.8b}$$

$$\frac{\Delta Z_{resm}}{Z_{resm}} = \sqrt{\left(\frac{\Delta TDC}{TDC}\right)^2 + \left(\frac{\Delta TDC_{LA}}{TDC_{LA}}\right)^2 + \left(\frac{\Delta v_{out}}{v_{out}}\right)^2 + \left(\frac{\Delta v_{avg}}{v_{avg}}\right)^2} \tag{5.8c}$$

$$\frac{\Delta E_{resm}}{E_{resm}} = \sqrt{\left(\frac{\Delta TDC}{TDC}\right)^2 + \left(\frac{\Delta TDC_{LA}}{TDC_{LA}}\right)^2 + \left(\frac{\Delta v_{out}}{v_{out}}\right)^2 + \left(\frac{\Delta v_{avg}}{v_{avg}}\right)^2 + \left(\frac{\Delta L}{L}\right)^2} \tag{5.8d}$$

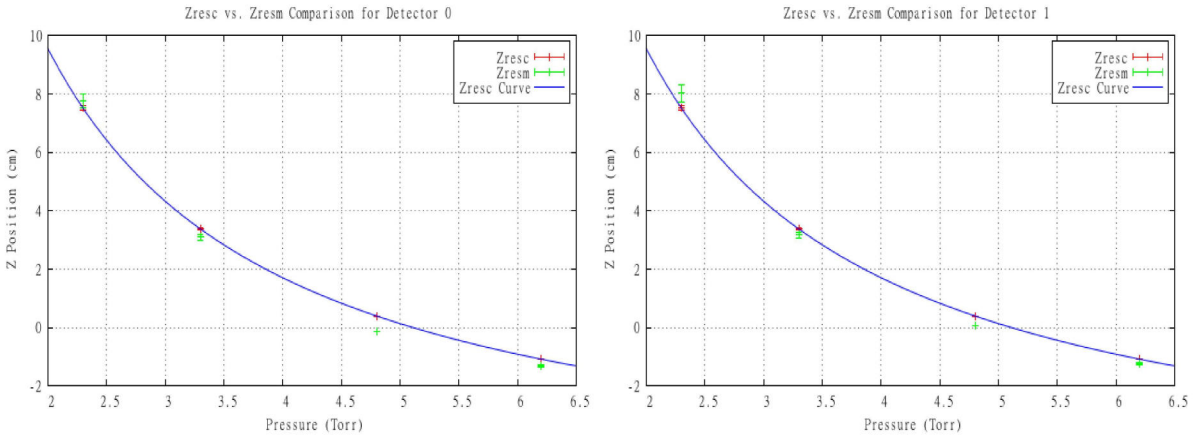

(a) (b)

Figure 5.6: (a) The measured values for the Z positions and the calculated values are shown for Detector 0. (b) The measured values for the Z positions and the calculated values are shown for Detector 1.

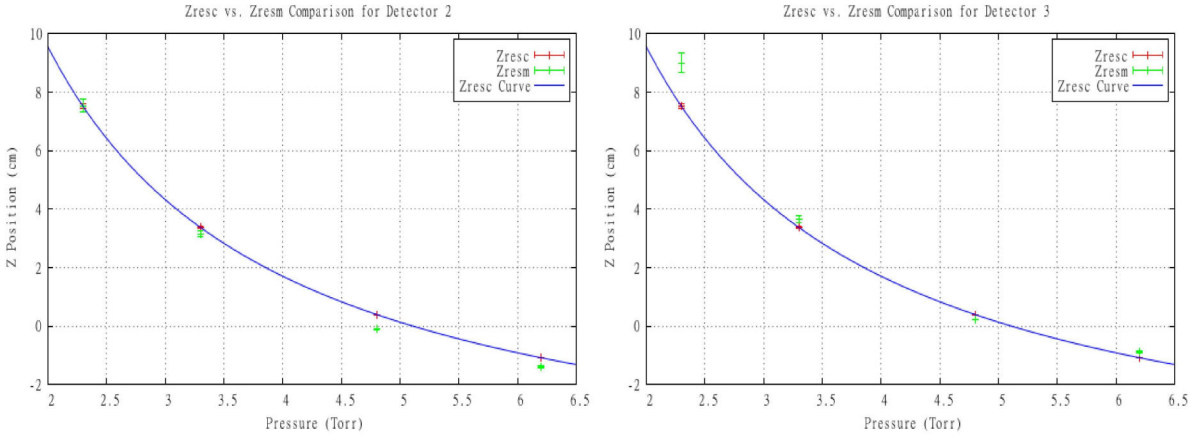

(a) (b)

Figure 5.7: (a) The measured values for the Z positions and the calculated values are shown for Detector 2. (b) The measured values for the Z positions and the calculated values are shown for Detector 3 where a significant disagreement is shown at 2.3 Torr.

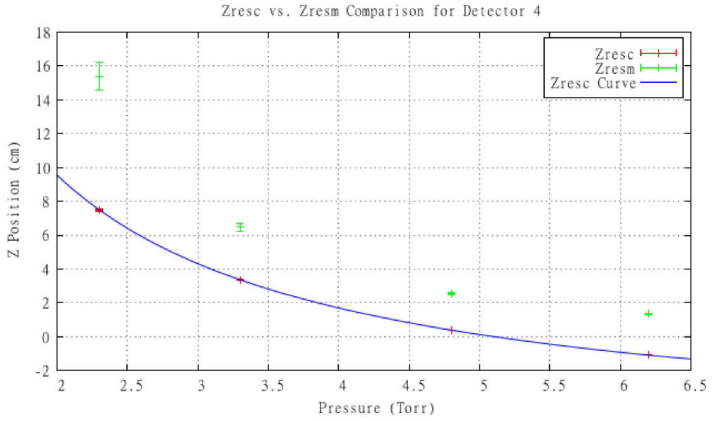

Figure 5.8: The measured values for the Z positions and the calculated values are shown for Detector 4 where they significantly disagree.

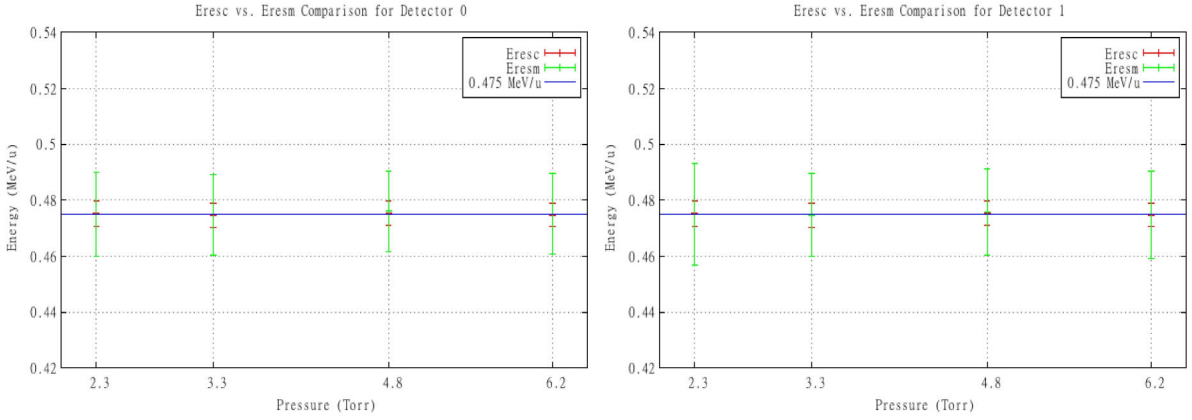

(a) (b)

Figure 5.9: (a) The measured resonance energies and the calculated values are shown for Detector 0. (b) The measured resonance energies and the calculated values are shown for Detector 1.

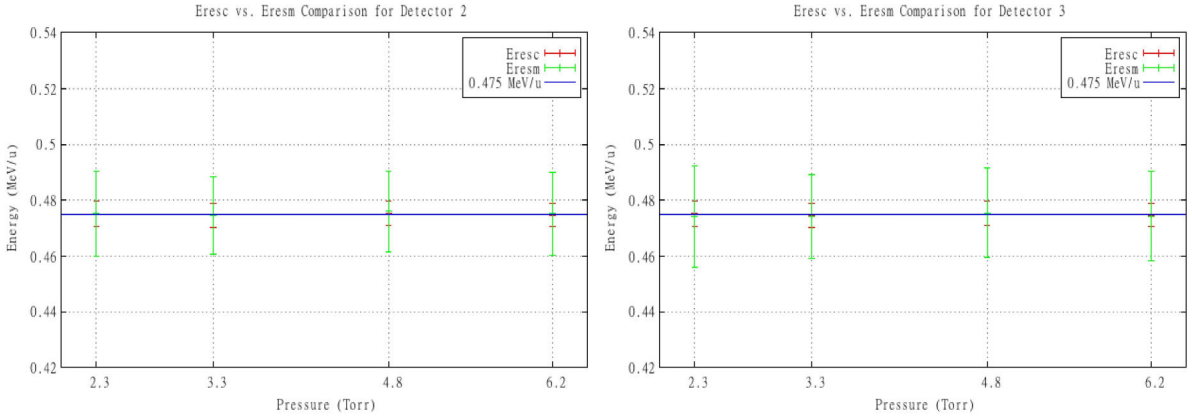

(a) (b)

Figure 5.10: (a) The measured resonance energies and the calculated values are shown for Detector 2. (b) The measured resonance energies and the calculated values are shown for Detector 3.

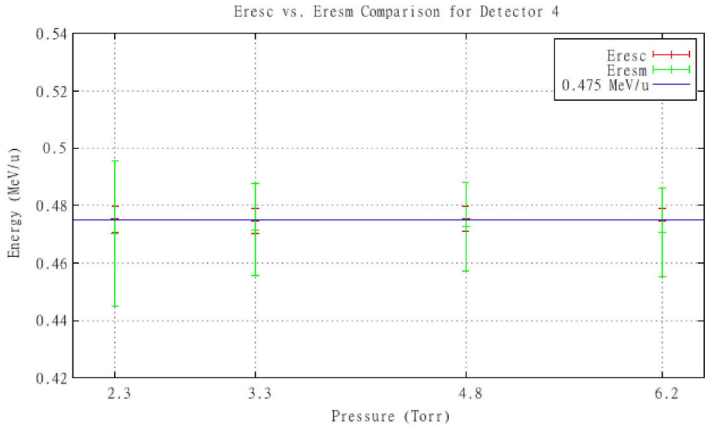

Figure 5.11: The Z_{resm} values cause the E_{resm} values to be below the true resonance energy value. However, they still agree with the calculated energies and the true value within error for Detector 4.

5.3 Other Experimental Timing Errors

The errors attributed to the dead time of the electronics have not been quantified because they are considered to be negligibly small compared to the sources of error that have been presented. In addition, the gamma ray time of flight to the $LaBr_3$:Ce detectors is not taken into account because it is negligibly small compared to the timing centroid data. The uncertainties are simplistically modelled to avoid overestimating them, so a rigorous analysis of the error bars for the resonance reaction positions and energies could be performed. The delays in the electronics have been analytically determined, so the uncertainties in the delays are considered to be zero.

Chapter 6

Conclusion

In regards to the BGO detector and the $LaBr_3$:Ce detector efficiency results, they agree within error when the experimental values and the simulation values are compared to each other. The BGO experimental data were quoted from Gigliotti (2004) [3]. The $LaBr_3$:Ce detector energy resolution values are within the range of the literature values. The purpose of comparing the detector efficiency and the energy resolution to other studies is to check the accuracy of the results. The comparisons generally suggest that the data are reliable so they can be used as a reference in future studies.

The Geant4 simulation overestimates the detector efficiency at high energies so its energy loss physics could be improved. The Gaussian fitting program uses a simple cubic fitting function to estimate the background on the experimental data, which may not always be accurate. A more detailed treatment of the background may be done to further improve the accuracy of

the results. The Gaussian fitting program could also be improved to match the width of the photopeak data. The 2 step decay of ^{60}Co could be taken into account when the experimental efficiency values are calculated to see if there is a difference in the results. The dead time of the MIDAS acquisition system could also be calculated for this purpose.

Overall, the results show that the $LaBr_3$:Ce detector has better energy resolution and time resolution than the BGO detector, while being less efficient at capturing gamma rays. The results of the BGO and $LaBr_3$:Ce detector efficiency calibration experiments demonstrate the trade off between efficiency and energy resolution. Therefore, the $LaBr_3$:Ce detector is favoured for experiments that require accurate results, and where the number of gamma ray events is not required to be particularly high; quality over quantity. However, further work may be required to investigate the differences between the simulation and experimental data to see if their differences have not been obscured by the error bars. Large data samples may enable inferential statistical analysis. The results of the $LaBr_3$:Ce detector timing experiments show that the timing method is a viable method of estimating the resonance energies of nuclear reactions, even though most of the position results do not agree within the error bars. The superior time resolution of the $LaBr_3$:Ce detector over the BGO detector is the reason why the timing method works better for it, although more investigative work may be required to confirm data agreement for the resonance reaction positions, and to examine detectors that may be further away from the gas target centre along the positive z-axis.

This thesis has been concluded. Appendix A provides the details on the detectors for the simulations and the experiments as well as the DRAGON detector array. Appendix B provides a guide on how to use the Gaussian fitting program. Appendix C provides a guide on how to use the Geant4 simulation and it presents some of its figures. A link to the Geant4 code is also provided. Appendix D lists the references.

Appendix A

Data Tables

Table A1: The $LaBr_3$:Ce detector's component materials and positions for the single detector simulations are provided here. A vacuum is enclosed within the photomultiplier tube. These positions are measured relative to the origin which is at the centre of the detector. The photocathode component is inside of the photomultiplier tube, and it is just behind the optical window.

Detector Component	Material	Z Position (cm)
Photomultiplier Tube	Pyrex Glass Shell Surrounding Vacuum	-2.875
Vacuum	None	-2.875
Photocathode	CsKSb [63]	-0.029
Optical Window	Polydimethylsiloxane [64]	0.325
Scintillator	$LaBr_3$:Ce	2.965
Gap Face	Magnesium Oxide	5.715
Aluminium Case	Aluminium	3.1
Aluminium Case Face	Aluminium	5.95

Table A2: The $LaBr_3$:Ce detector's component dimensions for the single detector simulations are provided here. The photomultiplier tube thickness on its ends allow the photocathode to be inserted on its front end. These values were obtained from the schematic diagrams of the single $LaBr_3$:Ce detector. The photocathode component is inside of the photomultiplier tube, and it is just behind the optical window.

Detector Component	Dimension (cm)
Photomultiplier Tube Length	6.20±0.05
Photomultiplier Tube Radius	2.55
Photomultiplier Tube Thickness	0.508
Vacuum Length	5.184
Vacuum Radius	2.3
Photocathode Radius	2.3
Photocathode Thickness	0.508
Scintillator Length	5.08
Scintillator Radius	2.54
Optical Window Radius	2.54
Optical Window Thickness	0.200±0.016
Aluminium Case Length	5.75
Aluminium Case Radius	2.59
Aluminium Case Thickness	0.05
Gap Face Radius	2.54
Gap Face Thickness	0.420±0.034
Aluminium Case Face Radius	2.54
Aluminium Case Face Thickness	0.05

Table A3: The BGO detector's component materials and positions for the single detector simulations are provided here. The positions are measured relative to the origin which is at the centre of the detector. The photocathode is part of the photomultiplier tube, and it is just behind the scintillator crystal.

Detector Component	Material	Z Position (cm)
Photomultiplier Tube	Pyrex Glass Shell Surrounding Vacuum	-4.0005
Vacuum	None	-4.0005
Photocathode	CsKSb [63]	5.995
Scintillator	BGO	10.059
Aluminium Case	Aluminium	10.2495
Aluminium Case Face	Aluminium	14.21825
Gap	Magnesium Oxide	10.21775
Gap Face	Magnesium Oxide	14.02775

Table A4: The DRAGON array's BGO detector component dimensions that are also used for the single detector simulations are provided here. The materials that are listed in Table A3 are used for the detectors in the hexagonal array. The photomultiplier tube thickness on its ends allow the photocathode to be inserted on its front end. The photocathode is part of the photomultiplier tube, and it is just behind the scintillator crystal. The radii refer to the radii of the incircles that would be formed within the hexagonal components. These values were derived from the detector component dimensions in Geant3. Credit is given to Lorenzo Principe and Dario Gigliotti for providing these dimensions.

Detector Component	Dimension (cm)
Photomultiplier Tube Length	20.499
Photomultiplier Tube Radius	2.95
Photomultiplier Tube Thickness	0.508
Vacuum Length	19.483
Vacuum Radius	2.79
Photocathode Radius	2.79
Photocathode Thickness	0.508
Scintillator Length	7.62
Scintillator Radius	2.79
Aluminium Case Length	8.001
Aluminium Case Radius	2.889
Aluminium Case Thickness	0.0635 [3]
Aluminium Case Face Radius	2.8255
Aluminium Case Face Thickness	0.0635 [3]
Gap Length	7.9375
Gap Radius	2.8255
Gap Thickness	0.0355 [3]
Gap Face Radius	2.79
Gap Face Thickness	0.3175 [3]

Table A5: The dimensions of the gas target box and its components for the simulations are provided here. The trapezoid wall thickness where the entrance and exit holes are placed is given. The trapezoid collimator thickness has been rounded to 3 decimal places.

Box Component Dimension	Simulation Value (cm)
External Box Length	25.718
External Box Width	17.146
External Box Depth	4.762
Box Thickness	0.317
Entrance and Exit Hole Radius	0.95
Upper External Trapezoid Length	13.518
Lower External Trapezoid Length	3.802
External Trapezoid Depth	3.81
External Trapezoid Width	8.416
Trapezoid Thickness	0.317
Trapezoid Hole Radius	0.8
Trapezoid Disk Radius	0.79
Trapezoid Disk Thickness	0.078
Entrance Trapezoid Collimator Radius	0.3 [43]
Exit Trapezoid Collimator Radius	0.4 [43]
Trapezoid Collimator Thickness	0.090

Table A6: The positions of the gas target box and its components are provided here with 3 or 4 decimal places. These positions are measured relative to the origin in Figure 3.5.

Box Component	(X,Y, Z) Position (cm)
Box	(0, -9.684, 0)
Entrance Hole	(0, 0, -8.4145)
Exit Hole	(0, 0, 8.4145)
Trapezoid	(0, -2.029, 0)
Trapezoid Entrance Hole	(0, 0, -5.319)
Trapezoid Entrance Disk	(0, 0, -5.457)
Trapezoid Entrance Collimator	(0, 0, -5.457)
Trapezoid Exit Hole	(0, 0, 5.319)
Trapezoid Exit Disk	(0, 0, 5.457)
Trapezoid Exit Collimator	(0, 0, 5.457)

Table A7: The positions of the left-hand array BGO detectors and their corresponding scintillators in the DRAGON array are provided here. These positions are measured relative to the origin. Detector #1, #2, #8, and #10 straddle the array. Detector #3, #4, #5, #6, #7, and #9 form the crown of the array. The other detectors are on the right-hand positions of the array. Credit is given to Lorenzo Principe for providing the Geant3 scintillator positions.

Detector	Detector (X,Y, Z) Position (cm)	Scintillator (X,Y, Z) Position (cm)
1	(-1.8, -4.96, -14.78)	(8.259, -4.96, -14.78)
2	(-9, -10.08, -11.83)	(1.059, -10.08, -11.83)
3	(-2.299, 4.96, -11.83)	(7.76, 4.96, -11.83)
4	(-9, 10.08, -8.87)	(1.059, 10.08, -8.87)
5	(-9, 7.68, -2.96)	(1.059, 7.68, -2.96)
6	(-9, 7.68, 2.96)	(1.059, 7.68, 2.96)
7	(-9, 10.08, 8.87)	(1.059, 10.08, 8.87)
8	(-9, -10.08, 11.83)	(1.059, -10.08, 11.83)
9	(-9, 4.96, 11.83)	(1.059, 4.96, 11.83)
10	(-9, -4.96, 14.78)	(1.059, -4.96, 14.78)
11	(-17.849, -2.56, -8.87)	(-7.79, -2.56, -8.87)
13	(-17.849, -7.68, -5.91)	(-7.79, -7.68, -5.91)
15	(-17.849, 2.56, -5.91)	(-7.79, 2.56, -5.91)
17	(-17.849, -2.56, -2.96)	(-7.79, -2.56, -2.96)
19	(-17.849, -7.68, 0.00)	(-7.79, -7.68, 0.00)
21	(-17.849, 2.56, 0.00)	(-7.79, 2.56, 0.00)
23	(-17.849, -2.56, 2.96)	(-7.79, -2.56, 2.96)
25	(-17.849, -7.68, 5.91)	(-7.79, -7.68, 5.91)
27	(-17.849, 2.56, 5.91)	(-7.79, 2.56, 5.91)
29	(-17.849, -2.56, 8.87)	(-7.79, -2.56, 8.87)

Table A8: The positions of the right-hand array BGO detectors and their corresponding scintillators in the DRAGON array are provided here. These positions are measured relative to the origin. Credit is given to Lorenzo Principe for providing the Geant3 scintillator positions.

Detector	Detector (X,Y, Z) Position (cm)	Scintillator (X,Y, Z) Position (cm)
12	(17.849, -2.56, -8.87)	(7.79, -2.56, -8.87)
14	(17.849, -7.68, -5.91)	(7.79, -7.68, -5.91)
16	(17.849, 2.56, -5.91)	(7.79, 2.56, -5.91)
18	(17.849, -2.56, -2.96)	(7.79, -2.56, -2.96)
20	(17.849, -7.68, 0.00)	(7.79, -7.68, 0.00)
22	(17.849, 2.56, 0.00)	(7.79, 2.56, 0.00)
24	(17.849, -2.56, 2.96)	(7.79, -2.56, 2.96)
26	(17.849, -7.68, 5.91)	(7.79, -7.68, 5.91)
28	(17.849, 2.56, 5.91)	(7.79, 2.56, 5.91)
30	(17.849, -2.56, 8.87)	(7.79, -2.56, 8.87)

Table A9: The approximate source activities during the experiments along with their corresponding activity uncertainties are provided here. These uncertainties are reported by the manufacturers as percentages of the source activities. The corresponding branching ratio for each gamma decay is shown. The source activities have been rounded to 5 decimal places to approximately give the numbers that were actually used to calculate the efficiency values of the $LaBr_3$:Ce detector.

Source Energy (MeV)	Activity (Bq)	Activity Uncertainty ($\pm$%)	Branching Ratio
0.511	32343.74764	3	1.8
0.6617	164613.10093	3.7	0.851
1.17	2184.79321	1.9	1.0
1.27	32343.74764	3	1.0
1.33	2184.79321	1.9	1.0

Table A10: The run time and the number of gates that are produced during each run are provided here. The run time is divided by the internal radiation run time to calculate the "Normalization Factor", where 9 decimal places are given. The counts on the internal radiation spectrum is multiplied by this factor when it is added to a given spectrum to subtract the internal radiation of the ^{138}La isotope from the spectrum.

Source	Position	Run Time (seconds)	Normalization Factor	Gates
^{22}Na	1	1590	-0.010832686	4006156
^{22}Na	2	1742	-0.011868264	1755897
^{22}Na	3	8009	-0.054565398	3536406
^{60}Co	1	7607	-0.051826568	1650723
^{60}Co	2	14575	-0.099299623	2240319
^{60}Co	3	89864	-0.612244342	11481549
^{137}Cs	1	1124	-0.007657823	4319158
^{137}Cs	2	1696	-0.011554865	2517764
^{137}Cs	3	4593	-0.031292156	2587144
^{138}La	Internal	146778	1	17166502

Table A11: The centroid time stamps that are shown by the $LaBr_3$:Ce detectors are given as TDC_{LA}. Likewise, their uncertainties are given as δTDC_{LA}.

Detector	P (Torr)	TDC_{LA} (ns)	δTDC_{LA} ($\pm$ns)
0	2.3	-183.839	1.78010
0	3.3	-188.687	1.65189
0	4.8	-192.053	1.67006
0	6.2	-193.293	1.72017
1	2.3	-183.355	2.40741
1	3.3	-188.396	1.75451
1	4.8	-191.644	1.92096
1	6.2	-192.992	1.98845
2	2.3	-186.994	1.81727
2	3.3	-191.547	1.54001
2	4.8	-194.966	1.72718
2	6.2	-196.307	1.82157
3	2.3	-183.655	2.43029
3	3.3	-189.204	1.82072
3	4.8	-192.811	2.05592
3	6.2	-193.955	2.09207
4	2.3	-180.246	3.74604
4	3.3	-189.529	2.07452
4	4.8	-193.617	1.92747
4	6.2	-194.877	1.99574

Table A12: The individual delay constants D are given for each $LaBr_3$:Ce detector. They have been rounded to 5 decimal places.

Detector	D (ns)
0	47.30160
1	47.50390
2	44.36364
3	46.18329
4	42.92543

Table A13: The E_{resc} and Z_{resc} values are given along with their uncertainties δE_{resc} and δZ_{resc}.

P (Torr)	E_{resc} (MeV/u)	δE_{resc} ($\pm$MeV/u)	Z_{resc} (cm)	δZ_{resc} ($\pm$cm)
2.3	0.47517	0.00468	7.5102	0.0731
3.3	0.47451	0.00443	3.3708	0.0311
4.8	0.47529	0.00431	0.3955	0.0035
6.2	0.47469	0.00426	-1.0825	0.0096

Table A14: The E_{resm} and Z_{resm} values are given along with their uncertainties δE_{resm} and δZ_{resm} for Detector 0.

P (Torr)	E_{resm} (MeV/u)	δE_{resm} ($\pm$MeV/u)	Z_{resm} (cm)	δZ_{resm} ($\pm$cm)
2.3	0.47503	0.01509	7.7445	0.2378
3.3	0.47478	0.01435	3.0857	0.0898
4.8	0.47596	0.01434	-0.1371	0.0040
6.2	0.47509	0.01447	-1.3179	0.0387

Table A15: The E_{resm} and Z_{resm} values are given along with their uncertainties δE_{resm} and δZ_{resm} for Detector 1.

P (Torr)	E_{resm} (MeV/u)	δE_{resm} ($\pm$MeV/u)	Z_{resm} (cm)	δZ_{resm} ($\pm$cm)
2.3	0.47487	0.01805	8.0148	0.2976
3.3	0.47470	0.01478	3.1706	0.0953
4.8	0.47571	0.01538	0.0604	0.0019
6.2	0.47493	0.01559	-1.2239	0.0389

Table A16: The E_{resm} and Z_{resm} values are given along with their uncertainties δE_{resm} and δZ_{resm} for Detector 2.

P (Torr)	E_{resm} (MeV/u)	δE_{resm} ($\pm$MeV/u)	Z_{resm} (cm)	δZ_{resm} ($\pm$cm)
2.3	0.47516	0.01512	7.5362	0.2318
3.3	0.47471	0.01382	3.1603	0.0883
4.8	0.47593	0.01447	-0.1133	0.0033
6.2	0.47522	0.01477	-1.3904	0.0417

Table A17: The E_{resm} and Z_{resm} values are given along with their uncertainties δE_{resm} and δZ_{resm} for Detector 3.

P (Torr)	E_{resm} (MeV/u)	δE_{resm} ($\pm$MeV/u)	Z_{resm} (cm)	δZ_{resm} ($\pm$cm)
2.3	0.47427	0.01812	8.9942	0.3358
3.3	0.47424	0.01501	3.6615	0.1120
4.8	0.47553	0.01591	0.2072	0.0067
6.2	0.47434	0.01597	-0.8833	0.0289

Table A18: The E_{resm} and Z_{resm} values are given along with their uncertainties δE_{resm} and δZ_{resm} for Detector 4.

P (Torr)	E_{resm} (MeV/u)	δE_{resm} ($\pm$MeV/u)	Z_{resm} (cm)	δZ_{resm} ($\pm$cm)
2.3	0.47039	0.02526	15.3918	0.8170
3.3	0.47160	0.01601	6.4698	0.2133
4.8	0.47260	0.01523	2.5502	0.0795
6.2	0.47048	0.01539	1.3419	0.0425

Appendix B

Gaussian Fitting Program Usage

The website link for this program is given here: https://isdaq00.triumf.ca/~dragon/Collection/DataPlot6.1.6/index.php. Both the username and the password that are required to enter this website is "midas". This program is coded in PHP (Hypertext Preprocessor) and HTML5 (Hyper Text Markup Language 5) is used to display it. In order to use it, one must first register an account to log in. This program is designed to handle text files so any data files need to be converted into the ".txt" format first before using this program. After one logs in, the following screen is displayed in Figure B1. One may then insert the chosen files and click on "Plot". The example that is shown in Figure B1 is for position 1 of ^{22}Na as run 478, and where run 480 represents the internal radiation of ^{138}La. Run 480 is multiplied by the corresponding "Normalization Factor" in Table A10 so when it is added to run 478, the internal radiation of ^{138}La is subtracted from run 478. In this case, the plot type needs to be "Sum" to specify that

the plots are added together and not being shown together as in "Stack".

This program can fit 1, 2, 3, or 4 photopeaks. The uncertainties for the channel counts were taken as the square root of the number of counts for each channel. They are shown if "Yes" is selected for the "Error Bars". The plots can be generated where the Gaussian fit function takes the background into account in "Data, BG, Gauss + BG". Alternatively, the plots can show the Gaussian fit function which disregards the background in "Data, BG, Gauss". All of the plots used for this thesis used the "Data, BG, Gauss + BG" option. There is an option to save the plot where the file directory must be specified. However, the save function has not been implemented. The range of channels for the plot to be displayed can also be specified, where all of the files that are being used begin on channel 0 and end on channel 4095. "Edit User Info" allows one to change the name, password, email, and phone number. "Clear All" clears all of the selections. Clicking on "Quit" opens a window that asks if one wants to log out or not. If one does not want to log out, the interface that is shown in Figure B1 is returned with all of the selections cleared.

Figure B2 shows the plot right after one clicks on "Plot", which displays the counts from channel 200 to channel 440. One is notified that the subtraction has been performed. Any channels with a negative number of counts are automatically set to have zero counts since the negative numbers have no physical meaning. Click on "New Data" to start a new plot or click on "Continue" to work with the existing plot. "App Info" has not been implemented, and "Fit Info" indicates that 5 points are needed to fit a single peak; 2 points on the left of the peak, 1

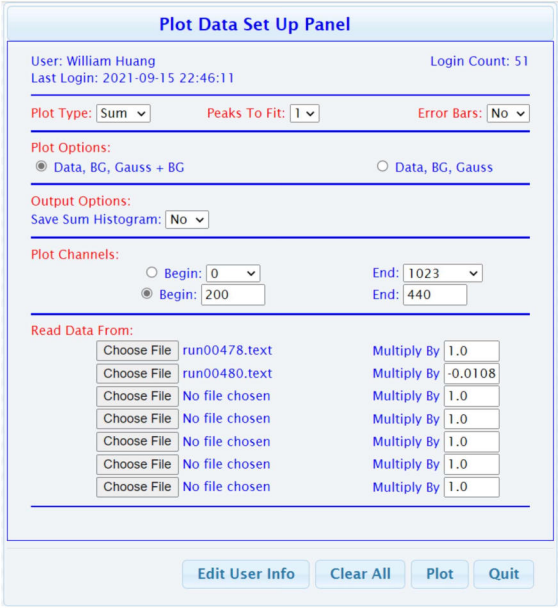

Figure B1: The Gaussian fitting program interface is shown with the specified files to be added.

point on the top of the peak, and 2 points on the right of the peak. The 2 points on the left of the peak are meant to estimate the average of the background on the left side, and the 2 points on the right of the peak fulfill this purpose for the right side. The fitting window is chosen so all of the chosen points are within this window to clearly display the data and its Gaussian fit. "Clear Selections" clears the selected channels before a fit is performed, and "Fit the Selection" performs a Gaussian fit. "To Set Up" asks if one wants to start a new plot and if so, it brings one back to the interface that is shown in Figure B1 with all of the selections cleared. "Back to Plot" clears the selections and the Gaussian fit. The source number is "R-00717" for Sodium-22, "R-00136C" for Cobalt-60, and "R-00094D" for Cesium-137 as labelled by

TRIUMF.

The "Total Counts" refer to all of the counts in a given spectrum, while the "Displayed Counts" refer to the counts that are shown within the field of view which is from channel 200 to channel 440 in this case. The "Norm Fact." shows why run 480 has a low number of total and displayed counts; they were reduced by about a factor of 92. The "Grand Total" shows the sum of the "Total Counts" in the spectra that were added together.

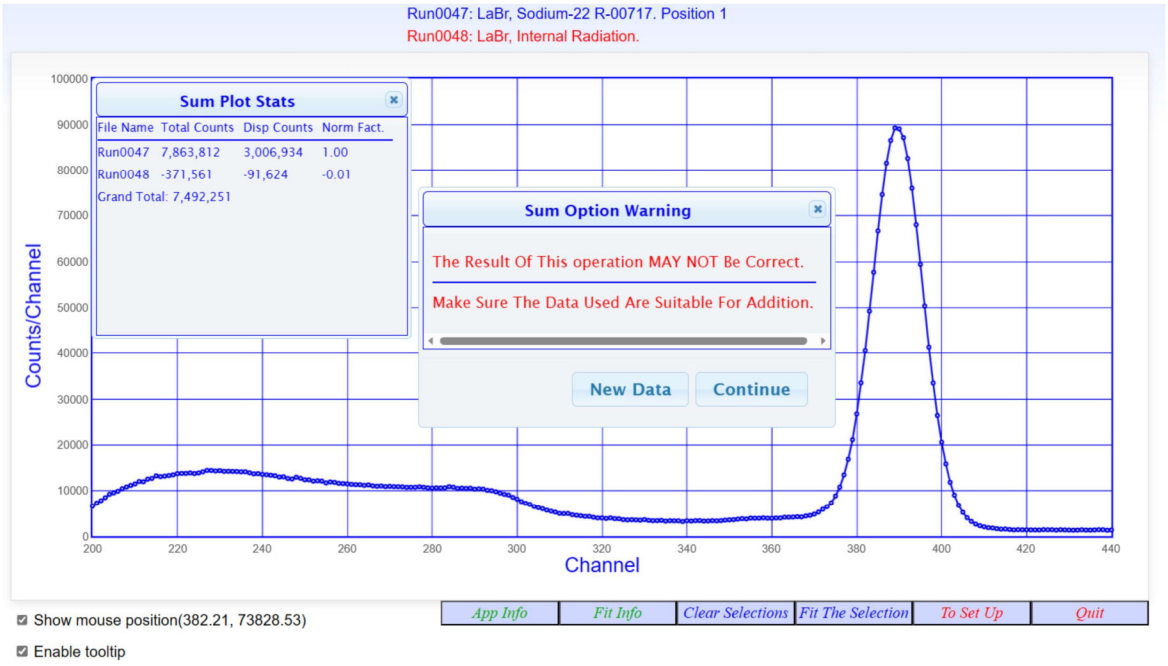

Figure B2: The spectrum that is generated by the addition of two spectra is shown along with the 0.511 MeV photopeak. The warning appears since subtracting the internal radiation counts from each channel may yield a negative number of counts for some channels. However, the program automatically sets these negative numbers to be zero since negative numbers of counts have no physical meaning.

For this example to fit 1 photopeak, channel 389 is taken at the top of the 0.511 MeV

photopeak for ^{137}Cs. Channel 335 and channel 348 were taken for the left background, while channel 420 and channel 429 were taken for the right background. The program will ask one to confirm these choices. If they are not confirmed, the plot that is shown in Figure B2 is returned. Once confirmed, the Gaussian fit program operates on the range of channels that begins with the leftmost channel and ends with the rightmost channel. A cubic function is used to fit the background, and the fitted background is subtracted from the photopeak. The 3 parameters of the Gaussian function which are the height, width, and the peak position are chosen to minimize the value of χ^2 to obtain the most accurate Gaussian fit for the selected channels. The FWHM of the Gaussian peak is taken for the width. The Gaussian parameters are varied in 20 small steps (around the corresponding experimental ones) one at a time, and finally the combination that produces the best χ^2 is used to generate the Gaussian curve that is plotted on top of the data. In doing so, the difference between the data and the Gaussian fit has been effectively minimized for each channel. The channels are chosen so that the χ^2 values for all of the experimental efficiency data are in between 0.99 and 1. The program will also estimate these parameters for the data themselves. The sum of the fitted background and the Gaussian peak area is not exactly equal to the peak area of the data because the background fitting function does not perfectly model the background. Figure B3 which is used for Figure 4.11 displays the results. The Gaussian peak area is used to calculate the $LaBr_3$:Ce detector efficiency. Since there is no save function, screenshots of the plots are taken to be saved.

In order to fit multiple photopeaks, the background between two photopeaks is assumed

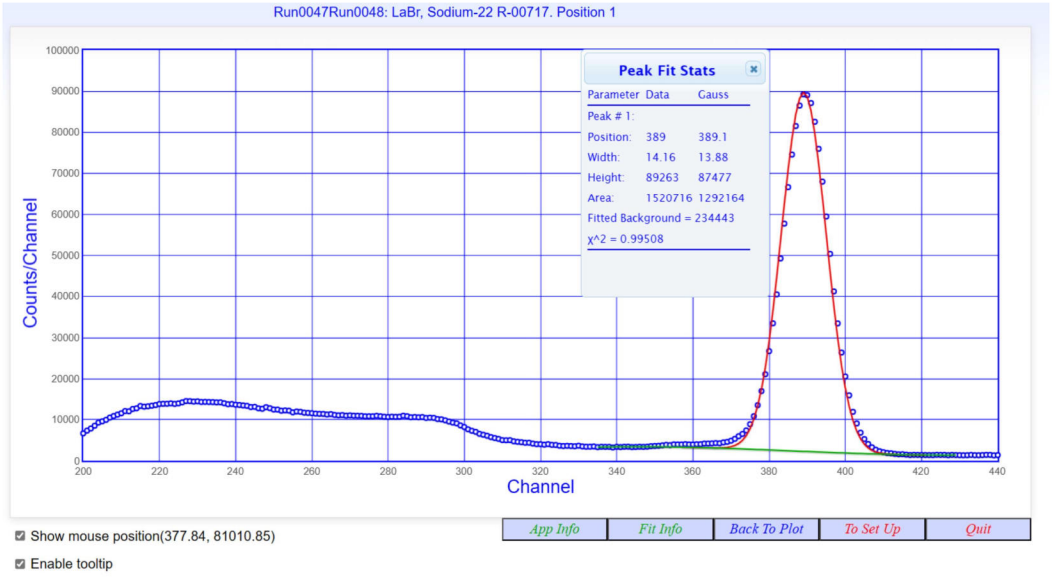

Figure B3: The Gaussian fit is performed on the 0.511 MeV photopeak.

to be shared between them. This means that the left background of one peak is the right background of the other peak. Therefore, 8 channels are required to fit 2 peaks, where the additional 2 channels are used to model the right background of the rightmost peak, and an additional channel is used for the top of the second peak. Likewise, 11 channels are required to fit 3 peaks, and 14 channels are required to fit 4 peaks. Figure B4 shows an example where the program fits the two photopeaks of ^{60}Co taken at position 1 for the gamma ray energies 1.17 MeV and 1.33 MeV. The Gaussian peak areas were not used to calculate the efficiency data, since the most accurate approach is to fit each photopeak individually. In regards to the ^{60}Co source, the best Gaussian fit is not taken by simply choosing the channel with the most counts as the peak since this channel may not be at the centre of the peak. The channel at the

centre of the peak is chosen for the 1.33 MeV peak for position 1 and the 1.17 MeV peak for position 2 so the Gaussian fit overlaps with the data as much as possible.

It is notable here that the y-axis is labelled "Counts/Channel" instead of "Counts". This is because when the Gaussian peak area is calculated by multiplying the height by the width, its height would have the units of "Counts/Channel" and its width would have the unit of "Channel", so the unit of the peak area is simply "Counts". The meaning of "Counts/Channel" is the number of counts in a given channel. A factor of $\sqrt{\frac{\pi}{4ln(2)}}$ which comes from the Gaussian integral is multiplied by the height and the width to take into account the shape of the Gaussian peak.

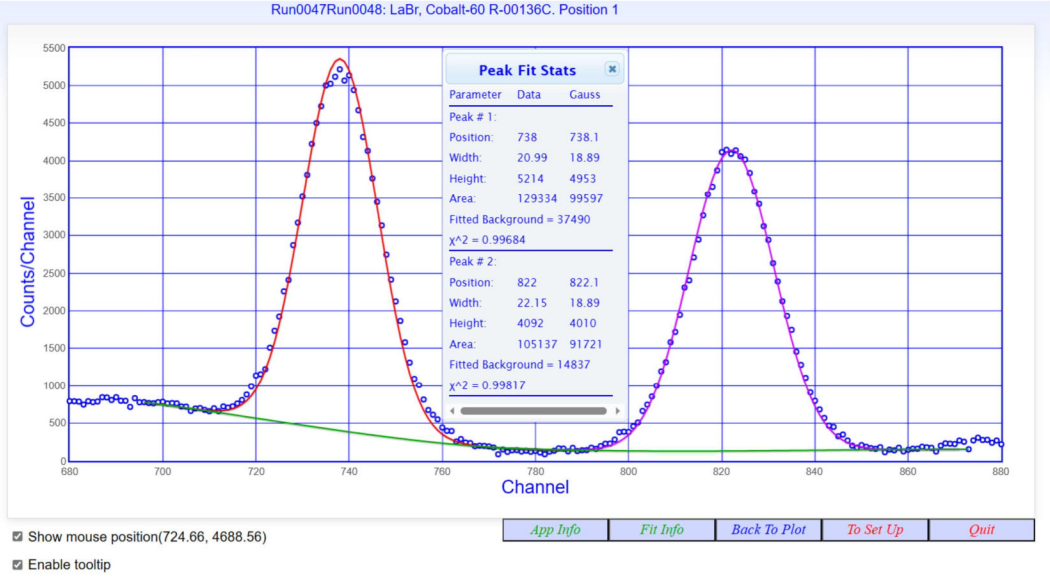

Figure B4: The Gaussian fit is performed on the 1.17 MeV photopeak and the 1.33 MeV photopeak simultaneously.

Appendix C

Geant4 Simulation Usage

A brief guide on how to use the Geant4 simulation is presented here and the details can be found online. The version of the Geant4 simulation that is being described is "sl6_x64-Geant4-10.01.p.01", which has been used to generate the $LaBr_3$:Ce efficiency data in this thesis [44,65]. The virtual machine can be downloaded from this link: https://geant4.cenbg.in2p3.fr/. It is installed in the form of a virtual machine, so it requires a program like VMware Workstation Player for Windows to run it. Open VMware and then click on "Create a New Virtual Machine". The virtual machine is opened from there by selecting the .vmx file or .vmdk file. The simulation that is used for this thesis has a .vmdk file named "sl6_x64" that is used to run the virtual machine, and VMware saves a shortcut so it can be opened on its front interface. Figure C1 shows this interface with the virtual machine shortcut.

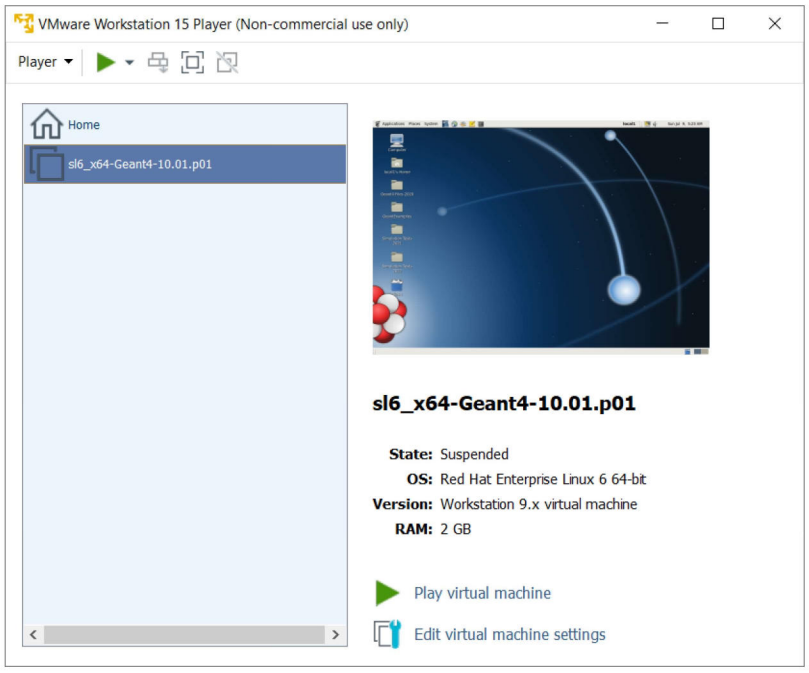

Figure C1: The VMware front interface is shown with the virtual machine shortcut selected.

Click on "Play virtual machine" to run the virtual machine. VMware will ask whether ths virtual machine has been moved or copied. Click on "I copied it" if this is not known so the virtual machine can have a system address. The virtual machine comes with some pre-made simulation examples, and the detector simulation is based on Example B4 as described in the Geant4 manual for application developers [66]. To set up the simulation, enter or make the directory that is called "LaBr3_v3-build" and open the terminal. For this simulation, type in "cmake -DGeant4_DIR=/home/local1/Desktop/GeantExamples/LaBr3_v3 /home/local1/Desktop/GeantExamples/LaBr3_v3", and include the space between the directories. Then type "make -jN", where N is the number of processors on the computer. For

example, a core i5 computer would need "make -j5". The commands may vary for different simulations but the general idea holds. Whenever the code is updated, the files need to be saved and the "make" command needs to be typed and executed in the terminal. The program is called "LaBr3_v3", and "./LaBr3_v3" is typed in the terminal to execute this program. Figure C2 shows the simulation interface when it is opened. The terminal must be opened in the correct directory which is inside the "LaBr3_v3-build" folder in this case. The Geant4 manual for application developers describes the details on the code for the simulations [66].

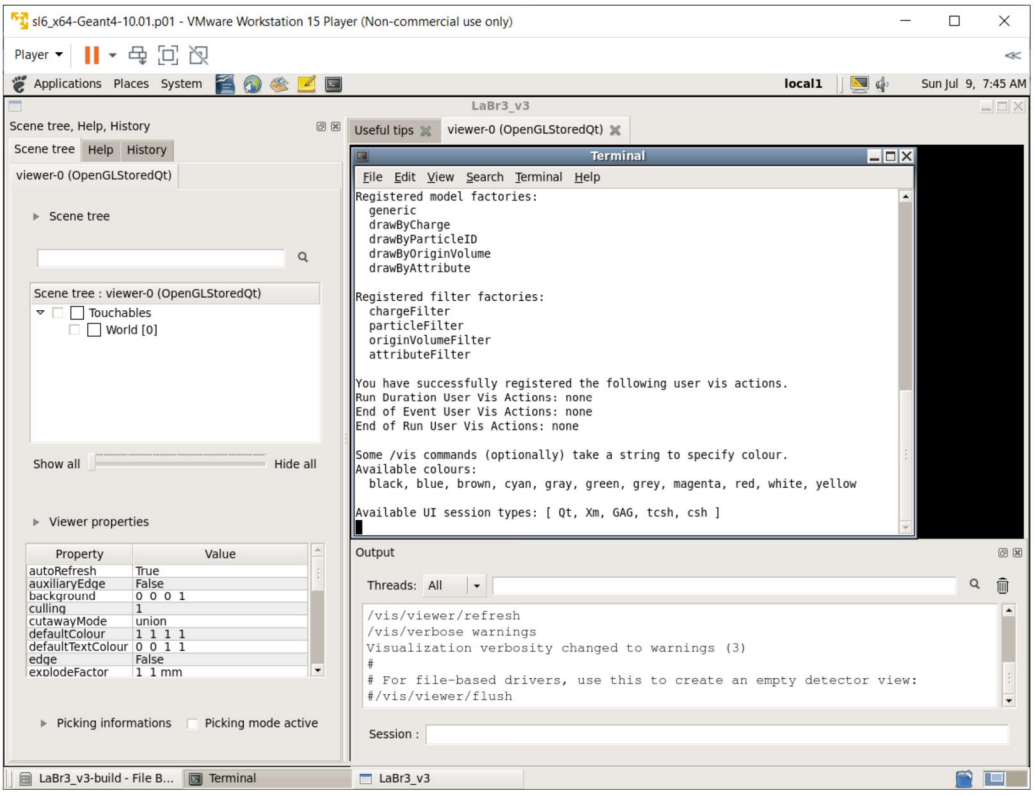

Figure C2: The simulation interface is shown.

Figure C3 illustrates the cylindrical $LaBr_3$:Ce detector as well as its major dimensions. The magenta scintillator, blue gap face, and gray aluminium case face have the same radius. Likewise, Figure C4 illustrates a single hexagonal BGO detector of the DRAGON array and its major dimensions where the scintillator is red. In this case, the radii refer to incircle radii with the exception of the photomultiplier tube. All of the figures in this section were developed by the Geant4 visualization software [44, 65].

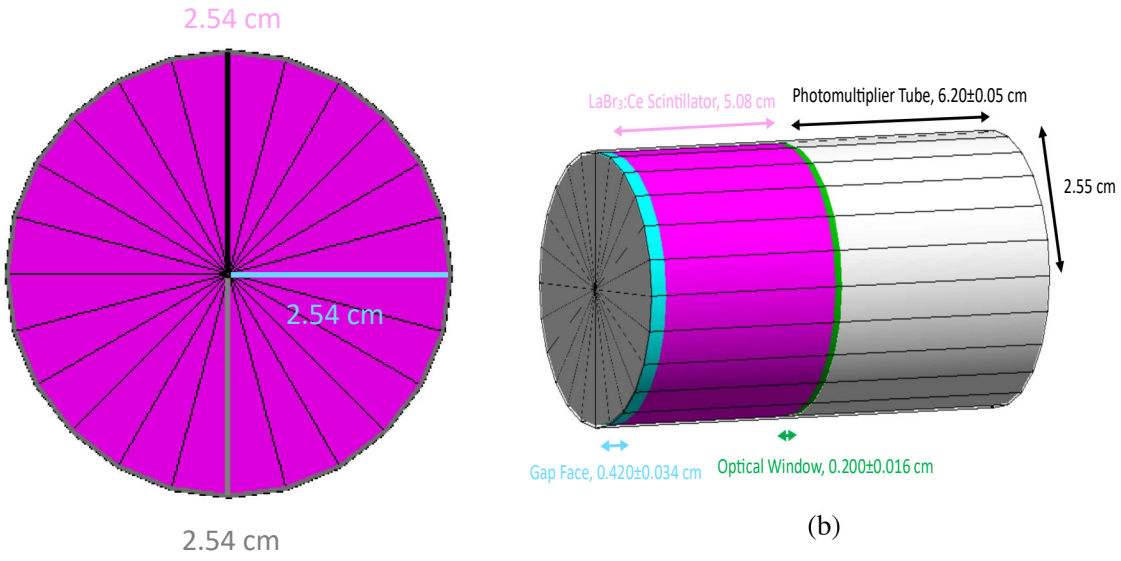

(a) (b)

Figure C3: (a) The front view of the $LaBr_3$:Ce detector is shown. (b) The side view of the $LaBr_3$:Ce detector is shown with the photomultiplier tube radius being 2.55 cm. These diagrams have not been drawn to scale.

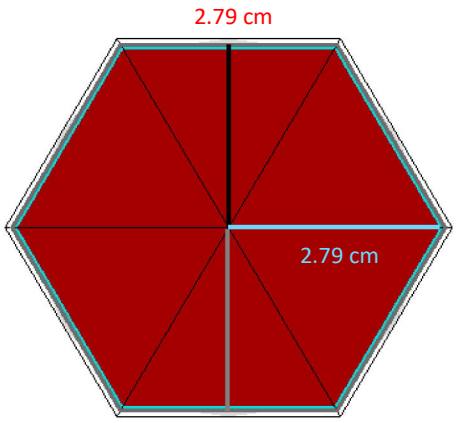

(a)

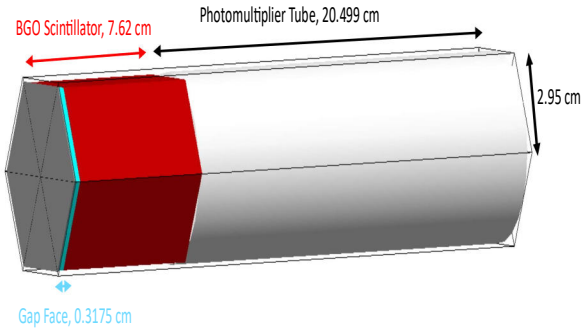

(b)

Figure C4: (a) The front view of the BGO detector is shown. (b) The side view of the BGO detector is shown with the photomultiplier tube radius being 2.95 cm. These diagrams have not been drawn to scale.

This simulation is able to simulate the entire DRAGON array with its gas target box. Figure C5 shows the right-hand side of the hexagonal array, and Figure C6 shows the left-hand side of the hexagonal array. For simplicity, all of the detectors have the Scionix design. Figure 3.5 illustrates the gas target box itself and it is also shown in Figure C7. The details on the detector dimensions are given on Table A4. The details for the gas target box dimensions are given on Table A5.

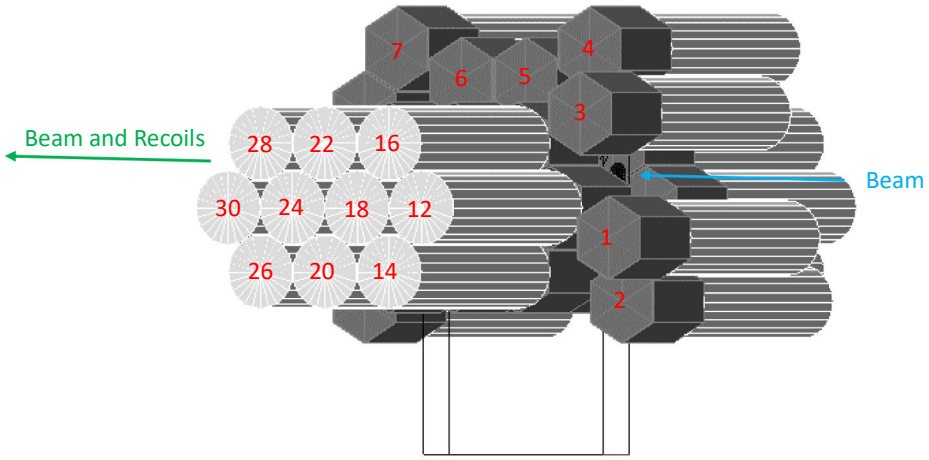

Figure C5: The right-hand side of the array along with the crown detectors are shown. Detector #1 and #2 straddle the array as shown. The direction of the beam and recoils is shown for perspective. This diagram has not been drawn to scale.

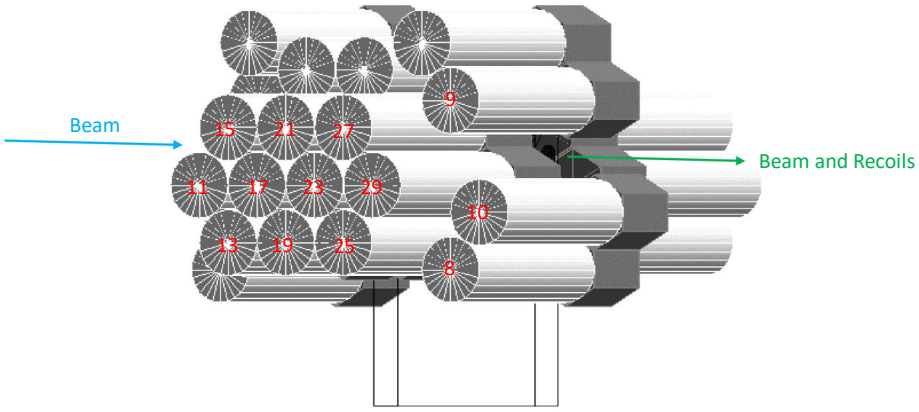

Figure C6: The left-hand side of the array is shown. Detector #8 and #10 straddle the array as shown and Detector #9 is a crown detector. The direction of the beam and recoils is shown for perspective. This diagram has not been drawn to scale.

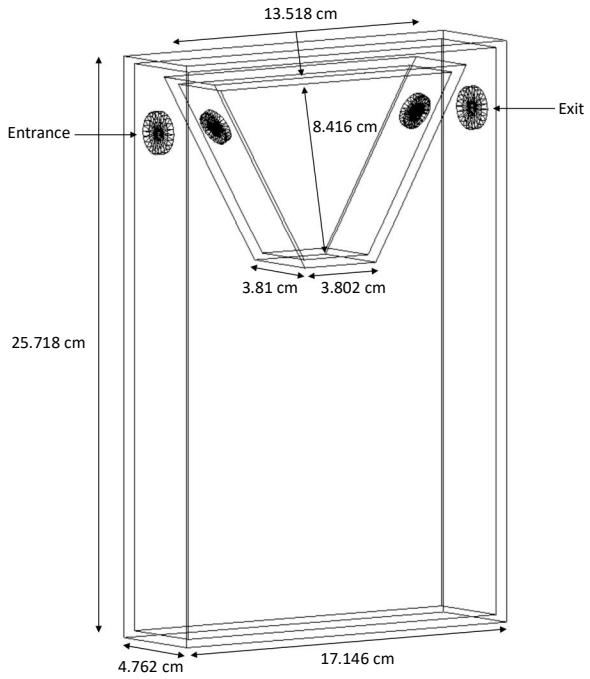

Figure C7: The major external dimensions of the gas target box are shown. This diagram has not been drawn to scale.

A complete collection of the code is given in Github. The link is: https://github.com/williamh2/Geant4-Code/tree/master. The files come in 3 folders; "src" which stands for the source files, "include" which contains the supporting files for the source files, and "macros" for the macro input files. There is also a fourth folder called "Backup Files" which holds the individual files for some of the references in Appendix D. "DetectorConstruction.cc" constructs the detectors. This simulation has been given the functionality to change the detector geometry, gap thickness, gap material, aluminium case thickness, photomultiplier tube diameter, and the photomultiplier tube length interactively as shown in the sample code for "DetectorMessenger.cc". "EventAction.cc" accumulates the energy deposit statistics for the incident gamma

ray events on the detector and fills the histograms with these events. "HistoManager.cc" shows how the histograms are generated. "PhysicsList.cc" sets up the simulation physics. "PrimaryGeneratorAction.cc" generates the particle events. "RunAction.cc" computes the statistics for the events. "SteppingAction.cc" determines the energy deposits of the incident gamma rays on the detector. "TrackingAction.cc" tracks the particles that are involved in the simulations.

For a large number of gamma ray events, the simulation would crash so it is run on the terminal without the visualization software that is seen on the simulation interface, and this mode of operation is known as the "batch" mode. To run the simulation on the terminal without actually opening it, type "./LaBr3_v3 Na22.in", for example, where "Na22.in" is the macro input file for the ^{22}Na source.

Appendix D

References

[1] C. Iliadis, 2nd ed., *Nuclear Physics of Stars*. Weinheim: Wiley–VCH, 2015.

[2] M. Arnould and K. Takahashi, "Nuclear astrophysics," *Reports on Progress in Physics*, vol. 62, no. 3, pp. 395–464, May 1999.

[3] D. G. Gigliotti, "Efficiency Calibration Measurement and Geant simulation of the DRAGON BGO Gamma Ray Array at TRIUMF," M.Sc. Thesis, University of Northern British Columbia, Prince George, BC, 2004.

[4] M. S. Scott, "The Onset and Breakout of the Stellar Hot CNO cycle," Ph.D. Dissertation, Yale University, New Haven, CT, 1990.

[5] A. M. Bebington, "Enter the DRAGON Investigating the $^{13}C(p,\gamma)^{14}N$ reaction & Using GEANT to test the DRAGON's acceptance," M.Sc. Thesis, Department of Physics, University of Surrey, Guildford, Surrey, 2004.

[6] R. K. Wallace and S. E. Woosley, "Explosive Hydrogen Burning," *The Astrophysical Journal Supplement Series*, vol. 45, pp. 389–420, February 1981.

[7] G. F. Knoll, 3rd ed., *Radiation Detection and Measurement*. Hoboken: Wiley, 2000.

[8] C. Grupen and B. A. Shwartz, 2nd ed., *Particle Detectors*. Cambridge: Cambridge University Press, 2008.

[9] C. Leroy and P. Rancoita, 2nd ed., *Principles of Radiation Interaction in Matter and Detection*. Singapore: World Scientific Publishing, 2009.

[10] M. S. Alekhin, J. T. M. de Haas, I. V. Khodyuk, K. W. Krämer, P. R. Menge, V. Ouspenski, and P. Dorenbos, "Improvement of γ–ray energy resolution of $LaBr_3:Ce^{3+}$ scintillation detectors by Sr^{2+} and Ca^{2+} co–doping," *Applied Physics Letters*, vol. 102, no. 161915, pp. 1–4, April 2013.

[11] Saint–Gobain, "Scintillation Products Technical Note," Courbevoie, France, *Saint–Gobain*, 2009. [Online]. Available: https://github.com/williamh2/Geant4-Code/tree/master/Backup%20Files. [Accessed: November 30, 2022]

[12] National Nuclear Data Center, "Evaluated Nuclear Structure Data File," *National Nuclear Data Center*, 2022. [Online]. Available: https://www.nndc.bnl.gov/ensdf/. [Accessed: November 30, 2022]

[13] S. O. Flyckt and C. Marmonier, *PHOTOMULTIPLIER TUBES principles and applications*, 2002. [E–book] Available: https://www2.pv.infn.it/~debari/doc/Flyckt_Marmonier.pdf.

[14] V. C. Spanoudaki and C. S. Levin, "Photo–detectors for Time of Flight Positron Emission Tomography (ToF–PET)," *Sensors*, vol. 10, no, 11, pp. 10484–10505, November 2010.

[15] P. Lecoq, "Development of new scintillators for medical applications," *Nuclear Instruments and Methods in Physics Research A*, vol. 809, pp. 130–139, February 2016.

[16] Hamamatsu Photonics, "Photomultiplier Tube R1828–01, R2059," Shizuoka, Japan, *Hamamatsu Photonics*, 2010. [Online]. Available: https://www.hamamatsu.com/content/dam/hamamatsu-photonics/sites/documents/99_SALES_LIBRARY/etd/R1828-01_R2059_TPMH1259E.pdf. [Accessed: October 1, 2022]

[17] ET Enterprises, "51 mm (2'') photomultiplier 9214b data sheet," Uxbridge, United Kingdom, *ET Enterprises*, 2010. [Online]. Available: https://et-enterprises.com/images/data_sheets/9214B.pdf. [Accessed: October 1, 2022]

[18] *PHOTOMULTIPLIER TUBES Basics and Applications*, 4th ed. Shizuoka, Japan: Hamamatsu Photonics, 2017. [E–book] Available: https://www.hamamatsu.com/content/dam/hamamatsu-photonics/sites/documents/99_SALES_LIBRARY/etd/PMT_handbook_v4E.pdf.

[19] D. A. Hutcheon, S. Bishop, L. Buchmann, M. L. Chatterjee, A. A. Chen, J. M. D'Auria, S. Engel, D. Gigliotti, U. Greife, D. Hunter, A. Hussein, C. C. Jewett, N. Khan, M. Lamey, A. M. Laird, W. Liu, A. Olin, D. Ottewell, J. Rogers, G. Roy, H. Sprenger, and C. Wrede, "The DRAGON facility for nuclear astrophysics at TRIUMF–ISAC: design, construction and operation," *Nuclear Instruments and Methods in Physics Research A*, vol. 498, no. 1–3, pp. 190–210, February 2003.

[20] Hamamatsu Photonics, "Photomultiplier Tubes R2083, R3377," Shizuoka, Japan, *Hamamatsu Photonics*, 2020. [Online]. Available: https://www.hamamatsu.com/content/dam/hamamatsu-photonics/sites/documents/99_SALES_LIBRARY/etd/R2083_R3377_TPMH1227E.pdf. [Accessed: October 1, 2022]

[21] M. Moszyński, A. Syntfeld–Każuch, Ł. Świderski, M. Grodzicka, J. Iwanowska, P. Sibczyński, and T.Szczęśniak, "Energy resolution of scintillation detectors," *Nuclear Instruments and Methods in Physics Research A*, vol. 805, pp. 25–35, January 2016.

[22] A. Syntfeld–Każuch, M. Moszyński, Ł. Świderski, T. Szczęśniak, A. Nassalski, C. L. Melcher, and M. A. Spurrier, "Energy Resolution of Calcium Co–doped LSO:Ce Scintillators," in *IEEE Transactions on Nuclear Science*, vol. 56, no. 5, pp. 2972–2978, October 2009.

[23] K. Klienknecht, 2nd ed., *Detectors for particle radiation*. Cambridge: Cambridge University Press: 1998.

[24] S. I. Ziegler, "Positron Emission Tomography: Principles, Technology, and Recent Developments," *Nuclear Physics A*, vol. 752, pp. 679c–687c, April 2005.

[25] S. Surti, J. S. Karp, G. Muehllehner, and P. S. Raby, "Investigation of Lanthanum Scintillators for 3–D PET," *IEEE Transactions on Nuclear Science*, vol. 50, no. 3, pp. 348–354, July 2003.

[26] S. E. Brunner and D. R. Schaart, "BGO as a hybrid scintillator / Cherenkov radiator for cost–effective time–of–flight PET," *Physics in Medicine and Biology*, vol. 62, no. 11, pp. 4421–4439, June 2017.

[27] G. Anil Kumar, I. Mazumdar, and D.A. Gothe, "Efficiency calibration and simulation of a $LaBr_3$(Ce) detector in close–geometry," *Nuclear Instruments and Methods in Physics Research A*, vol. 609, no. 2–3, pp. 183–186, October 2009.

[28] E.V.D. van Loef, P. Dorenbos, C.W.E. van Eijk, K. Krämer, and H.U. Güdel, "High–energy–resolution scintillator: Ce^{3+}activated $LaBr_3$," *Applied Physics Letters*, vol. 79, no. 10, pp. 1573–1575, August 2001.

[29] M. Moszyński, M. Balcerzyk, W. Czarnacki, M. Kapusta, W. Klamra, A. Syntfeld, and M. Szawlowski, "Intrinsic Energy Resolution and Light Yield Nonproportionality of BGO," *IEEE Transactions on Nuclear Science*, vol. 51, no. 3, pp. 1074–1079, June 2004.

[30] M. J. Weber, *Handbook of Optical Materials*. Boca Raton: CRC Press: 2003.

[31] M. Gierlik, T. Batsch, M. Moszyński, T. Szczęśniak, D. Wolski, W. Klamra, B. Perot, and G. Perret, "Comparative Study of Large NaI(Tl) and BGO Scintillators for the EURopean Illicit TRAfficking Countermeasures Kit Project," *IEEE Transactions on Nuclear Science*, vol. 53, no. 3, pp. 1737–1743, June 2006.

[32] M. E. Daube–Witherspoon, S. Surti, A. Perkins, C. C. M. Kyba, R. Wiener, M. E. Werner, R. Kulp, and J. S. Karp, "The imaging performance of a $LaBr_3$–based PET scanner," *Physics in Medicine and Biology*, vol. 55, no. 1, pp. 45–64, November 2009.

[33] K. Alzimami, E. Abuelhia, Z. Podolyak, A. Ioannou, and N. M. Spyrou, "Characterization of $LaBr_3$:Ce and $LaCl_3$:Ce scintillators for gamma–ray spectroscopy," *Journal of Radioanalytical and Nuclear Chemistry*, vol. 278, no. 3, pp. 755–759, November 2008.

[34] K. S. Shah, J. Glodo, M. Klugerman, W. W. Moses, S. E. Derenzo, and M. J. Weber, "$LaBr_3$:Ce Scintillators for Gamma Ray Spectroscopy," *IEEE Transactions on Nuclear Science*, vol. 50, no. 6, pp. 2410–2413, December 2003.

[35] Saint–Gobain, "BGO Bismuth Germanate Scintillation Material," Courbevoie, France, *Saint–Gobain*, 2012. [Online]. Available: https://github.com/williamh2/Geant4-Code/tree/master/Backup%20Files. [Accessed: October 1, 2022]

[36] Q. Bao and A. F. Chatziioannou, *GATE Simulation of a BGO Based High Sensitivity Small Animal PET Scanner*: 2007 Joint Meeting of the 6th International Symposium on Noninvasive Functional Source Imaging of the Brain and Heart and the International Conference on Functional Biomedical Imaging (NFSI–ICFBI), Hangzhou, China, October 12–14, 2007, Piscataway: Institute of Electrical and Electronics Engineers, 2007.

[37] M. Moszyński, C. Gresset, J. Vacher, and R. Odru, "Timing Properties of BGO Scintillator," *Nuclear Instruments and Methods in Physics Research*, vol. 188, no. 2, pp. 403–409, September 1981.

[38] M. E. McIlwain, D. Gao, and N. Thompson, “First Principle Quantum Description of the Energetics Associated with $LaBr_3$, $LaCl_3$, and Ce Doped Scintillators,” in *IEEE Nuclear Science Symposium Conference Record, Honolulu, USA, October 26–November 3, 2007*, Piscataway: Institute of Electrical and Electronics Engineers, 2008. pp. 2460–2465.

[39] R.E. Laxdal, G. Dutto, K. Fong, G. Mackenzie, M. Pasini, R. Poirier, and R. Ruegg, *Beam Commissioning and First Operation of the ISAC DTL at TRIUMF*: Proceedings of the 2001 Particle Accelerator Conference, Chicago, USA, June 18–22, 2001, Piscataway: Institute of Electrical and Electronics Engineers, 2002.

[40] TRI–University Meson Facility, “Post–Target Accelerators,” *TRI–University Meson Facility*, 2022. [Online]. Available: https://fiveyearplan.triumf.ca/teams-tools/post-target-accelerators/. [Accessed: June 20, 2022]

[41] TRI–University Meson Facility, Ed., *ISAC–II: A Project for Higher Energies at ISAC*. 1999.

[42] J. M. D’Auria, R. E. Azuma, S. Bishop, L. Buchmann, M. L. Chatterjee, A. A. Chen, S. Engel, D. Gigliotti, U. Greife, D. Hunter, A. Hussein, D. Hutcheon, C. C. Jewett, J. José, J. D. King, A. M. Laird, M. Lamey, R. Lewis, W. Liu, A. Olin, D. Ottewell, P. Parker, J. Rogers, C. Ruiz, M. Trinczek, and C. Wrede, “The $^{21}Na(p,\gamma)^{22}Mg$ reaction from $E_{c.m.} = 200$ to 1103 keV in novae and x–ray bursts,” *Physical Review C*, vol. 69, no. 065803, pp. 1–16, June 2004.

[43] S. Bishop, “Direct Measurement of the $^{21}Na(p,\gamma)^{22}Mg$ Resonant Reaction Rate in Nova Nucleosynthesis,” Ph.D. Dissertation, Department of Physics, Simon Fraser University, Burnaby, BC, 2003.

[44] S. Agostinelli, J. Allison, K. Amako, J. Apostolakis, H. Araujo, P. Arce, M. Asai, D. Axen, S. Banerjee, G. Barrand, F. Behner, L. Bellagamba, J. Boudreau, L. Broglia, A. Brunengo, H. Burkhardt, S. Chauvie, J. Chuma, R. Chytracek, G. Cooperman, G. Cosmo, P. Degtyarenko, A. Dell'Acqua, G. Depaola, D. Dietrich, R. Enami, A. Feliciello, C. Ferguson, H. Fesefeldt, G. Folger, F. Foppiano, A. Forti, S. Garelli, S. Giani, R. Giannitrapani, D. Gibin, J. J. Gómez Cadenas, I. González, G. Gracia Abril, G. Greeniaus, W. Greiner, V. Grichine, A. Grossheim, S. Guatelli, P. Gumplinger, R. Hamatsu, K. Hashimoto, H. Hasui, A. Heikkinen, A. Howard, V. Ivanchenko, A. Johnson, F. W. Jones, J. Kallenbach, N. Kanaya, M. Kawabata, Y. Kawabata, M. Kawaguti, S. Kelner, P. Kent, A. Kimura, T. Kodama, R. Kokoulin, M. Kossov, H. Kurashige, E. Lamanna, T. Lampén, V. Lara, V. Lefebure, F. Lei, M. Liendl, W. Lockman, F. Longo, S. Magni, M. Maire, E. Medernach, K. Minamimoto, P. Mora de Freitas, Y. Morita, K. Murakami, M. Nagamatu, R. Nartallo, P. Nieminen, T. Nishimura, K. Ohtsubo, M. Okamura, S. O'Neale, Y. Oohata, K. Paech, J. Perl, A. Pfeiffer, M.G. Pia, F. Ranjard, A. Rybin, S. Sadilov, E. Di Salvo, G. Santin, T. Sasaki, N. Savvas, Y. Sawada, S. Scherer, S. Sei, V. Sirotenko, D. Smith, N. Starkov, H. Stoecker, J. Sulkimo, M. Takahata, S. Tanaka, E. Tcherniaev, E. Safai Tehrani, M. Tropeano, P. Truscott, H. Uno, L. Urban, P. Urban, M. Verderi, A. Walkden, W. Wander, H. Weber, J. P. Wellisch, T. Wenaus, D. C. Williams, D. Wright, T. Yamada, H. Yoshida, and D. Zschiesche, "GEANT4–a simulation toolkit," *Nuclear Instruments and Methods in Physics Research A*, vol. 506, no. 3, pp. 250–303, July 2003.

[45] G. Christian, C. Akers, D. Connolly, J. Fallis, D. Hutcheon, K. Olchanski, and C. Ruiz, "Design and commissioning of a timestamp–based data acquisition system for the DRAGON recoil mass separator," *The European Physical Journal A*, vol. 50, no. 75, pp. 1–11, April 2014.

[46] Christopher L. H. Wrede, "A Double Sided Silicon Strip Detector as an End Detector for the DRAGON Recoil Mass Separator," M.Sc. Thesis, Department of Physics, Simon Fraser University, Burnaby, BC, 2003.

[47] C. Ruiz, U. Greife, and U. Hager, "Recoil separators for radiative capture using radioactive ion beams," *The European Physical Journal A*, vol. 50, no. 99, pp. 1–31, June 2014.

[48] European Council for Nuclear Research, "Physics Reference Manual, Release 10.4.," Geneva, Switzerland, *European Council for Nuclear Research*, 2017. [Online]. Available: https://indico.cern.ch/event/679723/contributions/2792554/attachments/1559217/2454299/PhysicsReferenceManual.pdf. [Accessed: September 30, 2020]

[49] Saint–Gobain, “Efficiency Calculations for Selected Scintillators,” Courbevoie, France, *Saint–Gobain*, 2007. [Online]. Available: https://github.com/williamh2/Geant4-Code/tree/master/Backup%20Files. [Accessed: September 30, 2020]

[50] N. Zelenskaya, A. Spassky, V. Lebedev, N. Orlova, and L. Galanina, “The Alignment of the $^{16}O(3^-; 6.131$ MeV) Nucleus Formed in Some Nuclear Reactions at $E_x \approx 7.5$ MeV/Nucleon,” in *LXXI International conference “NUCLEUS – 2021. Nuclear physics and elementary particle physics. Nuclear physics technologies”, St. Petersburg, Russia, September 20–25, 2021*.

[51] T. Williams and C. Kelley. *Gnuplot Version 4.4*, 2011.

[52] T. Vidmar, M. Korun, and A. Likar, “Close–geometry efficiency calibration in gamma–ray spectrometry using radio–nuclides with a two–step cascade decay,” *Nuclear Instruments and Methods in Physics Research A*, vol. 508, no. 3, pp. 404–413, August 2003.

[53] Costruzioni Apparecchiature Elettroniche Nucleari, “Technical Information Manual,” Viareggio, Italy, *Costruzioni Apparecchiature Elettroniche Nucleari*, 2005. [Online]. Available: https://groups.nscl.msu.edu/nscl_library/manuals/caen/MOD.V785%20revision.pdf. [Accessed: November 1, 2022]

[54] Phillips Scientific, “Quad Gate/Delay Generator NIM Model 794,” Ramsey, USA, *Phillips Scientific*. [Online]. Available: https://www-f9.ijs.si/~rok/detectors/doc/manuals/nim/794ds.pdf. [Accessed: November 1, 2022]

[55] Teledyne LeCroy, “NIM Model 821 Quad 100 MHz Discriminator,” Chestnut Ridge, USA, *Teledyne LeCroy*, 2015. [Online]. Available: https://wwwusers.ts.infn.it/~rui/univ/Acquisizione_Dati/Manuals/LRS%20821%20Specifications.pdf.
[Accessed: November 1, 2022]

[56] U. A. Tarim and O. Gurler, “Source–to–detector Distance Dependence of Efficiency and Energy Resolution of a 3’’x3’’ NaI(Tl) Detector,” *European Journal of Science and Technology*, no. 13, pp. 103–107, August 2018.

[57] T. Maekawa and Y. Oshima, “A rapid–detection method for radioactive cesium in the air,” *Journal of Nuclear Science and Technology*, vol. 55, no. 2, pp. 181–189, November 2017.

[58] E. I. Prosper, O. J. Abebe, and U. J. Ogri, “Characterisation of Cerium–Doped Lanthanum Bromide scintillation detector,” *Latin–American Journal of Physics Education*, vol. 6, no. 1, pp. 162–172, March 2012.

[59] D. A. Hutcheon, C. Ruiz, J. Fallis, J. M. D’Auria, B. Davids, U. Hager, L. Martin, D. F. Ottewell, S. Reeve, and A. Rojas, “Measurement of radiative capture resonance energies with an extended gas target,” *Nuclear Instruments and Methods in Physics Research A*, vol. 689, pp. 70–74, October 2012.

[60] Hamamatsu Photonics, “Photomultiplier Tubes R6427, R7056, R7057,” Shizuoka, Japan, *Hamamatsu Photonics*, 2019. [Online]. Available: https://www.hamamatsu.com/content/dam/hamamatsu-photonics/sites/documents/99_SALES_LIBRARY/etd/R6427_R7056_R7057_TPMH1377E.pdf. [Accessed: November 30, 2022]

[61] M. Williams, “Measurement of the ^{22}Ne(p,γ)^{23}Na reaction rate using the DRAGON facility and commissioning of the EMMA recoil mass spectrometer,” Ph.D. Dissertation, University of York, Heslington, England, 2018.

[62] R. Brun and F. Rademakers, *ROOT – An Object Oriented Data Analysis Framework*: New computing techniques in physics research V. Proceedings, 5th International Workshop, AIHENP '96, Lausanne, Switzerland, September 2–6, 1996, Amsterdam: *Nuclear Instruments and Methods in Physics Research A*, vol. 389, no. 1–2, pp. 81–86, 1997. Version 6.18/02.

[63] A. Migdall, S. V. Polyakov, J. Fan, and J. C. Bienfang, *Single–Photon Generation and Detection Physics and Applications*, Amsterdam, Netherlands: Elsevier, 2013. [E–book] Available: https://www.sciencedirect.com/bookseries/experimental-methods-in-the-physical-sciences/vol/45/suppl/C.

[64] H. Nomada, K. Morita, H. Higuchi, H. Yoshioka, and Y. Oki, “Carbon–polydimethylsiloxane–based integratable optical technology for spectroscopic analysis,” *Talanta*, vol. 166, pp. 428–432, May 2017.

[65] S. Incerti, G. Baldacchino, M. Bernal, R. Capra, C. Champion, Z. Francis, S. Guatelli, P. Guèye, A. Mantero, B. Mascialino, P. Moretto, P. Nieminen, A. Rosenfeld, C. Villagrasa, and C. Zacharatou, “The Geant4–DNA Project,” *International Journal of Modeling, Simulation, and Scientific Computing*, vol. 01, no. 02, pp. 157–178, June 2010.

[66] European Council for Nuclear Research, “Geant4 User's Guide for Application Developers,” Version: geant4 10.2, Geneva, Switzerland, *European Council for Nuclear Research*, 2015. [Online]. Available: https://geant4-userdoc.web.cern.ch/UsersGuides/ForApplicationDeveloper/BackupVersions/V10.2/fo/BookForAppliDev.pdf. [Accessed: September 30, 2020]